Some aspects of phase estimation in paraxial wave optics

A thesis submitted

in partial fulfillment for the award of the degree of

Doctor of Philosophy

in

Classical Optics

by

Ameen Yasir P A

Department of Physics

Indian Institute of Space Science and Technology

Thiruvananthapuram, India

June 4, 2019

Certificate

This is to certify that the thesis titled **Some aspects of phase estimation in paraxial wave optics** submitted by **Ameen Yasir P A**, to the Indian Institute of Space Science and Technology, Thiruvananthapuram, in partial fulfillment for the award of the degree of **Doctor of Philosophy** in **Classical Optics**, is a bonafide record of the research work carried out by him under my supervision. The contents of this report, in full or in parts, have not been submitted to any other Institute or University for the award of any degree or diploma.

Dr. J. Solomon Ivan,
Associate Professor.

Dr. Umesh R. Kadhane,
Associate Professor,
HOD, Dept. of Physics.

Place: Thiruvananthapuram
Date: June 4, 2019

Acknowledgements

I am grateful to Dr. J. Solomon Ivan for his constant encouragement and guidance throughout my years at IIST.

Ameen Yasir P A

Abstract

Estimation of phase information through the knowledge of intensity information is a well-studied problem. The intensity measurements can be made, for instance, at two or more transverse planes in the direction of wave field propagation, or using an interferometric setup. The phase is then retrieved from such intensity measurements using several well-known techniques. These retrieved phases could possess dislocations, i.e., phase is undefined at points where the intensity vanishes. Phase retrieval through many plane intensity measurements, in general, requires the knowledge of a general first-order optical system (FOOS). Thus, we first realize any general FOOS using the optical transformations : free propagation, thin convex lens, and thin cylindrical lens of positive focal length.

As is well known, any general FOOS is characterized by a matrix in $Sp(4, \mathbb{R})$, symplectic group in 4 dimensions with its entries being real. Using Euler decomposition, we first write the given $Sp(4, \mathbb{R})$ matrix as a product of orthogonal symplectic matrices in 4 dimensions and differential magnifier matrix in 4 dimensions. These matrices are then realized in terms of free propagation and thin lenses of positive focal length. It is shown that not more than four convex lenses and 14 cylindrical lenses of positive focal length are required to realize any matrix in $Sp(4, \mathbb{R})$. Besides, if the symplectic matrix $\mathbf{S} \in Sp(4, \mathbb{R})$ is of the form $\mathbf{S} = S_1 \oplus S_2$, where $S_1,\ S_2 \in Sp(2, \mathbb{R})$, then we prove that such $\mathbf{S}$ can be realized using not more than three convex lenses and seven cylindrical lenses of positive focal length. In addition, we have provided for the first time, to the best of our knowledge, explicit decompositions for the well known optical transformations such as differential free and inverse propagations, partial and inverse Fourier transformations, image reflectors, differential magnifiers, and differential fractional Fourier transformations.

Having realized any general FOOS, we now consider the problem of retrieving the phase possessing dislocations from two or more transverse plane intensity measurements. In this regard, we propose an iterative algorithm to retrieve phases with dislocations through three transverse plane intensity measurements and demonstrate the same numerically using Monte-Carlo simulations. The algorithm makes use of partial Fourier transformation, i.e., Fourier transformation in one transverse coordinate and identity transformation on the other, an example of asymmetric FOOS which is optically implemented using thin cylindrical lenses and free propagation transformations. Because partial Fourier transforma-

tion, unlike Fourier transformation, does not conserve longitudinal orbital angular momentum (OAM) of the wave field in general, the phase dislocation(s) possessed by the wave field is (are) created or destroyed naturally and its (their) orientation is (are) also distinguished. For numerical demonstration, we consider complex random linear superpositions of Laguerre-Gaussian (LG) beams with added white Gaussian noise. In all studied random superpositions, the algorithm converged well within 100 iterations. The proposed method is found to work well for wave fields with both integral and non-integral longitudinal OAM.

We then deal with the problem of phase retrieval from perturbed straight line fringes. For this problem, we present a single-shot phase retrieval algorithm from straight line fringes without phase unwrapping. It is worth mentioning here that most of the phase retrieving algorithms available in the literature require phase unwrapping – a process in which the extracted phase has to unwrapped, i.e., add and subtract 2π wherever discontinuity occurs, typically owing to the periodicity of $\tan^{-1}$ function. We first obtain phase gradients from the given interferogram using Hilbert-pair method, and then the desired phase is estimated from the gradients using the method of least squares for the Hudgin geometry. Here, the inverse of the matrix appearing in the method of least squares is computed analytically through the use of discrete cosine transform (DCT) as well as additional symmetries available in the Hudgin geometry. As a result, the computational time is reduced drastically and could as well be implemented in real-time applications. The algorithm is tested on both numerical interferograms with added white Gaussian noise, as well as on interferograms obtained from a Mach–Zehnder setup, where the respective imparted phases were random, and corresponded to atmospheric turbulence-like models.

Contents

List of Figures

List of Tables

Abbreviations

BS	beam-splitter
CCD	charge-coupled device
DCT	discrete cosine transform
FOOS	first-order optical system
GS	Gerchberg-Saxton
HG	Hermite-Gaussian
HWP	half wave plate
IP	input plane
IW	incoming wave field
LA	laser
LG	Laguerre-Gaussian
LCT	linear canonical transformations
LHS	left hand side
ND	neutral density filter
OAM	orbital angular momentum
OP	output plane
PBS	polarizing beam splitter
PFT	partial Fourier transformation
PRPP	pseudo-random phase plate
PW	plane wave field
PZT	piezo-electric transducer
RHS	right hand side
RMS	root mean square
SF	spatial filter
SNR	signal-to-noise ratio
TIE	transport-of-intensity equation

Nomenclature

$\mathbf{A}$	vector potential
$A(x)$	amplitude function
B	Hudgin geometry matrix
$\mathbf{B}$	magnetic field
c	velocity of light in vacuum
c	column folding operation
$\mathrm{C}\left(\phi_1, \phi_2\right)$	correlation between phases $\phi_1(x, y)$ and $\phi_2(x, y)$
$C(2n)$	correlation between $\psi(x, y; z)$ and $\psi_{2n}(x, y; z)$
C_n^2	refractive-index structure constant
$\mathcal{C}$	$[\mathcal{C}_1 \oplus \cdots \oplus \mathcal{C}_N]$
$\mathcal{C}_1$	$\mathrm{diag}\left\{N^2, \Lambda_2, \ldots, \Lambda_N\right\}$
$\mathcal{C}_j$	$\mathrm{diag}\left\{\Lambda_j, \Lambda_2 + \Lambda_j, \ldots, \Lambda_N + \Lambda_j\right\}$ with $j = 2, 3, \ldots, N$
$\mathcal{C}_j^{(k)}$	(k, k)–th entry of $\mathcal{C}_j$ with $j, k = 1, 2, \ldots, N$
d	distance between two transverse planes
D_1	$\mathrm{diag}\left\{\Lambda_1, \ldots, \Lambda_n\right\}$
D_2	$N \times N$ matrix whose $(1, 1)$–th entry is N and all other entries are 0
$\mathbf{D}_{\alpha,\beta}$	symplectic matrix associated with differential fractional Fourier transform
$\mathbf{E}$	electric field
E_j	$V\,\mathcal{C}_j^{-1}\,V^T$ with $j = 1, 2, \ldots, N$
f	focal length of a thin lens
$f_x\,(f_y)$	focal length of a thin cylindrical lens whose curvature is along the $x\,(y)$ direction
$F(d)$	two dimensional free propagation matrix for a distance d
$\mathbf{F}(d)$	direct sum of two $F(d)$'s
$\mathcal{F}_d$	free propagation unitary operator
$\mathfrak{F}$	Discrete Fourier transform matrix after `fftshift` operation

	applied to both its rows and columns
$\mathsf{F_c}$	$N \times N$ matrix whose j–th column vector is P_j with $j = 1, 2, \ldots, N$
f	$I_0 \cos\varphi$
$\mathsf{f}_x\,(\mathsf{f}_y)$	$\partial\mathsf{f}/\partial x\,(\partial\mathsf{f}/\partial y)$
g	$I_0 \sin\varphi$
$\mathsf{g}_x\,(\mathsf{g}_y)$	$\partial\mathsf{g}/\partial x\,(\partial\mathsf{g}/\partial y)$
G	$\mathsf{F_c}\,V$
G_j	j–th column vector of G with $j = 1, \ldots, N$
$h(\mathbf{x})$	free propagation kernel
$\tilde{h}(\tilde{\mathbf{x}})$	Fourier transform of the free propagation kernel
$H_m(x)$	Hermite polynomial with index m
i	$\sqrt{-1}$
$\mathbb{I}$	identity operator in infinite dimensions
$I(x, y)$	intensity function
$I(i, j)$	discretized version of $I(x, y)$
$I_0(x, y)$	background intensity
$I_c(x, y)$	intensity function without $I_0(x, y)$
$I_s(x, y)$	Hilbert transform of $I_c(x, y)$
$\tilde{I}_0(x, y)$	Fourier transform of $I_0(x, y)$
$\mathbf{I}_y$	symplectic matrix associated with image reflector transformation
$\hat{i}$	unit vector along the x–axis
$\hat{j}$	unit vector along the y–axis
$\mathbf{J}_j$	symplectic orthogonal matrices in 4 dimensions with $j = 0, 1, 2, 3$
$\hat{J}_j$	quadratic operators corresponding to the symplectic orthogonal matrices in 4 dimensions with $j = 0, 1, 2, 3$
$\mathcal{J}_j$	unitary operators corresponding to the symplectic orthogonal matrices in 4 dimensions with $j = 0, 1, 2, 3$
$\hat{k}$	unit vector along the z–axis
L	orbital angular momentum density
$\bar{\mathsf{L}}$	L averaged over the transverse plane
$\mathsf{L}^{\mathrm{ext}}$	extrinsic angular momentum density
$\bar{\mathsf{L}}^{\mathrm{ext}}$	$\mathsf{L}^{\mathrm{ext}}$ averaged over the transverse plane
$\mathsf{L}^{\mathrm{int}}$	intrinsic angular momentum density
$\bar{\mathsf{L}}^{\mathrm{int}}$	$\mathsf{L}^{\mathrm{int}}$ averaged over the transverse plane
L_z	z component of L

$\bar{\mathsf{L}}_z$	L_z averaged over the transverse plane
$\mathsf{L}_z^{\rm ext}$	z component of $\mathsf{L}^{\rm ext}$
$\bar{\mathsf{L}}_z^{\rm ext}$	$\mathsf{L}_z^{\rm ext}$ averaged over the transverse plane
$\mathsf{L}_z^{\rm int}$	z component of $\mathsf{L}^{\rm int}$
$\bar{\mathsf{L}}_z^{\rm int}$	$\mathsf{L}_z^{\rm int}$ averaged over the transverse plane
L_ς	ray transfer matrix of a lens with thickness ς
$L(f)$	ray transfer matrix of a thin lens of focal length f
$\mathbf{L}(f)$	direct sum of two $L(f)$'s
$\mathcal{L}_f$	thin lens unitary operator
$\mathcal{L}_f^x$	thin cylindrical lens unitary operator whose curvature varies in the x direction
$\mathcal{L}_f^y$	thin cylindrical lens unitary operator whose curvature varies in the y direction
$L_p^l(x)$	associated Laguerre polynomial
M	matrix of size $(N-1)\times N$ used in the Hudgin geometry matrix B
M_a	$\mathrm{diag}\,\{a, 1/a\}$
$\mathbf{M}$	$M_a \oplus M_b$
$\mathcal{M}$	unitary operator associated with the magnifier transformation
n	refractive index of the given medium
$O(4,\mathbb{R})$	orthogonal group in 4 dimensions
P	Cauchy principal value
P	linear momentum density
$\bar{\mathsf{P}}$	P averaged over the transverse plane
$\mathbf{p}$	(p_x, p_y)
$\hat{p}_x$	$-i(\partial/\partial x)$ in the position representation
$\hat{p}_y$	$-i(\partial/\partial y)$ in the position representation
p_j	(j,j)–th diagonal entry of the (infinite dimensional) cross-spectral density matrix with $\sum_j \mathrm{p}_j = 1$
P_k	a point in the k–the transverse plane
P_j	j–th column vector of size $N\times 1$ obtained when the column vector $B^T s$ of size $N^2\times 1$ is broken into N column vectors of equal size $N\times 1$ with $j = 1,\ldots,N$
$\mathbf{P}_y(d)$	symplectic matrix associated with partial Fourier transform
$\tilde{\mathbf{P}}_y(d)$	$-\mathbb{1}\!\mathbb{1} \oplus \sigma_d$
$\mathcal{Q}$	penalty function

$\mathbf{r}$	$x\,\hat{i} + y\,\hat{j} + z\,\hat{k}$
R_α	rotation matrix in two dimensions (see (4.7))
$\mathbf{R}$, $\mathbf{R}_1$, $\mathbf{R}_2$	4-dimensional orthogonal symplectic matrices
$R(z)$	radius of the curvature of the paraxial wave field at a given z
s_1 (s_2)	column vector formed by concatenating the rows of φ_x (φ_y)
	followed by a transposition
s	$[s_1^T, s_2^T, 0]^T$
S_1, S_2	front and back surfaces of a lens
S_1, S_2	two dimensional symplectic matrices
$\mathbf{S}$	4-dimensional symplectic matrix
$\mathbf{s}_1$, $\mathbf{s}_2$, $\mathbf{s}_3$, $\mathbf{s}_4$	block matrices of $\mathbf{S}$
s_{jk}	(j,k)–th entry of $\mathbf{S}$
$\mathrm{sgn}\,(x)$	signum function
$\mathrm{SU}(2)$	special unitary group in 2 dimensions
$Sp(2,\mathbb{R})$	symplectic group in 2 dimensions
$Sp(4,\mathbb{R})$	symplectic group in 4 dimensions
t	time
u	distance between point object and imaging element
$\mathrm{U}(1)$	unitary group in one dimension
$\mathrm{U}(2)$	unitary group in two dimensions
$U(x)$	real, square integrable function
$U_h(x)$	Hilbert transform of $U(x)$
$U_a(x)$	complex analytic signal associated with $U(x)$
$\tilde{U}(\tilde{x})$	Fourier transform of $U(x)$
$\tilde{U}_h(\tilde{x})$	Fourier transform of $U_h(x)$
$\tilde{U}_a(\tilde{x})$	Fourier transform of $U_a(x)$
$\mathcal{U}$	most general quadratic in the operators $\hat{x}$, $\hat{p}_x$, $\hat{y}$, and $\hat{p}_y$
$\mathcal{U}_1$	most general quadratic in the operators $\hat{x}$ and $\hat{p}_x$
$\mathcal{U}_2$	most general quadratic in the operators $\hat{y}$ and $\hat{p}_y$
v	distance between image of the point object and imaging element
$\mathcal{V}$	electric potential
V	orthogonal matrix whose column vectors are the eigenvectors of $\mathsf{M}^T\mathsf{M}$
$\tilde{v}_k$	$1/\sqrt{2}$ when $k = 1$ and 1 when k runs from 2 through N
w	row vector of size $1 \times N$ whose all entries are 1
$W(\mathbf{x}, \mathbf{p})$	Wolf function

$w(z)$	width of the paraxial wave field at a given z
$\hat{x}$	x in the position representation
x_k	distance between the point P_k and the optical axis in the x–z plane
x'_k	angle between the ray going through the point P_k and the optical axis in the x–z plane
$\mathbf{x}$	(x, y)
x_k	$[x_k, x'_k]^T$
$\hat{y}$	y in the position representation
y_k	distance between the point P_k and the optical axis in the y–z plane
y'_k	angle between the ray going through the point P_k and the optical axis in the y–z plane
y_k	$[y_k, y'_k]^T$
z_r	Rayleigh range
δ_z	propagation distance
δz	distance between two nearby points in the z-axis
$\tilde{\Delta}(x, y)$	lens thickness function
ϵ_0	permittivity of free space
η	additive white Gaussian noise
Γ	cross spectral density
$\boldsymbol{\kappa}$	three dimensional spatial wave number ($\kappa_x\,\hat{i} + \kappa_y\,\hat{j} + \kappa_z\,\hat{k}$)
κ	modulus of $\boldsymbol{\kappa}$
μ	mean value
∇	gradient operator
$\nabla_\perp$	gradient operator in the transverse x–y plane
λ	wavelength of the monochromatic wave field
Λ	large positive real number
Λ_k	eigenvalues of $\mathsf{M}^T\mathsf{M}$ with k running from 1 through N
μ_0	permeability of free space
$\phi(x, y)$	phase function
$\phi(i, j)$	discretized version of $\phi(x, y)$
$\phi_w(x, y)$	wrapped phase function
$\phi_x\,(\phi_y)$	$\partial\phi/\partial x\,(\partial\phi/\partial y)$
$\Phi(x)$	auxiliary function associated with $\phi(x)$
$\Phi_n(\boldsymbol{\kappa})$	power spectral density of the refractive index fluctuations
$\Phi_\theta(\boldsymbol{\kappa})$	random phase power spectrum

$\Psi(x, y, z; t)$	monochromatic wave field
$\Psi_s(x, y; z)$	spatial part of Ψ
$\Psi_t(t)$	temporal part of Ψ
$\psi(x, y; z)$	paraxial wave field
σ_d	ray transfer matrix associated with the Fourier transform
σ^2	variance
τ	twist parameter
$\Theta(x)$	Heaviside step function
$\varphi(x, y)$	phase function along with the tilt term
$\varphi(i, j)$	discretized version of $\varphi(x, y)$
φ_x (φ_y)	$\partial\varphi/\partial x$ ($\partial\varphi/\partial y$)
ϖ	k–th root of unity ($\exp(2\pi i/k)$)
$\boldsymbol{\varphi}$	column vector corresponding to $\varphi(i, j)$
ς	thickness of a lens
ξ	(x, p_x, y, p_y)
$\hat{\xi}$	$[\hat{x}, \hat{p}_x, \hat{y}, \hat{p}_y]^T$
$\hat{\xi}'$	$[\Delta\hat{x}, \Delta\hat{p}_x, \Delta\hat{y}, \Delta\hat{p}_y]^T$
$\langle\hat{\xi}\rangle$	expectation of the operator $\hat{\xi}$ associated with $\psi(x, y; z)$
$\zeta(z)$	Gouy phase
$\mathbb{1}$	identity matrix in two dimensions
——	In Bibliography, there are few references where the author's name is given as "——". This just means that the author's name of this reference is the same as the previous one. For example, the authors of Ref. [13] are T. E. Gureyev, A. Roberts, and K. A. Nugent, the same as that of Ref. [12]. This happens due to the bibliographic file compilation format.

Chapter 1

Introduction

1.1 Phase estimation in optics

Phase estimation through intensity measurements is well explored, and several methods have been studied and demonstrated [1, 2, 3, 4, 5, 6, 7, 8, 9, 10, 11, 12, 13, 14]. This is typically done as follows. First, the intensity pattern is captured at one or many transverse planes in the direction of wave field propagation by means of recording devices such as charge-coupled device (CCD) camera. Then, the phase information encoded in the intensity pattern measured at the respective transverse plane(s) is extracted through several well-known techniques [4, 5, 9, 10, 14, 12, 13, 15, 16, 17]. These phase estimation techniques broadly fall into one of the two categories : *interferometry based* and *diffraction based* (see Figure 1.1).

We first briefly study the interferometry based method [4, 5, 16, 15, 18, 17, 19, 20, 21, 22, 23, 24, 25, 26, 27, 28, 29, 30, 31, 32, 33, 34, 35, 36, 37]. In this method, two coherent wave fields drawn from the same source are superposed, and relative phase acquired by one of the wave fields is to be estimated. The phase is then retrieved from the recorded intensity, also known as the 'interferogram'. For instance, when the two sources are collimated and of equal and uniform transverse amplitude, the transverse intensity of the recorded interferogram can be expressed as :

$$I(x,y) = I_0 \left\{1 + \cos\left[\varphi(x,y)\right]\right\} + \eta(x,y), \tag{1.1}$$

$$\text{where } \varphi(x,y) = \kappa_x x + \kappa_y y - \phi(x,y). \tag{1.2}$$

Here, $\kappa_x x + \kappa_y y$ is the relative tilt factor between the two collimated sources, $\phi(x,y)$ is the phase acquired by one of the sources, $I_0 \equiv I_0(x,y)$ is the background intensity, and $\eta(x,y)$ is the additive noise term. It can be noted that $I_0(x,y)$ can be slowly varying in

the transverse plane variables x and y, and this slow variation can be traced to the quasi-monochromaticity of the coherent source [38, 39, 2]. In order to obtain the phase $\phi(x, y)$, first $\varphi(x, y)$ is retrieved from Eq. (1.1), and then $\phi(x, y)$ is obtained from $\varphi(x, y)$ by removing the tilt.

There are several approaches towards retrieving $\phi(x, y)$ from $I(x, y)$ of Eq. (1.1) [1, 7, 15, 16, 17]. These methods typically involve expressing $\tan[\phi(x, y)]$ in terms of the measured intensity(s) $I(x, y)$, and then $\phi(x, y)$ is obtained by applying $\tan^{-1}$ on the obtained expression. However, the thus obtained $\phi(x, y)$ is in its wrapped form owing to the periodicity of $\tan^{-1}$ function, and it has to be unwrapped [15, 16, 3]. Two well known approaches towards retrieving $\phi(x, y)$ from Eq. (1.1) are the *phase shifting method* [4, 5], and the *Fourier fringe analysis method* [15, 16]. In the former method, an expression for $\tan[\phi(x, y)]$ is obtained from several recorded interferograms for the same phase object, where the recorded interferograms are phase shifted versions of one another. The phase shifts between the two coherent light fields can be obtained in a controlled manner using piezoelectric phase shifters [28], or for instance using the geometric phase [20, 21, 23]. In the latter method, $\tan[\phi(x, y)]$ is obtained using only a single interferogram, for instance, through the Hilbert transform [16]. Thus the latter method has the advantage in that only a single interferogram is required, nevertheless it relies on approximations that need to be ensured [40, 41, 42, 43]. More recently, several methods towards retrieving $\phi(x, y)$ from Eq. (1.1) have been proposed which do not require unwrapping of the phase [44, 31, 36].

We now move on to briefly discuss the diffraction based methods. These methods make use of diffraction of the wave field and can be broadly classified into two major categories : *gradient based* and *iteration based*. In the former method, gradients of a wave field are extracted from the diffracted intensity pattern generated by a lenslet array [45, 46, 47] placed in a wavefront sensor. The phase is then estimated with the knowledge of the gradients [45, 48, 49, 47, 50, 51, 52]. Several geometries and methods in this regard have been proposed and demonstrated [44, 45, 47, 48, 49, 50, 51, 52, 53, 54, 55, 56, 57]. A significant difference between the interference based approach and the gradient based approach towards phase estimation may be noted. Since in the former approach, $\tan[\phi(x, y]$ is estimated, its periodicity over 2π can necessitate phase unwrapping. However, since in the latter approach, phase is directly estimated from its gradients, say, for instance, using the least square fit, there is no inherent requirement for phase unwrapping. In the latter method, the wave field typically is diffracted by means of free propagation and thin lenses, and the diffracted intensity patterns are recorded at two or more transverse planes [58, 59, 60, 61, 62, 63, 64]. The phase information is then extracted from these

intensities by the widely known iterative algorithms such as Gerchberg-Saxton (GS) algorithm [58] and Fienup algorithm [60].

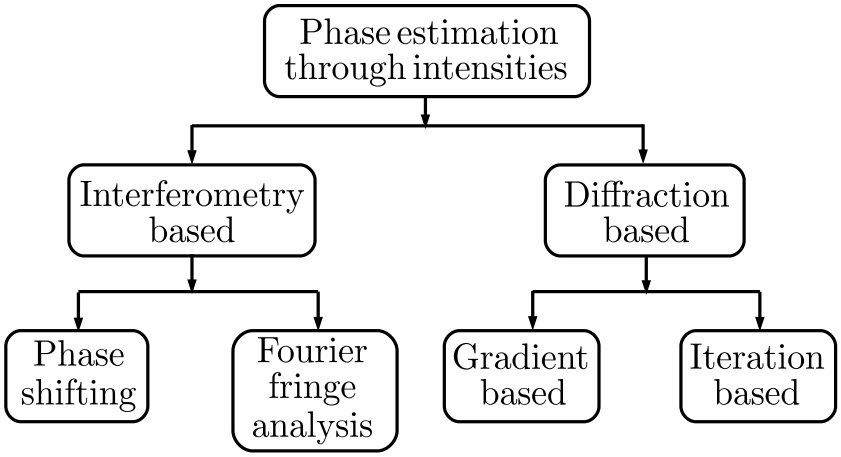

Figure 1.1: Diagram classifying phase estimation through measurement of intensity(s).

Wave fields whose phases possess dislocations [65] have been well explored in the literature [66, 67, 8, 68, 69, 70, 71, 72, 73, 71, 74, 75]. Such wave fields occur naturally in several contexts such as in optics [66, 67, 8, 74, 75], electron beams [68, 69], x-ray beams [70], atom interferometry [71, 72], Bose-Einstein condensates [73, 71], etc. A well-known example in paraxial wave optics are the Laguerre-Gaussian (LG) modes which are the stable solutions of the paraxial wave equation [76], and these are readily realized in experiments [76, 77, 78]. In fact, the LG modes and their superpositions are known to possess well-defined orbital angular momentum (OAM), which is intrinsically linked to the dislocations in their phase [79, 80, 81, 82, 83, 84, 85, 86, 87, 88, 89, 90]. The LG modes and their superpositions have been explored as potential carriers of information, particularly in free space optical communication [91, 8, 92], and quantum information processing [67, 93]. An important problem in regard of LG modes and their superpositions is the detection of dislocations in their phase (also their orientation [85, 86, 87, 88]), estimation of such a phase through intensity measurements [8, 9, 10, 11, 12, 13, 14], and estimation of OAM possessed by such wave fields [81, 82, 83, 84]. While amplitude is readily available through intensity measurements, phase is in principle retrieved.

A well known approach in retrieving phases with dislocations is the transport-of-intensity

method [8, 9, 10], an example of diffraction based method. For instance, the wave field is propagated through a known first-order optical system (FOOS) and the transverse intensities are measured in the two (or more) respective planes, with the intensities in the respective planes being transported versions of one another. The phase is then algorithmically retrieved from the transported intensities. This is done either iteratively [60, 11] as in the Gerchberg-Saxton (GS) algorithm [58], or by solving the transport-of-intensity equation (TIE) [8, 9, 10, 12, 13, 14], or by using both [75, 14]. In this regard, it is pertinent to mention that such methods, in particular, make use of additional constraints while retrieving the phase [9, 11, 75].

Here, it is fitting to mention the important work of Allen and coworkers [75]. They were interested in extracting the phase information of an image consisting of N first-order vortexes using TIE and modified version of the GS algorithm. Because the uniqueness of the phase was lost at the N vortexes (as the intensity vanished), they had to guess the sign of the vortexes from $2^N - 1$ choices. Besides, the convergence was obtained after 939 iterations. Martin and Allen [11] used another variant of GS algorithm to successfully recover phases with first-order vortex, but however, the convergence was achieved after 10,000 iterations for the studied examples. In passing, it is interesting to note that very few methods exist even in finding the signature of the phase dislocation [85, 86, 87], let alone extracting such a phase.

With this brief introduction, we, in this thesis, will propose new algorithms to extract phase from intensity measurements and demonstrate them numerically as well as experimentally.

1.2 Summary of results obtained in the Thesis

In this Section we will outline the results obtained in this Thesis. First, as mentioned above, extraction of phases with dislocations does require the knowledge of FOOS. An optical system is said to belong to a FOOS if its corresponding Wolf function transforms linearly [94]. Such systems can broadly be classified into two categories : *symmetric* and *asymmetric*. Realization of symmetric FOOS using thin lenses of arbitrary focal length was first classified in Ref. [94] and was proved that any such system can be realized using free propagation and three thin lenses of arbitrary focal length alone. In Ref. [95], it was proved that three thin convex lenses of arbitrary focal length (as opposed to three thin lenses as in Ref. [94]) would suffice in realizing any symmetric FOOS. Moreover, it was shown in Ref. [95] that five thin convex lenses of fixed focal length would also realize any symmetric

FOOS. In the case of asymmetric FOOS, it was indicated in Ref. [94] that such systems could be realized using free propagation and thin lens transformations. In Ref. [96], few examples of asymmetric FOOS such as partial Fourier transformation (PFT) and image reflector were studied and some results in their regard were outlined.

In this Thesis we develop explicit decompositions to realize any general FOOS, symmetric as well as asymmetric, in terms of optical transformations including free propagations, thin convex lenses, and thin cylindrical lenses of positive focal length. In addition, we provide explicit decompositions for optical transformations including one-sided free propagation, differential free and inverse propagations, partial and inverse Fourier transformations, image reflectors, differential magnifiers, differential fractional Fourier transformations, gyrator, and cross-gyrator transformations.

Having realized any general FOOS using thin lenses of positive focal length, we propose an iterative algorithm which extracts the phase information (consisting of one or many dislocations, i.e., OAM of the wave field [8]) of a wave field from three transverse plane intensity measurements. Here, the wave fields at first and second transverse planes are related through PFT, i.e., identity transformation in one transverse coordinate and Fourier transformation in another transverse coordinate, and is realized as in Figure 4.12, and those at second and third are related through free propagation transformation. It is worth mentioning now that PFT does not conserve the OAM of the wave field in general, and our algorithm does not require the knowledge of any boundary conditions.

Finally we propose a single-shot phase extraction algorithm from interferogram with perturbed straight line fringes. As is well known, phase extracted from interferograms using methods such as Fourier fringe analysis [15], phase shifting method [25], Hilbert-pair method [16], and so on, is typically in wrapped form. Hence, we need to unwrap them, a process in which one needs to add and subtract 2π wherever discontinuity occurs, as the extracted phase assumes values between $-\pi$ and π. On the contrary, phase estimated from gradient based methods [45] do not require unwrapping, for the phase is estimated directly from its gradients, say, for instance, using the least squares fit. Our algorithm retrieves phase in an unwrapped form, combining techniques available in Hilbert-pair method and gradient based methods.

1.3 Organization of the thesis

Having introduced the outline of the Thesis in Chapter 1, in Chapter 2 we derive elementary optical transformations, free propagation and thin lens, in the context of ray as well as wave

optics, and bring out the equivalence between them. To begin with, we develop ray transfer matrices of these optical transformations in the paraxial limit in Section 2.2. In Section 2.3 we first derive wave equation from Maxwell equations, obtain paraxial wave equation from it in the paraxial limit, and discuss the solutions of the paraxial wave equation. In Sections 2.4 and 2.5 we explain how a paraxial wave field transforms under the action of free propagation and thin lens in the wave optic picture. Then, in Section 2.6 we introduce linear canonical transformations (LCT) and show the explicit connection between optical transformations, in the paraxial limit, occurring in ray and wave optics. Finally in Section 2.7 we obtain longitudinal orbital angular momentum (OAM) carried by a paraxial wave field traveling in z-direction, for instance, Laguerre-Gaussian (LG) modes, solutions of paraxial wave equation in cylindrical coordinate system dealt in Section 2.3, and in Section 2.8 we offer some concluding remarks.

In Chapter 3 we review some standard algorithms, and some useful phase estimation tools and techniques existing in the literature to extract phase from intensities. First, we consider interferometry based methods. In Section 3.2 we discuss phase shifting interferometry. In Section 3.3 we define Hilbert transforms and asymptotic analytic signals, mathematical tools we require in Fourier fringe analysis (Section 3.4), one of the widely used methods to extract phase from perturbed straight line fringes. We then demonstrate phase unwrapping process in Section 3.5 as the estimated phase through the method of Fourier fringe analysis is generally in wrapped form. We now move on to diffraction based methods. For the gradient based method, we describe the working principle of Shack-Hartmann wavefront sensor in Section 3.6, a sensor which measures phase gradients of the incoming wave field. For the iteration based method, we discuss the widely used GS algorithm and some of its variants in Section 3.7, followed by phase retrieval using TIE in Section 3.8. In passing, we define noise and related terminologies in Section 3.9, as it is inherently present when we measure intensities in a lab. Finally, in Section 3.10 we end up with some concluding remarks.

In Chapter 4 we realize a general FOOS using optical transformations including free propagation, thin convex lenses, and thin cylindrical lenses of positive focal length. In Section 4.2 we realize some well known examples of symmetric FOOS as worked out by the author in Ref. [95]. In Section 4.3 we discuss the singular value and Euler decompositions of any $\mathbf{S} \in Sp(4, \mathbb{R})$, symplectic matrix in 4 dimensions with real entries. In Section 4.4 we arrive at identities for some well known optical transformations of the form $S_1 \oplus S_2$, where $S_1,\ S_2 \in Sp(2, \mathbb{R})$, by making use of the results obtained in Section 4.2. A method to realize any $\mathbf{S}$ of the form $S_1 \oplus S_2$, symplectic matrices in 2 dimensions with real entries,

is also outlined. In Section 4.5 the results obtained in the previous Sections are further used to realize any $\mathbf{S} \in Sp(4, \mathbb{R})$. Finally, we end with some concluding remarks in Section 4.6.

In Chapter 5 we propose an iterative algorithm to estimate phases with dislocations from three plane intensity measurements, and demonstrate the same numerically using Monte-Carlo simulations. In Section 5.2 we briefly review paraxial light fields in the context of longitudinal OAM, Fourier transformation, and partial Fourier transformation, whose physical realization was already outlined in Section 4.4. In Section 5.3 we outline the proposed algorithm, and present a numerical demonstration on LG modes and their superpositions. Finally, we end with some concluding remarks in Section 5.4.

In Chapter 6 we propose a single-shot algorithm to retrieve phase from perturbed straight line fringes without phase unwrapping. In Section 6.2 we outline the proposed algorithm in extracting the gradients of phase from a measured interferogram using the Hilbert transform, and then the extraction of the phase from its gradients for the Hudgin geometry using the method of least squares. In Section 6.3 we explain how the matrix inversion of size $N^2 \times N^2$, appearing in the method of least squares, for a given interferogram of matrix size $N \times N$ could be performed using multiplication and sums of $N \times N$ matrices alone, and how it aids in speeding up the estimation process. In Section 6.4 we describe and summarize a numerical experiment that brings out the consistency of our proposed algorithm. Here, numerically generated interferograms corresponding to numerically generated random phases are considered. The phases are then estimated from these numerically generated interferograms using the proposed algorithm and then compared with the input numerically generated phases. The random phases are generated using techniques well known in the context of atmospheric turbulence [97, 98, 99, 100, 101, 102, 103, 104], and the numerically generated interferograms are accounted for the quasi-monochromaticity of the light field [38, 39, 2], and also the noise. In Section 6.5 the algorithm is implemented on interferograms measured in a Mach–Zehnder interferometer, through the insertion of a pseudo-random phase plate (PRPP) in one of its arms, to bring out the consistency of the proposed algorithm. We finally end with some concluding remarks in Section 6.6.

In Chapter 7 we conclude the thesis with few remarks and suggest possible future research directions.

Chapter 2

Review of ray and wave optics and the connection between them

2.1 Introduction

In this Chapter we first derive elementary optical transformations including free propagation and thin lens using the principles of ray optics. As is well known [39], these optical transformations can be represented using ray transfer matrices. We then derive wave optic equivalent of such optical transformations from Maxwell equations in the paraxial limit. We then show the correspondence between ray and wave optic versions of the optical transformations pertaining to a general FOOS using LCT. Finally we introduce the notion of OAM and derive relevant expressions, starting from the Maxwell equations, in the paraxial limit.

2.2 Ray transfer matrices of free propagation and thin lenses

In this Section we develop ray transfer matrices corresponding to the optical transformations : free propagation, thin convex lens, and thin cylindrical lens. Here, without loss of generality, we take z–axis to be optic axis. Further, a light ray is characterized by four parameters : distances from the optic axis in x and y coordinates, and angles between the ray and the optic axis in x–z and y–z planes. For symmetric FOOS, the ray transforms symmetrically in both x–z and y–z planes. It can be noted that free propagation, thin convex lens, and thin concave lenses are some examples of symmetric FOOS, and thin cylindrical lens is an example of asymmetric FOOS. First, we start with the free propagation transformation.

2.2.1 Free propagation

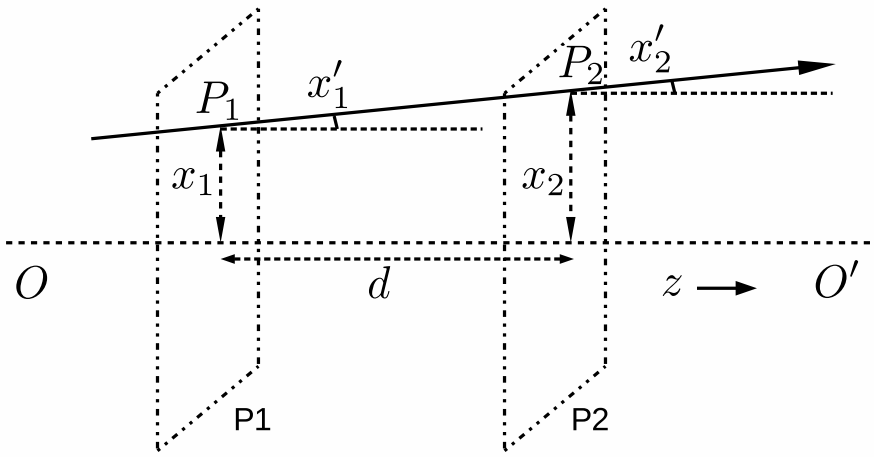

Figure 2.1: Shown here is the light ray traveling in the x–z plane from a point P_1 to another point P_2.

Consider a light ray traveling in the x–z plane from a point P_1 at transverse plane P1 to another point P_2 at transverse plane P2 (see Figure 2.1). These two points, P_1 and P_2, are located at distances x_1 and x_2 from the optical axis OO' respectively, and the distance between the planes P1 and P2 is d. Further, the angles made by the ray at points P_1 and P_2 are x'_1 and x'_2 respectively. With this, we readily see that

$$x_2 = x_1 + d\,\tan x'_1, \tag{2.1}$$

$$x'_2 = x'_1. \tag{2.2}$$

On applying paraxial approximation [39, 76], we have $\tan x'_1 \approx x'_1$, and hence Eqs. (2.1) and (2.2) can be written in matrix form as

$$\begin{bmatrix} x_2 \\ x'_2 \end{bmatrix} = \begin{bmatrix} 1 & d \\ 0 & 1 \end{bmatrix} \begin{bmatrix} x_1 \\ x'_1 \end{bmatrix} \equiv F(d) \begin{bmatrix} x_1 \\ x'_1 \end{bmatrix}, \tag{2.3}$$

where $F(d)$ is the ray transfer matrix corresponding to the free propagation by distance d in x–z plane. It is easy to see that the ray coordinates in the y–z plane also transform in the

same way as those in the x–z plane, and hence we can write

$$\begin{bmatrix} \mathsf{x}_2 \\ \mathsf{y}_2 \end{bmatrix} = \mathbf{F}(d) \begin{bmatrix} \mathsf{x}_1 \\ \mathsf{y}_1 \end{bmatrix}, \quad \text{where } \mathbf{F}(d) \equiv \begin{bmatrix} F(d) & 0 \\ 0 & F(d) \end{bmatrix}, \tag{2.4}$$

$\mathsf{x}_k = [x_k, x'_k]^T$, and $\mathsf{y}_k = [y_k, y'_k]^T$ with k being 1 or 2. Here, $\mathbf{F}(d)$ is the ray transfer matrix corresponding to the free propagation by a distance d.

Now we derive ray transfer matrix corresponding to a thin lens of focal length f. To do so, we first obtain ray optic transformation of a ray refracted at a spherical boundary of radius of curvature R separating two mediums with refractive indices n_1 and n_2, and follow it with lens maker's formula. With these, we get the ray transfer matrix of a lens with thickness ς. In the limit $\varsigma \to 0$, we arrive at the ray transfer matrix of the thin lens of focal length f.

2.2.2 Refraction at a spherical surface

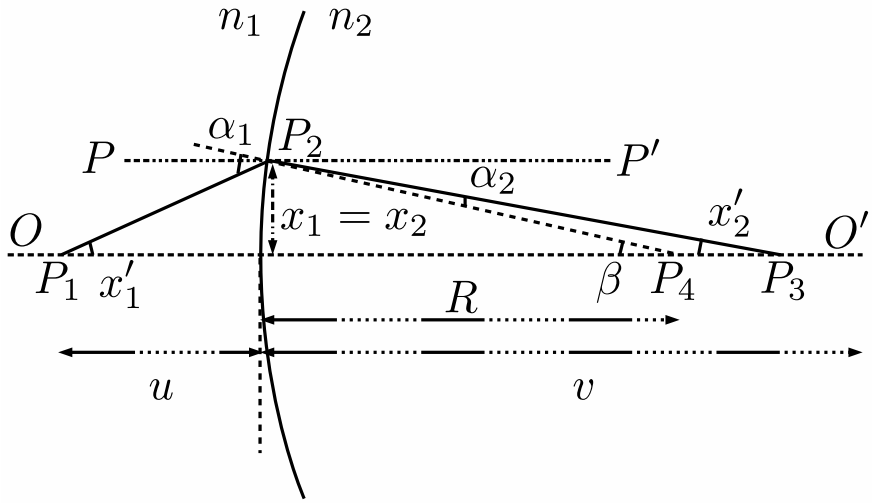

Figure 2.2: Shown here is refraction of a light ray at a spherical boundary separating mediums with refractive indices n_1 and n_2. The light ray traveling along the line P_1P_2 is refracted at the spherical boundary and travels along the line P_2P_3.

Consider a spherical surface of radius of curvature R separating two mediums with refractive indices n_1 and n_2 as shown in Figure 2.2. Suppose a ray traveling from P_1 reaches

P_2, gets refracted at the spherical boundary at P_2, and reaches P_3. At P_2, the input and output ray heights are x_1 and x_2 respectively with $x_1 = x_2$, and the respective angles they make with the optic axis OO' are $\angle P_1P_2P = x_1'$ and $\angle P_3P_2P' = x_2'$. Now by applying paraxial approximation and using sign convention [39], we see that

$$x_1' \approx \tan x_1' = -\frac{x_1}{u}, \tag{2.5}$$

$$x_2' \approx \tan x_2' = \frac{x_1}{v}, \tag{2.6}$$

$$\beta \approx \tan \beta = \frac{x_1}{R}. \tag{2.7}$$

By using Snell's law at P_2 [76] and invoking paraxial approximation once again, we obtain

$$n_1 \sin(x_1' + \beta) = n_2 \sin(\beta - x_2') \tag{2.8}$$

$$n_1 (x_1' + \beta) = n_2 (\beta - x_2'). \tag{2.9}$$

Now by using Eqs. (2.5)-(2.7) in Eq. (2.9) yields

$$\begin{aligned} n_1 \left(-\frac{x_1}{u} + \frac{x_1}{R}\right) &= n_2 \left(\frac{x_1}{R} - \frac{x_1}{v}\right) \\ \frac{n_2}{v} - \frac{n_1}{u} &= \frac{n_2 - n_1}{R}. \end{aligned} \tag{2.10}$$

Also, by using Eqs. (2.6) and (2.7) in Eq. (2.9), we readily obtain

$$\begin{aligned} n_1 \left(x_1' + \frac{x_1}{R}\right) &= n_2 \left(\frac{x_1}{R} - x_2'\right) \\ -x_2' &= \frac{1}{R}\left(\frac{n_1}{n_2} - 1\right) x_1 + \frac{n_1}{n_2} x_1'. \end{aligned} \tag{2.11}$$

Here, as the ray is traveling downwards and the angle is measured with respect to the optic axis OO', we place an extra minus sign before x_2'. Now, in view of Eq. (2.11), we have

$$\begin{bmatrix} x_2 \\ -x_2' \end{bmatrix} = \begin{bmatrix} 1 & 0 \\ \frac{1}{R}\left(\frac{n_1}{n_2} - 1\right) & \frac{n_1}{n_2} \end{bmatrix} \begin{bmatrix} x_1 \\ x_1' \end{bmatrix}. \tag{2.12}$$

That is, the ray transfer matrix corresponding to the spherical surface of radius of curvature

R separating two media with refractive indices n_1 and n_2 is

$$\begin{bmatrix} 1 & 0 \\ \frac{1}{R}\left(\frac{n_1}{n_2}-1\right) & \frac{n_1}{n_2} \end{bmatrix}. \tag{2.13}$$

2.2.3 Lens maker's formula

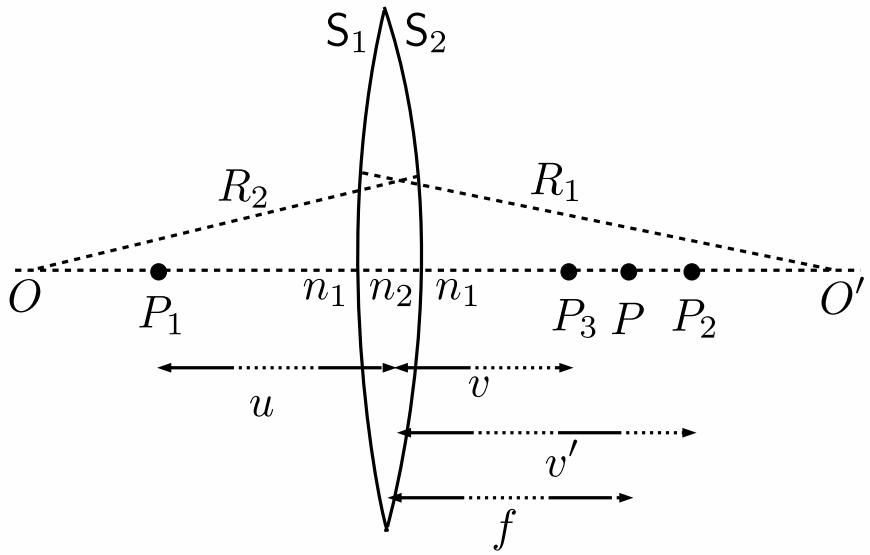

Figure 2.3: Shown here is a thin lens of focal length f. The image of the point object P_1 due to the surface S_1 is formed at P_2, and the image of P_2 due to the surface S_2 is formed at P_3.

Now we consider two spherical surfaces S_1 and S_2 with radii of curvature R_1 and R_2 respectively of a thin lens of focal length f as shown in Figure 2.3. Suppose the lens forms a point image P_3 (located at a distance v from the lens) of the point object P_1 (located at a distance u from the lens). Then, the lens maker's formula [105] relates u, v, and f as derived below. We now begin with the surface S_1 which forms the point image of P_1 at P_2 (located at a distance v' from the lens). Then by Eq. (2.10), we can write

$$\frac{n_2}{v'} - \frac{n_1}{u} = \frac{n_2 - n_1}{R_1}. \tag{2.14}$$

It is easy to observe that the image of P_2 due to S_2 is formed at P_3, and hence by Eq. (2.10),

we have

$$\frac{n_1}{v} - \frac{n_2}{v'} = \frac{n_1 - n_2}{R_2}. \tag{2.15}$$

Here, the extra minus sign before R_2 is due to sign convention. Now by adding Eqs. (2.14) and (2.15), we obtain

$$\begin{aligned} n_1 \left(\frac{1}{v} - \frac{1}{u}\right) &= (n_2 - n_1) \left(\frac{1}{R_1} - \frac{1}{R_2}\right) \\ \frac{1}{v} - \frac{1}{u} &= \left(\frac{n_2}{n_1} - 1\right) \left(\frac{1}{R_1} - \frac{1}{R_2}\right). \end{aligned} \tag{2.16}$$

Now suppose P_1 is moved very far in the left direction from the lens, i.e., $u \to \infty$. Then, all the rays originating from P_1 and reaching the lens will be parallel the optic axis OO', and will be focused at point P. So, Eq. (2.16) assumes the form

$$\frac{1}{f} = \left(\frac{n_2}{n_1} - 1\right) \left(\frac{1}{R_1} - \frac{1}{R_2}\right). \tag{2.17}$$

Eq. (2.17) is known as the lens maker's formula. By Eqs. (2.16) and (2.17), it is readily noted that

$$\frac{1}{f} = \frac{1}{v} - \frac{1}{u}. \tag{2.18}$$

2.2.4 Lens transformation matrix

We are now equipped with the relevant equations to derive the ray transfer matrix corresponding to a lens of thickness ς as shown in Figure 2.4. It has two spherical surfaces S_1 and S_2 whose radii of curvature are R_1 and R_2 respectively. Suppose, a ray traveling from left is refracted by S_1 at P_1, free propagates by distance ς in the lens, and gets refracted by S_2 at P_2. At P_1, by Eq. (2.12), the column vectors $[x_1, x_1']^T$ and $[x_2, x_2']^T$ are related by

$$\begin{bmatrix} x_2 \\ x_2' \end{bmatrix} = \begin{bmatrix} 1 & 0 \\ \frac{1}{R_1}\left(\frac{n_1}{n_2} - 1\right) & \frac{n_1}{n_2} \end{bmatrix} \begin{bmatrix} x_1 \\ x_1' \end{bmatrix}. \tag{2.19}$$

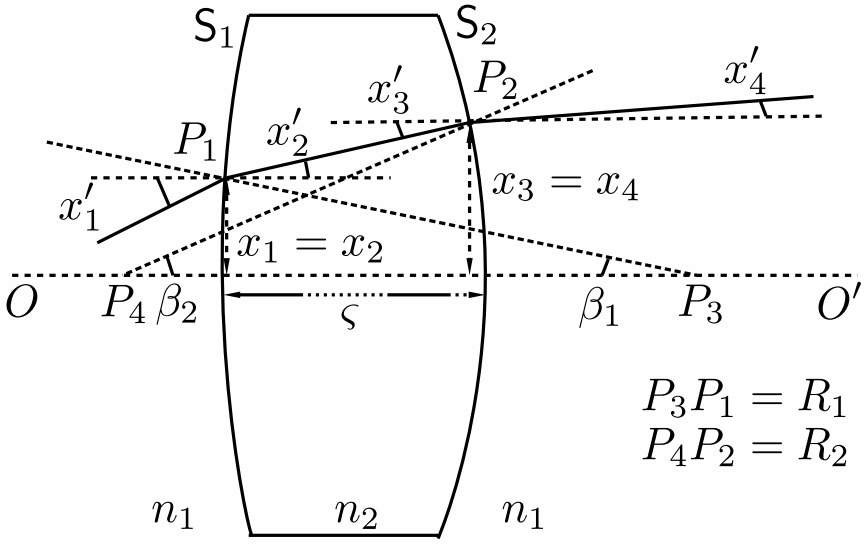

Figure 2.4: Shown here is a thick convex lens. A light ray traveling in the medium with refractive index n_1 is refracted by S_1 at P_1, and free propagates by distance ς along the line P_1P_2 in the lens before getting refracted by S_2 at P_2.

We see that the column vectors $[x_2, x_2']^T$ and $[x_3, x_3']^T$ are related by free propagation by distance ς, and hence by Eq. (2.3),

$$\begin{bmatrix} x_3 \\ x_3' \end{bmatrix} = \begin{bmatrix} 1 & \varsigma \\ 0 & 1 \end{bmatrix} \begin{bmatrix} x_2 \\ x_2' \end{bmatrix}. \tag{2.20}$$

Finally, at P_2, by Eq. (2.12), the column vectors $[x_3, x_3']^T$ and $[x_4, x_4']^T$ are related by

$$\begin{bmatrix} x_4 \\ x_4' \end{bmatrix} = \begin{bmatrix} 1 & 0 \\ \frac{1}{R_2}\left(\frac{n_2}{n_1} - 1\right) & \frac{n_2}{n_1} \end{bmatrix} \begin{bmatrix} x_3 \\ x_3' \end{bmatrix}. \tag{2.21}$$

Now by Eqs. (2.19), (2.20), and (2.21), we can write

$$\begin{bmatrix} x_4 \\ x_4' \end{bmatrix} = \begin{bmatrix} 1 & 0 \\ \frac{1}{R_2}\left(\frac{n_2}{n_1} - 1\right) & \frac{n_2}{n_1} \end{bmatrix} \begin{bmatrix} 1 & \varsigma \\ 0 & 1 \end{bmatrix} \begin{bmatrix} 1 & 0 \\ \frac{1}{R_1}\left(\frac{n_1}{n_2} - 1\right) & \frac{n_1}{n_2} \end{bmatrix} \begin{bmatrix} x_1 \\ x_1' \end{bmatrix}. \tag{2.22}$$

Thus, the ray transfer matrix corresponding to a thick lens as shown in Figure 2.4 is

$$L_\varsigma \equiv \begin{bmatrix} 1 & 0 \\ \frac{1}{R_2}\left(\frac{n_2}{n_1}-1\right) & \frac{n_2}{n_1} \end{bmatrix} \begin{bmatrix} 1 & \varsigma \\ 0 & 1 \end{bmatrix} \begin{bmatrix} 1 & 0 \\ \frac{1}{R_1}\left(\frac{n_1}{n_2}-1\right) & \frac{n_1}{n_2} \end{bmatrix} \tag{2.23}$$

For a thin lens, we have $\varsigma \to 0$, and hence

$$\begin{aligned} L_0 &= \begin{bmatrix} 1 & 0 \\ \frac{1}{R_2}\left(\frac{n_2}{n_1}-1\right) & \frac{n_2}{n_1} \end{bmatrix} \begin{bmatrix} 1 & 0 \\ \frac{1}{R_1}\left(\frac{n_1}{n_2}-1\right) & \frac{n_1}{n_2} \end{bmatrix} \\ &= \begin{bmatrix} 1 & 0 \\ \left(1-\frac{n_2}{n_1}\right)\left(\frac{1}{R_1}-\frac{1}{R_2}\right) & 1 \end{bmatrix}. \end{aligned} \tag{2.24}$$

But by substituting the lens maker's formula (see Eq. (2.17)) at Eq. (2.24), we readily obtain the transformation matrix of a thin convex lens of focal length f given by

$$L_0 \equiv L(f) = \begin{bmatrix} 1 & 0 \\ -\frac{1}{f} & 1 \end{bmatrix}. \tag{2.25}$$

For a thin concave lens of focal length f, we replace f in Eq. (2.25) with $-f$. Clearly, as the ray coordinates transform symmetrically in x–z and y–z planes under the action of thin lens of focal length f, we have

$$\begin{bmatrix} \mathsf{x}_2 \\ \mathsf{y}_2 \end{bmatrix} = \mathbf{L}(f) \begin{bmatrix} \mathsf{x}_1 \\ \mathsf{y}_1 \end{bmatrix}, \text{ where } \mathbf{L}(f) \equiv \begin{bmatrix} L(f) & 0 \\ 0 & L(f) \end{bmatrix}, \tag{2.26}$$

$\mathsf{x}_k = [x_k, x'_k]^T$, and $\mathsf{y}_k = [y_k, y'_k]^T$ with k being 1 or 2.

2.2.5 Thin cylindrical lenses

Thin cylindrical lens of focal length f is perhaps the simplest example in which the ray coordinates in the x–z and y–z planes transform asymmetrically. Let us consider a thin cylindrical lens of focal length f_x as shown in Figure 2.5, where the curvature is in the x direction. This behaves like a thin lens of focal length f_x in the x–z plane and does not affect the rays traveling in y–z plane. Then it can readily be seen that

$$\begin{bmatrix} \mathsf{x}_2 \\ \mathsf{y}_2 \end{bmatrix} = \begin{bmatrix} L(f_x) & 0 \\ 0 & \mathbb{1} \end{bmatrix} \begin{bmatrix} \mathsf{x}_1 \\ \mathsf{y}_1 \end{bmatrix}, \tag{2.27}$$

where $\mathbb{1}$ is the identity matrix in two dimensions. Now consider two cylindrical lenses of the same focal length f placed such that their curvatures are in the x and y directions respectively. Then their respective ray transfer matrices are

$$\mathbf{L}_x(f) \equiv \begin{bmatrix} L(f) & 0 \\ 0 & \mathbb{1} \end{bmatrix}, \text{ and } \mathbf{L}_y(f) \equiv \begin{bmatrix} \mathbb{1} & 0 \\ 0 & L(f) \end{bmatrix}. \tag{2.28}$$

Note that as in the symmetric situation, $f > 0\,(f < 0)$ denotes that the lens is convex (concave).

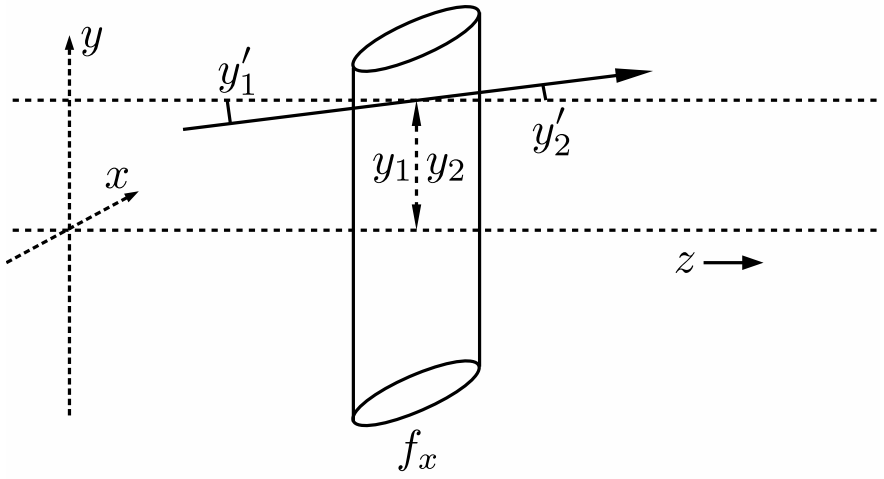

Figure 2.5: Shown here is a thin cylindrical lens of focal length f_x whose curvature is in the x-direction.

Having derived ray transfer matrices for the optical transformations (free propagation and thin lenses), we now set out to derive such transformations using wave optics in the paraxial limit in Sections 2.3, 2.4, and 2.5.

2.3 Paraxial wave equation and its solutions

In this Section we derive wave equation from Maxwell equations, obtain the paraxial version, and discuss its solutions.

2.3.1 Maxwell equations

As is well known, in free space, i.e., in regions where electrostatic charges and current are absent, Maxwell equations [106] are given by

$$\nabla \cdot \mathbf{E} = 0, \tag{2.29}$$

$$\nabla \cdot \mathbf{B} = 0, \tag{2.30}$$

$$\nabla \times \mathbf{E} = -\frac{\partial \mathbf{B}}{\partial t}, \tag{2.31}$$

$$\nabla \times \mathbf{B} = \mu_0 \, \epsilon_0 \, \frac{\partial \mathbf{E}}{\partial t}. \tag{2.32}$$

Here, $\nabla = \hat{i} \, \frac{\partial}{\partial x} + \hat{j} \, \frac{\partial}{\partial y} + \hat{k} \, \frac{\partial}{\partial z}$, $\mathbf{E}$ is electric field (with units $\mathrm{kg\,m\,s^{-2}\,C^{-1}}$), $\mathbf{B}$ is magnetic field (with units $\mathrm{kg\,s^{-2}\,A^{-1}}$), ϵ_0 is permittivity of free space ($8.85 \times 10^{-12}\,\mathrm{m^{-3}\,kg^{-1}\,s^4\,A^2}$), μ_0 is permeability of free space ($4\pi \times 10^{-7}\,\mathrm{m\,kg\,s^{-2}\,A^{-2}}$), and t is time (with units s).

2.3.2 Wave equation in free space

The wave equation in free space can readily be obtained from Maxwell equations using vector calculus identities [107] as follows. Applying curl operation on both sides of Eq. (2.31), and by using Eqs. (2.29) and (2.32), we readily obtain

$$\begin{aligned} \nabla \times (\nabla \times \mathbf{E}) &= -\frac{\partial}{\partial t} (\nabla \times \mathbf{B}) \\ \nabla (\nabla \cdot \mathbf{E}) - \nabla^2 \mathbf{E} &= -\mu_0 \, \epsilon_0 \, \frac{\partial^2 \mathbf{E}}{\partial t^2} \\ \nabla^2 \mathbf{E} &= \mu_0 \, \epsilon_0 \, \frac{\partial^2 \mathbf{E}}{\partial t^2}. \end{aligned} \tag{2.33}$$

Similarly, it can be easily shown that

$$\nabla^2 \mathbf{B} = \mu_0 \, \epsilon_0 \, \frac{\partial^2 \mathbf{B}}{\partial t^2}. \tag{2.34}$$

Because the velocity of light $c = 1/\sqrt{\mu_0 \, \epsilon_0} = 3 \times 10^8\,\mathrm{m\,s^{-1}}$, the fields $\mathbf{E}$ and $\mathbf{B}$ satisfy the partial differential equation

$$\nabla^2 \Psi = \frac{1}{c^2} \, \frac{\partial^2 \Psi}{\partial t^2}, \tag{2.35}$$

where Ψ is a scalar function of space-time variables. Clearly, Eq. (2.35) is the well known three-dimensional wave equation.

2.3.3 Paraxial wave equation

Assuming that Ψ (Eq. (2.35)) is separable in space variables and time, we write

$$\Psi = \Psi_s(x, y, z)\, \Psi_t(t), \tag{2.36}$$

where Ψ_s and Ψ_t are purely functions of space and time respectively. Now, plugging Eq. (2.36) in Eq. (2.35), we obtain

$$\frac{1}{\Psi_s} \nabla^2 \Psi_s = \frac{1}{c^2} \frac{1}{\Psi_t} \frac{\mathrm{d}^2 \Psi_t}{\mathrm{d}t^2}. \tag{2.37}$$

Here, LHS is purely a function of space variables while RHS is purely a function of time. Hence, they must both equal to some constant, say $-\kappa^2$. So,

$$\frac{1}{\Psi_s} \nabla^2 \Psi_s = \frac{1}{c^2} \frac{1}{\Psi_t} \frac{\mathrm{d}^2 \Psi_t}{\mathrm{d}t^2} = -\kappa^2. \tag{2.38}$$

Now, we readily obtain

$$\nabla^2 \Psi_s = -\kappa^2\, \Psi_s, \tag{2.39}$$

$$\frac{\mathrm{d}^2 \Psi_t}{\mathrm{d}t^2} = -\omega^2\, \Psi_t. \tag{2.40}$$

Here, Eq. (2.39) is known as Helmholtz's equation, and $\omega = \kappa\, c$. For a monochromatic wave field ($\kappa = 2\pi/\lambda$ with λ being the wavelength), it is readily noted that the solution of Eq. (2.40) is given by

$$\Psi_t = \exp\left(-i\omega t\right). \tag{2.41}$$

If Ψ_s (Eq. (2.39)) is traveling in directions which make small angles with the z axis, it can be approximated as [108]

$$\Psi_s(x, y, z) \approx \psi(x, y; z)\, \exp\left(i\kappa z\right), \tag{2.42}$$

where $\psi(x, y; z)$ slowly varies with respect to z. Now, by substituting Eq. (2.42) in Eq. (2.39), we obtain

$$\exp\left(i\kappa z\right) \left[\left(\frac{\partial^2}{\partial x^2} + \frac{\partial^2}{\partial y^2} \right) \psi + \frac{\partial^2 \psi}{\partial z^2} + 2i\kappa \frac{\partial \psi}{\partial z} \right] = 0. \tag{2.43}$$

As ψ is a slowly varying function in z, we drop $\frac{\partial^2\psi}{\partial z^2}$, the second derivative term in z, to obtain

$$\exp(i\kappa z)\left(\frac{\partial^2\psi}{\partial x^2}+\frac{\partial^2\psi}{\partial y^2}+2i\kappa\frac{\partial\psi}{\partial z}\right)=0. \tag{2.44}$$

Because the above differential equation holds true for any arbitrary z, we require

$$\frac{\partial^2\psi}{\partial x^2}+\frac{\partial^2\psi}{\partial y^2}+2i\kappa\frac{\partial\psi}{\partial z}=0. \tag{2.45}$$

This equation is the well known paraxial wave equation or *paraxial Helmholtz equation*[108, 76]. Note that in cylindrical coordinates [106, 107] $(r-\theta-z)$ with $r=\sqrt{x^2+y^2}$ and $\theta=\tan^{-1}(y/x)$ (at a given z), Eq. (2.45) assumes the form

$$\frac{\partial^2\psi}{\partial r^2}+\frac{1}{r}\frac{\partial\psi}{\partial r}+\frac{1}{r^2}\frac{\partial^2\psi}{\partial\theta^2}+2i\kappa\frac{\partial\psi}{\partial z}=0. \tag{2.46}$$

Now we discuss the solutions of Eqs. (2.45) and (2.46).

2.3.4 Solutions of the paraxial wave equation

The solutions of Eq. (2.45) are the well known Hermite-Gaussian (HG) modes [76], and are given as

$$\begin{aligned}\psi_{m_1m_2}(x,y;z)=\sqrt{\frac{2}{\pi}}\frac{1}{\sqrt{2^{m_1+m_2}\,m_1!\,m_2!}}\frac{1}{w(z)}H_{m_1}\left(\frac{\sqrt{2}\,x}{w(z)}\right)H_{m_2}\left(\frac{\sqrt{2}\,y}{w(z)}\right)\\ \times\exp\left[-(x^2+y^2)\left(\frac{1}{w(z)^2}-\frac{i\kappa}{2R(z)}\right)-i\,(m_1+m_2+1)\,\zeta(z)\right].\end{aligned} \tag{2.47}$$

Here, $H_{m_1}(\cdot)$ is the Hermite polynomial,

$$w(z)^2=w(0)^2\left(1+\frac{z^2}{z_r^2}\right), \tag{2.48}$$

$$R(z)=z\left(1+\frac{z_r^2}{z^2}\right), \tag{2.49}$$

$$\zeta(z)=\tan^{-1}\left(\frac{z}{z_r}\right), \tag{2.50}$$

with $w(0)$ being the width of the wave field at $z=0$, and $z_r=\kappa w(0)^2/2$ is known as the *Rayleigh range* [76, 109]. Further, $w(z)$ and $R(z)$ refer to width and radius of curvature of

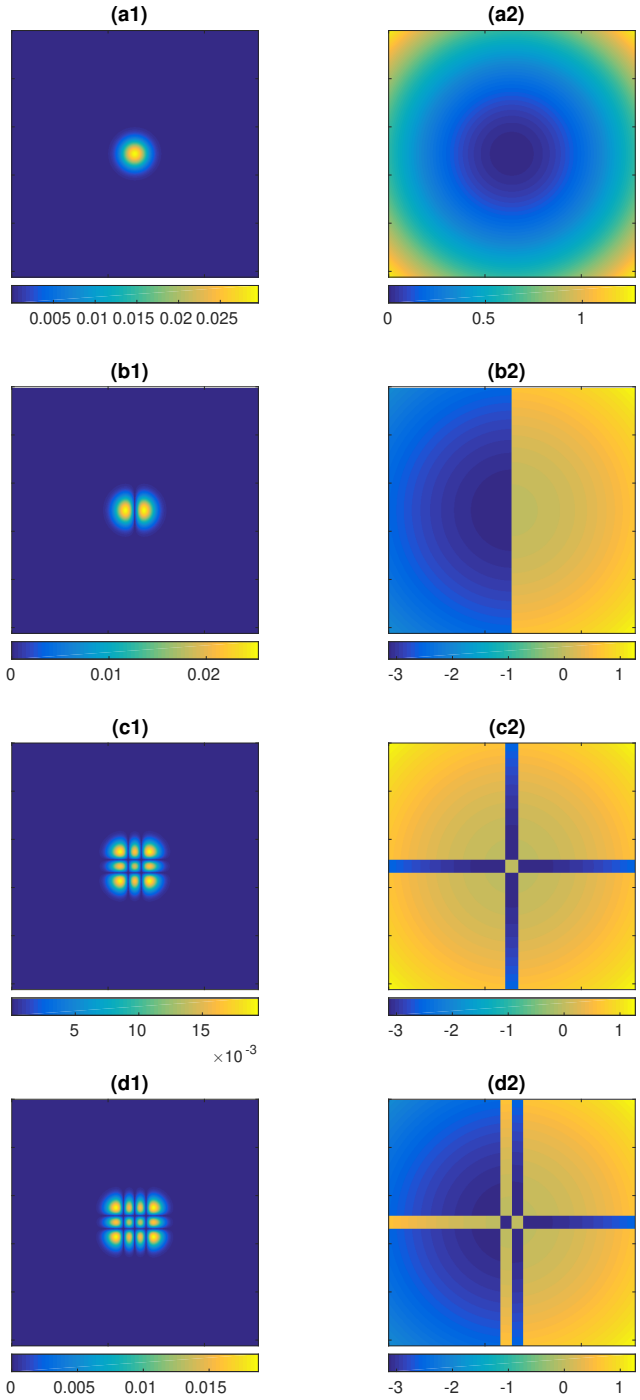

Figure 2.6: Shown here are amplitude and phase profiles of some HG modes (see Eq. (2.47)). While (a1), (b1), (c1), and (d1) plot the amplitude profiles of $\psi_{00}(x, y; z)$, $\psi_{10}(x, y; z)$, $\psi_{22}(x, y; z)$, and $\psi_{32}(x, y; z)$ respectively, (a2), (b2), (c2), and (d2) plot their respective phase profiles.

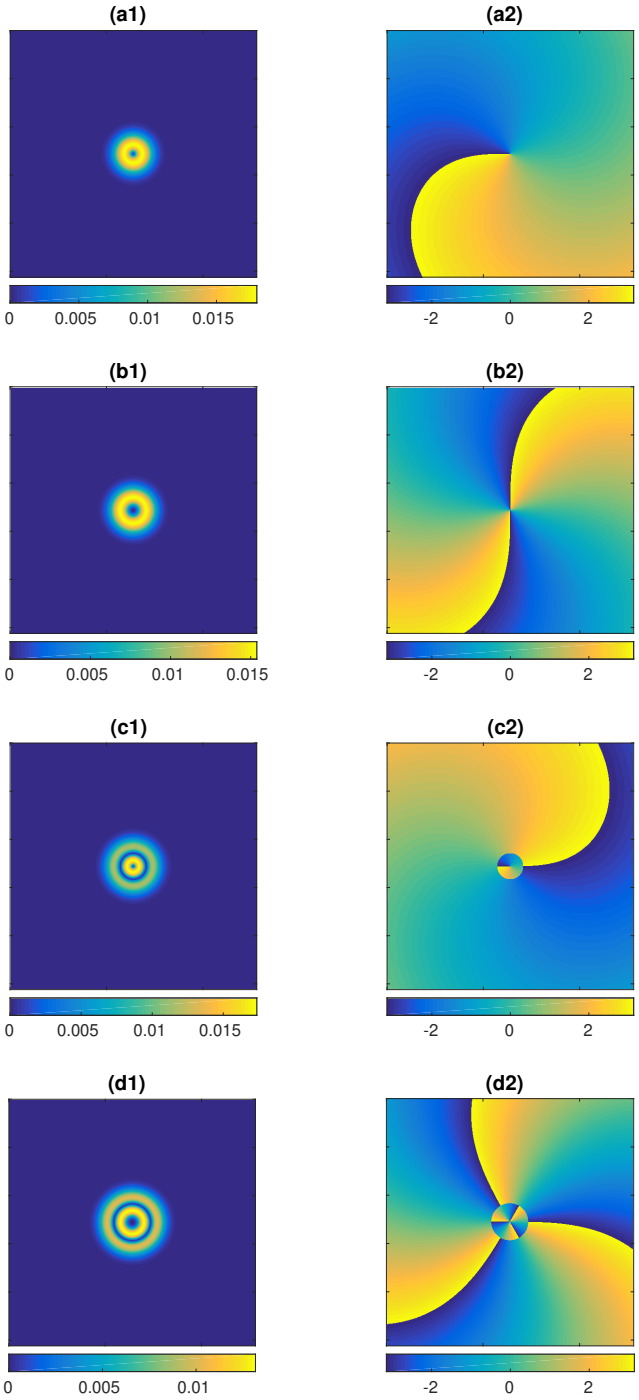

Figure 2.7: Shown here are amplitude and phase profiles of some LG modes (see Eq. (2.51)). While (a1), (b1), (c1), and (d1) plot the amplitude profiles of $\psi_0^1(x, y; z)$, $\psi_0^{-2}(x, y; z)$, $\psi_1^1(x, y; z)$, and $\psi_1^{-3}(x, y; z)$ respectively, (a2), (b2), (c2), and (d2) plot their respective phase profiles.

the wave field at a distance z respectively. Finally, the extra phase factor $(m_1+m_2+1)\zeta(z)$, acquired by the light field while traveling in z–direction is known as the *Gouy phase* [39].

Now, for the case of Eq. (2.46), the solutions are Laguerre-Gaussian (LG) modes and are given by

$$\psi_p^l(r,\theta;z) = \frac{\sqrt{2}}{\sqrt{\pi}\,w(z)}\left[\frac{p!}{(p+|l|)!}\right]^{\frac{1}{2}}\left[\frac{\sqrt{2}\,r}{w(z)}\right]^{|l|} L_p^{|l|}\left(\frac{2r^2}{w^2(z)}\right) \times \exp\left[-r^2\left(\frac{1}{w(z)^2}-\frac{i\kappa}{2R(z)}\right)+i\,l\theta-i\,(|l|+2p+1)\,\zeta(z)\right], \tag{2.51}$$

where $L_p^l(\cdot)$ is the associated Laguerre polynomial.

2.4 Fresnel-Kirchhoff diffraction integral

Now we derive the wave optic version of free propagation by distance d from the paraxial wave equation (Eq. (2.45)). The solution of Eq. (2.45) is given by [110]

$$\psi(\mathbf{x};z) = \exp\left[\frac{id}{2\kappa}\left(\frac{\partial^2}{\partial x^2}+\frac{\partial^2}{\partial y^2}\right)\right]\psi(\mathbf{x};z_0), \tag{2.52}$$

where $\mathbf{x}=(x,y)$ and $d=z-z_0$. For brevity, we first solve

$$\psi(x;z) = \exp\left[\frac{id}{2\kappa}\frac{\partial^2}{\partial x^2}\right]\psi(x;z_0), \tag{2.53}$$

Fourier decomposing $\psi(x;z)$ and $\psi(x;z_0)$, we respectively obtain

$$\psi(x;z) = \frac{1}{\sqrt{2\pi}}\int_{-\infty}^{\infty}\mathrm{d}\tilde{x}\,e^{ix\,\tilde{x}}\,\tilde{\psi}(\tilde{x},z), \tag{2.54}$$

$$\psi(x;z_0) = \frac{1}{\sqrt{2\pi}}\int_{-\infty}^{\infty}\mathrm{d}\tilde{x}\,e^{ix\,\tilde{x}}\,\tilde{\psi}(\tilde{x},z_0). \tag{2.55}$$

Here, the inverse relations are

$$\tilde{\psi}(\tilde{x},z) = \frac{1}{\sqrt{2\pi}}\int_{-\infty}^{\infty}\mathrm{d}x\,e^{-ix\,\tilde{x}}\,\psi(x;z), \tag{2.56}$$

$$\tilde{\psi}(\tilde{x}, z_0) = \frac{1}{\sqrt{2\pi}} \int_{-\infty}^{\infty} \mathrm{d}x \, e^{-ix\,\tilde{x}} \, \psi(x; z_0). \tag{2.57}$$

Plugging Eqs. (2.54) and (2.55) in Eq. (2.53) we obtain

$$\frac{1}{\sqrt{2\pi}} \int_{-\infty}^{\infty} \mathrm{d}\tilde{x} \left\{ \tilde{\psi}(\tilde{x}, z) - \exp\left(\frac{-id}{2\kappa}\,\tilde{x}^2\right) \tilde{\psi}(\tilde{x}, z_0) \right\} e^{ix\,\tilde{x}} = 0. \tag{2.58}$$

Since this equation must hold for any x, we require

$$\begin{aligned} \tilde{\psi}(\tilde{x}, z) &= \exp\left(\frac{-id}{2\kappa}\,\tilde{x}^2\right) \tilde{\psi}(\tilde{x}, z_0) \\ &= \frac{1}{\sqrt{2\pi}} \exp\left(\frac{-id}{2\kappa}\,\tilde{x}^2\right) \int_{-\infty}^{\infty} \mathrm{d}x_1 \, e^{-ix_1\,\tilde{x}} \, \psi(x_1; z_0). \end{aligned} \tag{2.59}$$

Here we have used Eq. (2.57). Now by using Eq. (2.59) in Eq. (2.54), we obtain

$$\begin{aligned} \psi(x; z) &= \frac{1}{2\pi} \int_{-\infty}^{\infty} \mathrm{d}\tilde{x} \, e^{ix\,\tilde{x}} \, \exp\left(\frac{-id}{2\kappa}\,\tilde{x}^2\right) \int_{-\infty}^{\infty} \mathrm{d}x_1 \, e^{-ix_1\,\tilde{x}} \, \psi(x_1; z_0) \\ &= \frac{1}{2\pi} \int_{-\infty}^{\infty} \mathrm{d}x_1 \, \psi(x_1; z_0) \int_{-\infty}^{\infty} \mathrm{d}\tilde{x} \, \exp\left[\frac{-id}{2\kappa}\,\tilde{x}^2 + i\tilde{x}\,(x - x_1)\right] \\ &= \frac{1}{2\pi} \int_{-\infty}^{\infty} \mathrm{d}x_1 \, \psi(x_1; z_0) \times \exp\left(-i\pi/4\right) \sqrt{\frac{2\pi\kappa}{d}} \, \exp\left[\frac{i\kappa}{2d}\,(x - x_1)^2\right] \\ &= \frac{\exp\left(-i\pi/4\right)}{\sqrt{\lambda\, d}} \int_{-\infty}^{\infty} \mathrm{d}x_1 \, \exp\left[\frac{i\kappa}{2d}\,(x - x_1)^2\right] \psi(x_1; z_0). \end{aligned} \tag{2.60}$$

Then, the solution of Eq. (2.52) is

$$\psi(\mathbf{x}; z) = \frac{1}{i\lambda\, d} \int_{-\infty}^{\infty} \int_{-\infty}^{\infty} \mathrm{d}x_1 \, \mathrm{d}y_1 \, \exp\left\{\frac{i\kappa}{2d}\left[(x - x_1)^2 + (y - y_1)^2\right]\right\} \psi(\mathbf{x}_1; z_0). \tag{2.61}$$

Here we remark that while Eq. (2.4) is the ray optic version of free propagation by distance d, Eq. (2.61) is the wave optic version of the same. It can be noted that Eq. (2.61) can also

be written as

$$\psi(\mathbf{x};z) = \int_{-\infty}^{\infty}\int_{-\infty}^{\infty} \psi(\mathbf{x}_1;z_0)\, h(\mathbf{x}-\mathbf{x}_1)\, \mathrm{d}x_1\, \mathrm{d}y_1, \quad \text{where} \tag{2.62}$$

$$h(\mathbf{x}) = \frac{1}{i\lambda d}\, \exp\left[\frac{i\kappa}{2d}\,(x^2+y^2)\right]. \tag{2.63}$$

That is, $\psi(\mathbf{x};z)$ is just the two dimensional convolution of $\psi(\mathbf{x}_1;z_0)$ and $h(\mathbf{x})$.

2.5 Transformation of wave field due to thin lens

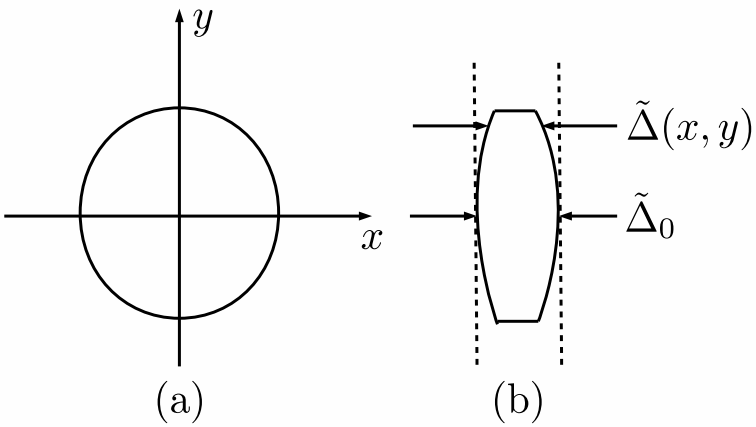

Figure 2.8: Frame (a) is the front view of the lens while frame (b) is the side view of the same.

In this Section we obtain the wave optic version of the optical transformation corresponding to a thin lens of focal length f in the paraxial limit. Since refractive index of the thin lens is n, the wave field passing through it is delayed more in the middle than at the edges. Suppose the thickness of the lens at the axis be $\tilde{\Delta}_0$ and $\tilde{\Delta}(x,y)$ at (x,y) (see Frame (b) of Figure 2.8). Then the total phase delay is given by

$$\phi(x,y) = \kappa\, n\, \tilde{\Delta}(x,y) + \kappa\, [\tilde{\Delta}_0 - \tilde{\Delta}(x,y)]. \tag{2.64}$$

By Frame (b) of Figure 2.8, it is easy to see that the lens provides a phase delay $\kappa\, n\, \tilde{\Delta}(x,y)$

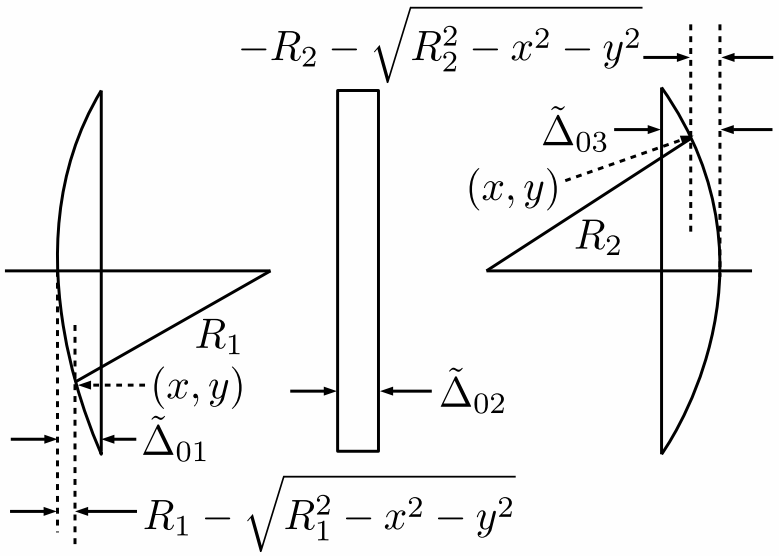

Figure 2.9: The side view of the lens shown in the frame (b) of Figure 2.8 is split into two curved parts and a flat part to calculate its thickness function.

while the region free of lens between the two planes provides a phase delay $\kappa\,[\tilde{\Delta}_0 - \tilde{\Delta}(x, y)]$. Then the phase transformation of the lens can be represented by [108]

$$\mathcal{L}_f(x, y) = \exp\left(i\kappa\,\tilde{\Delta}_0\right)\,\exp\left[i\kappa\,(n-1)\,\tilde{\Delta}(x, y)\right]. \tag{2.65}$$

Let the paraxial wave field at the entry and exit planes be $\psi_1(x, y)$ and $\psi_2(x, y)$ respectively. Then we readily have

$$\psi_2(x, y) = \mathcal{L}_f(x, y)\,\psi_1(x, y). \tag{2.66}$$

Now to calculate $\tilde{\Delta}(x, y)$, we can consider that the lens is made up of three parts as shown in Figure 2.9. Thus,

$$\begin{aligned}\tilde{\Delta}(x, y) &= \tilde{\Delta}_{01} - \left(R_1 - \sqrt{R_1^2 - x^2 - y^2}\right) + \tilde{\Delta}_{02} + \tilde{\Delta}_{03} - \left(-R_2 - \sqrt{R_2^2 - x^2 - y^2}\right) \\ &= \tilde{\Delta}_0 - R_1\left(1 - \sqrt{1 - \frac{x^2 + y^2}{R_1^2}}\right) + R_2\left(1 - \sqrt{1 - \frac{x^2 + y^2}{R_2^2}}\right),\end{aligned} \tag{2.67}$$

where $\tilde{\Delta}_0 = \tilde{\Delta}_{01} + \tilde{\Delta}_{02} + \tilde{\Delta}_{03}$. By invoking paraxial approximation,

$$\begin{aligned}\tilde{\Delta}(x,y) &\approx \tilde{\Delta}_0 - R_1\left\{1 - \left[1 - \frac{(x^2+y^2)}{2R_1^2}\right]\right\} + R_2\left\{1 - \left[1 - \frac{(x^2+y^2)}{2R_1^2}\right]\right\} \\ &= \tilde{\Delta}_0 - \frac{(x^2+y^2)}{2}\left(\frac{1}{R_1} - \frac{1}{R_2}\right). \end{aligned} \tag{2.68}$$

Substituting Eq. (2.68) in Eq. (2.65) we obtain

$$\begin{aligned}\mathcal{L}_f(x,y) &= \exp\left(i\kappa\, n\, \Delta_0\right) \exp\left[-i\kappa\,(n-1)\,\frac{(x^2+y^2)}{2}\left(\frac{1}{R_1} - \frac{1}{R_2}\right)\right] \\ &= \exp\left(i\kappa\, n\, \tilde{\Delta}_0\right) \exp\left[\frac{-i\kappa}{2f}\,(x^2+y^2)\right]. \end{aligned} \tag{2.69}$$

Here, we have made use of the lens maker's formula (Eq. (2.17)) with the assumption that $n_2 = n$ and $n_1 = 1$. Discarding the overall factor $\exp\left(i\kappa\, n\, \tilde{\Delta}_0\right)$, the lens transformation is

$$\mathcal{L}_f(x,y) = \exp\left[\frac{-i\kappa}{2f}\,(x^2+y^2)\right]. \tag{2.70}$$

It can be observed that Eq. (2.26) is the ray optic version of the thin lens transformation, and Eq. (2.70) is the wave optic version of the same.

2.5.1 Numerical free propagation

Here, we discuss how free propagation by distance d is implemented numerically in MATLAB. Say, we are given the wave field $\psi(\mathbf{x}_1; z_0)$, and wish to compute the wave field $\psi(\mathbf{x}; z)$ (see Eq. (2.62)). Let the Fourier transforms of $\psi(\mathbf{x}_1; z_0)$ and $h(\mathbf{x})$ (see Eq. (2.63)) be $\tilde{\psi}(\tilde{\mathbf{x}}_1; z_0)$ and $\tilde{h}(\tilde{\mathbf{x}})$ respectively, where

$$\tilde{h}(\tilde{\mathbf{x}}) = \exp\left[-i\pi\lambda d\,(\tilde{x}^2 + \tilde{y}^2)\right]. \tag{2.71}$$

Then by convolution theorem [108], inverse Fourier transforming the function $\tilde{\psi}(\tilde{\mathbf{x}}_1; z_0) \times \tilde{h}(\tilde{\mathbf{x}})$, we can obtain $\psi(\mathbf{x}; z)$. We note in passing that $\tilde{h}(\tilde{\mathbf{x}})$ of Eq. (2.71) acts as a lens in the Fourier plane (cf. Eq. (2.69)).

Now the numerical implementation is done as follows. Let the transverse planes x–y and $\tilde{x}$–$\tilde{y}$ both contain $N \times N$ pixels with respective screen dimensions $\mathfrak{L} \times \mathfrak{L}\,\mathrm{m}^2$ and $N\mathfrak{L}^{-1} \times N\mathfrak{L}^{-1}\,\mathrm{m}^{-2}$. Clearly, the spacing between two adjacent pixels are $\mathfrak{L}/N$ and $\mathfrak{L}^{-1}$ respectively for x–y and $\tilde{x}$–$\tilde{y}$. First we compute $\tilde{\psi}(\tilde{\mathbf{x}}_1; z_0)$, i.e., the Fourier transform of

$\psi(\mathbf{x}_1; z_0)$. Let $\psi_{z_0}(j,k)$ be the discrete $N \times N$ matrix associated with $\psi(\mathbf{x}_1; z_0)$, where the dummy indices j and k each run from 1 through N. Also, $\mathfrak{F}(j,k)$ be the discrete $N \times N$ matrix obtained through applying the `fftshift` operation to both rows and column of the discrete Fourier transform matrix of size $N \times N$. Then

$$\tilde{\psi}_{z_0}(j,k) = \mathfrak{F}(j,k) * \psi_{z_0}(j,k) * \mathfrak{F}(j,k), \tag{2.72}$$

where $\tilde{\psi}_{z_0}(j,k)$ is the discrete $N \times N$ matrix associated with $\tilde{\psi}(\tilde{\mathbf{x}}_1; z_0)$. Now we point-wise multiply $\tilde{\psi}_{z_0}(j,k)$ with $\tilde{h}(j,k)$, where $\tilde{h}(j,k)$ is the discrete $N \times N$ matrix associated with $\tilde{h}(\tilde{\mathbf{x}})$ (see Eq. (2.71)). Inverse Fourier transform of the resultant matrix gives us $\psi_z(j,k)$, the discrete $N \times N$ matrix associated with $\psi(\mathbf{x}; z)$.

2.6 Linear canonical transforms and the relationship between ray and wave optics

In previous Sections, we have obtained optical transformations corresponding to free propagation and thin lens using ray and wave optics in the paraxial limit. In this Section we provide the explicit connection between any optical transformation corresponding to a general FOOS expressed using ray and wave optics in the paraxial limit. Suppose a paraxial wave field $\psi(x, y; z)$ undergoes a unitary transformation given by

$$\psi(x, y; z) \to \mathcal{U}\, \psi(x, y; z), \tag{2.73}$$

where $\mathcal{U}$ is generated by the most general quadratic in the operators $\hat{x}$, $\hat{p}_x$, $\hat{y}$, and $\hat{p}_y$ [111]. In fact, as seen through Refs. [111, 112], such a unitary transformation $\mathcal{U}$ is in correspondence with a symplectic matrix $\mathbf{S} \in Sp(4, \mathbb{R})$, i.e., $\mathcal{U} \equiv \mathcal{U}(\mathbf{S})$. For instance, let $\hat{\xi} = [\hat{x}, \hat{p}_x, \hat{y}, \hat{p}_y]^T$, then

$$\mathcal{U}(\mathbf{S})\, \hat{\xi}\, \mathcal{U}^\dagger(\mathbf{S}) = \mathbf{S}^{-1}\, \hat{\xi}, \text{ where} \tag{2.74}$$

$$\mathbf{S}\, \Sigma\, \mathbf{S}^T = \Sigma, \text{ with } \Sigma = \Omega \oplus \Omega, \text{ and} \tag{2.75}$$

$$\Omega = \begin{bmatrix} 0 & 1 \\ -1 & 0 \end{bmatrix}. \tag{2.76}$$

In other words, $\mathbf{S}$ is a linear canonical transformation [113, 114]. Note that in Eq. (2.75), '$\oplus$' refers to direct sum of matrices. It is readily seen by Eq. (2.74) that both $\mathcal{U}(\mathbf{S})$ and

$-\mathcal{U}(\mathbf{S})$ are mapped to the same $\mathbf{S}$. In other words, there exists a two-to-one correspondence between $\mathcal{U}(\mathbf{S})$ and $\mathbf{S}$ [111, 112]. And as well known, any $\mathbf{S} \in Sp(4,\mathbb{R})$ can be characterized by ten independent parameters [111, 96]. Here, $\det \mathbf{S} = 1$ reflects the fact that the refractive indices of the medium for the input and output field amplitudes are the same.

Now we consider two examples of the unitary operator $\mathcal{U}$. First we start with

$$\mathcal{F}_d = \exp\left[\frac{-id\kappa}{2}\,(\hat{p}_x^2 + \hat{p}_y^2)\right], \tag{2.77}$$

where

$$\hat{p}_x = \frac{-i}{\kappa}\frac{\partial}{\partial x}, \;\text{ and }\; \hat{p}_y = \frac{-i}{\kappa}\frac{\partial}{\partial y}, \tag{2.78}$$

in the position representation [115]. Clearly, $\mathcal{F}_d$ is the free propagation unitary

$$\exp\left[\frac{id}{2\kappa}\left(\frac{\partial^2}{\partial x^2} + \frac{\partial^2}{\partial y^2}\right)\right]$$

in the position representation (see Eq. (2.52)). Now, if $\mathcal{U} = \mathcal{F}_d$, then Eq. (2.74) reads as

$$\mathcal{F}_d\,\hat{\xi}\,\mathcal{F}_d^\dagger = \mathbf{F}^{-1}(d)\,\hat{\xi}, \tag{2.79}$$

where we immediately recognize by Eq. (2.4) that $\mathbf{F}(d)$ is the ray transfer matrix corresponding to the free propagation by distance d. The second unitary operator we consider is

$$\mathcal{L}_f = \exp\left[\frac{-i\kappa}{2f}\,(\hat{x}^2 + \hat{y}^2)\right] \equiv \mathcal{L}_f^x \otimes \mathcal{L}_f^y, \tag{2.80}$$

where

$$\hat{x} = x, \;\text{ and }\; \hat{y} = y \tag{2.81}$$

in the position representation. To this end, we note that $\mathcal{L}_f^x$ and $\mathcal{L}_f^y$ (see Eq. (2.80)) act respectively on the operators $[\hat{x}, \hat{p}_x]^T$ and $[\hat{y}, \hat{p}_y]^T$ alone. Likewise, if $\mathcal{U} = \mathcal{L}_f$, then

$$\mathcal{L}_f\,\hat{\xi}\,\mathcal{L}_f^\dagger = \mathbf{L}^{-1}(f)\,\hat{\xi}. \tag{2.82}$$

Here, by Eq. (2.26), it is easy to see that $\mathbf{L}(f)$ is the ray transfer matrix corresponding to the

thin lens of focal length f. Note that for the unitary operators $\mathcal{L}_f^x$ and $\mathcal{L}_f^y$, by Eq. (2.74), the associated ray transfer matrices are $\mathbf{L}_x(f)$ and $\mathbf{L}_y(f)$ respectively, i.e., ray transfer matrices of cylindrical lenses whose curvatures are in the x and y directions respectively (see (2.28)).

Here, the operators $\mathcal{F}_d$ and $\mathcal{L}_f$ are axially symmetric, the corresponding symplectic matrices $\mathbf{F}(d)$ and $\mathbf{L}(f)$ are in block form as in Eqs. (2.4) and (2.26), and act identically on $[\hat{x}, \hat{p}_x]^T$ and $[\hat{y}, \hat{p}_y]^T$. Further the blocks $F(d),\ L(f) \in Sp(2, \mathbb{R})$, i.e.,

$$F(d)\,\Omega\,F(d)^T = \Omega \ \text{ and}$$
$$L(f)\,\Omega\,L(f)^T = \Omega,$$

as seen from Eqs. (2.74) and (2.75). Suppose $\mathcal{U}(\mathbf{S})$ acts identically on $[\hat{x}, \hat{p}_x]^T$ and $[\hat{y}, \hat{p}_y]^T$, then

$$\mathcal{U}(\mathbf{S}) = \mathcal{U}_1(S) \otimes \mathcal{U}_2(S), \tag{2.83}$$
$$\text{and } \ \mathbf{S} = S \oplus S, \tag{2.84}$$

where $\mathcal{U}_1(S)$ ($\mathcal{U}_2(S)$) is the most general quadratic in $\hat{x}$ and $\hat{p}_x$ ($\hat{y}$ and $\hat{p}_y$) and $S \in Sp(2, \mathbb{R})$. With this, Eq. (2.74) can be explicitly written as

$$\mathcal{U}(S)\,\hat{x} = (s_{22}\,\hat{x} - s_{12}\,\hat{p}_x)\,\mathcal{U}(S), \tag{2.85}$$
$$\mathcal{U}(S)\,\hat{p}_x = (-s_{21}\,\hat{x} + s_{11}\,\hat{p}_x)\,\mathcal{U}(S). \tag{2.86}$$

Here, $\mathcal{U}(S) = \mathcal{U}_1(S)$ and s_{jk} is the (j,k)–th entry of S with j and k being 1 or 2. Suppose these operators act on an abstract state vector $|\psi_1\rangle$ with $\psi_1(x) = \langle x|\psi_1\rangle$ denoting the paraxial wave field in the position representation. In the position representation, we have

$$\langle x|\hat{x}|\psi_1\rangle = x\,\psi_1(x), \tag{2.87}$$
$$\text{and } \ \langle x|\hat{p}_x|\psi_1\rangle = -\frac{i}{\kappa}\,\frac{\partial\psi_1}{\partial x}, \tag{2.88}$$

where

$$\langle x_1|x\rangle = \delta(x - x_1), \tag{2.89}$$
$$\text{and } \int_{-\infty}^{\infty} dx\,|x\rangle\langle x| = \mathbb{I}, \tag{2.90}$$

with $\mathbb{I}$ being the identity operator in infinite dimensions. Note that Eqs. (2.89) and (2.90) are the orthogonality and completeness conditions respectively [115]. Then, in the position representation, Eqs. (2.85) and (2.86) readily become

$$\langle x_1|\mathcal{U}(S)\,\hat{x}|\psi_1\rangle = \langle x_1|(s_{22}\,\hat{x} - s_{12}\,\hat{p}_x)\,\mathcal{U}(S)|\psi_1\rangle, \tag{2.91}$$

$$\langle x_1|\mathcal{U}(S)\,\hat{p}_x|\psi_1\rangle = \langle x_1|(-s_{21}\,\hat{x} + s_{11}\,\hat{p}_x)\,\mathcal{U}(S)|\psi_1\rangle. \tag{2.92}$$

The LHS of Eq. (2.91) is now written as

$$\begin{aligned}\langle x_1|\mathcal{U}(S)\,\hat{x}|\psi_1\rangle &= \int_{-\infty}^{\infty} \mathrm{d}x\,\langle x_1|\mathcal{U}(S)\,\hat{x}\,|x\rangle\langle x|\psi_1\rangle, \\ &= \int_{-\infty}^{\infty} \mathrm{d}x\,\mathfrak{U}(x_1,x)\,x\,\psi_1(x),\end{aligned} \tag{2.93}$$

where we have defined

$$\mathfrak{U}(x_1,x) = \langle x_1|\mathcal{U}(S)|x\rangle. \tag{2.94}$$

Also, the LHS of Eq. (2.92) becomes

$$\begin{aligned}\langle x_1|\mathcal{U}(S)\,\hat{p}_x|\psi_1\rangle &= \int_{-\infty}^{\infty} \mathrm{d}x\,\langle x_1|\mathcal{U}(S)\,\hat{p}_x|x\rangle\langle x|\psi_1\rangle \\ &= \int_{-\infty}^{\infty} \mathrm{d}x\,\mathfrak{U}(x_1,x)\left(-\frac{i}{\kappa}\,\frac{\partial}{\partial x}\right)\psi_1(x) \\ &= \int_{-\infty}^{\infty} \mathrm{d}x\,\psi_1(x)\left(\frac{i}{\kappa}\,\frac{\partial}{\partial x}\right)\mathfrak{U}(x_1,x),\end{aligned} \tag{2.95}$$

where in the last step we have integrated by parts, and assumed that the wave field dies off

at the infinities. Now we consider the RHS of Eq. (2.91). We have

$$\langle x_1|(s_{22}\,\hat{x} - s_{12}\,\hat{p}_x)\,\mathcal{U}(S)|\psi_1\rangle = \int_{-\infty}^{\infty} \mathrm{d}x \int_{-\infty}^{\infty} \mathrm{d}x_2\, \langle x_1|(s_{22}\,\hat{x} - s_{12}\,\hat{p}_x)|x_2\rangle\langle x_2|\mathcal{U}(S)|x\rangle\langle x|\psi_1\rangle$$
$$= \int_{-\infty}^{\infty} \mathrm{d}x\, \psi_1(x) \left(s_{22}\,x_1 + s_{12}\,\frac{i}{\kappa}\,\frac{\partial}{\partial x_1}\right) \mathfrak{U}(x_1, x). \tag{2.96}$$

Similarly, the RHS of Eq. (2.92) is written as

$$\langle x_1|(-s_{21}\,\hat{x} + s_{11}\,\hat{p}_x)\,\mathcal{U}(S)|\psi_1\rangle = \int_{-\infty}^{\infty} \mathrm{d}x\, \psi_1(x) \left(-s_{21}\,x_1 - s_{11}\,\frac{i}{\kappa}\,\frac{\partial}{\partial x_1}\right) \mathfrak{U}(x_1, x). \tag{2.97}$$

By using Eqs. (2.93), (2.95), (2.96), and (2.97) in Eqs. (2.91) and (2.92) we obtain

$$\int_{-\infty}^{\infty} \mathrm{d}x\, \psi_1(x) \left(x - s_{22}\,x_1 - s_{12}\,\frac{i}{\kappa}\,\frac{\partial}{\partial x_1}\right) \mathfrak{U}(x_1, x) = 0, \tag{2.98}$$

$$\int_{-\infty}^{\infty} \mathrm{d}x\, \psi_1(x) \left(\frac{i}{\kappa}\,\frac{\partial}{\partial x} + s_{21}\,x_1 + s_{11}\,\frac{i}{\kappa}\,\frac{\partial}{\partial x_1}\right) \mathfrak{U}(x_1, x) = 0, \tag{2.99}$$

Because the LHS of Eqs. (2.98) and (2.99) should vanish for any arbitrary $\psi_1(x)$, we require

$$x\,\mathfrak{U}(x_1, x) = \left(s_{22}\,x_1 + s_{12}\,\frac{i}{\kappa}\,\frac{\partial}{\partial x_1}\right) \mathfrak{U}(x_1, x), \tag{2.100}$$

$$i\,\frac{\partial}{\partial x}\,\mathfrak{U}(x_1, x) = \left(-s_{21}\,x_1 - s_{11}\,\frac{i}{\kappa}\,\frac{\partial}{\partial x_1}\right) \mathfrak{U}(x_1, x). \tag{2.101}$$

It is easy to verify that

$$\mathfrak{U}(x_1, x) = \frac{\exp\left(-i\pi/4\right)}{\sqrt{\lambda s_{12}}}\, \exp\left[\frac{i\kappa}{2s_{12}}\,(s_{11}\,x^2 - 2\,x\,x_1 + s_{22}\,x_1^2)\right]. \tag{2.102}$$

Now we consider the transformed wave field $\mathcal{U}(S)\,|\psi_1\rangle$ in Eqs. (2.91) and (2.92), and let

$|\psi_2\rangle = \mathcal{U}(S)\,|\psi_1\rangle$. Then by Eq. (2.102),

$$\begin{aligned}\psi_2(x_1) = \langle x_1|\mathcal{U}(S)|\psi_1\rangle &= \int_{-\infty}^{\infty} \mathrm{d}x \int_{-\infty}^{\infty} \mathrm{d}x_2\, \langle x_1|x_2\rangle\langle x_2|\mathcal{U}(S)|x\rangle\langle x|\psi_1\rangle \\ &= \int_{-\infty}^{\infty} \mathrm{d}x\, \mathfrak{U}(x_1, x)\, \psi_1(x) \\ &= \frac{\exp\left(-i\pi/4\right)}{\sqrt{\lambda s_{12}}} \int_{-\infty}^{\infty} \mathrm{d}x\, \exp\left[\frac{i\kappa}{2s_{12}}\left(s_{11}\,x^2 - 2\,x\,x_1 + s_{22}\,x_1^2\right)\right] \psi_1(x). \end{aligned} \tag{2.103}$$

We now readily observe that when $S = F(d)$ (Eq. (2.3)), Eq. (2.103) reduces to the free propagation transformation in the x–z plane as described in Eq. (2.60).

Now we consider the case $s_{12} \to 0$. By using $s_{11}s_{22} - s_{12}s_{21} = 1$, we can rewrite Eq. (2.103) as

$$\begin{aligned}\psi_2(x_1) &= \frac{\exp\left(-i\pi/4\right)}{\sqrt{\lambda s_{12}}} \int_{-\infty}^{\infty} \mathrm{d}x\, \exp\left\{\frac{i\kappa}{2s_{12}}\left[s_{11}x^2 - 2\,x\,x_1 + \left(\frac{1 + s_{12}s_{21}}{s_{11}}\right) x_1^2\right]\right\} \psi_1(x) \\ &= \frac{\exp\left(-i\pi/4\right)}{\sqrt{\lambda s_{12}}}\, \exp\left(\frac{i\kappa s_{21}}{2s_{11}}\, x_1^2\right) \int_{-\infty}^{\infty} dx\, \psi_1(x)\, \exp\left[\frac{i\kappa s_{11}}{2s_{12}}\left(x - \frac{x_1}{s_{11}}\right)^2\right]. \end{aligned} \tag{2.104}$$

Note that when $s_{12} \to 0$, by applying the method of stationary phase [107, 43], we readily obtain

$$\begin{aligned}\psi_2(x_1) &= \frac{\exp\left(-i\pi/4\right)}{\sqrt{\lambda s_{12}}}\, \exp\left(\frac{i\kappa s_{21}}{2s_{11}}\, x_1^2\right)\psi\left(\frac{x_1}{s_{11}}\right) \times \exp\left(i\pi/4\right)\sqrt{\frac{2\pi s_{12}}{\kappa s_{11}}} \\ &= \frac{1}{\sqrt{s_{11}}}\, \exp\left(\frac{i\kappa s_{21}}{2s_{11}}\, x_1^2\right)\psi_1\left(\frac{x_1}{s_{11}}\right). \end{aligned} \tag{2.105}$$

Also we have $s_{11} \to 1/s_{22}$ as $s_{12} \to 0$ and Eq. (2.105) can readily be written as

$$\psi_2(x_1) = \sqrt{s_{22}}\, \exp\left(\frac{i\kappa s_{21}s_{22}}{2}\, x_1^2\right) \psi_1(s_{22}\, x_1). \tag{2.106}$$

Clearly, when $S = L(f)$ (Eq. (2.25)), Eq. (2.105) reads as $\psi_2(x_1) = \mathcal{L}_f(x)\, \psi_1(x_1)$, where $\mathcal{L}_f(x)$ is the action of thin lens on a wave field $\psi_1(x_1)$ traveling in the x–z plane (see Eq. (2.70)).

Thus, for any ray transfer matrix S of the axially symmetric system, the associated wave optic transformation is given by Eq. (2.103), and when $s_{12} \to 0$, the corresponding transformation is given by Eq. (2.105). In fact, as seen through Refs. [113, 116], the integral kernel given in Eqs. (2.102) and (2.105) for a given S can easily be generalized to a general $\mathbf{S} \in Sp(4, \mathbb{R})$ (Eq. (2.74)). Let

$$\mathbf{S} = \begin{bmatrix} s_{11} & s_{13} & s_{12} & s_{14} \\ s_{31} & s_{33} & s_{32} & s_{34} \\ s_{21} & s_{23} & s_{22} & s_{24} \\ s_{41} & s_{43} & s_{42} & s_{44} \end{bmatrix} \equiv \begin{bmatrix} \mathbf{s}_1 & \mathbf{s}_2 \\ \mathbf{s}_3 & \mathbf{s}_4 \end{bmatrix}. \tag{2.107}$$

Then, by Refs. [113, 116], the corresponding kernel is

$$\mathfrak{U}(\mathbf{x}_1, \mathbf{x}) = \frac{\exp(-i\pi/2)}{\sqrt{\lambda \det \mathbf{s}_2}} \exp\left[i\kappa \left(\frac{1}{2}\mathbf{x}_1^T \mathbf{s}_2^{-1}\mathbf{s}_4 \mathbf{x}_1 - \mathbf{x}_1^T \mathbf{s}_2^{-1}\mathbf{x} + \frac{1}{2}\mathbf{x}^T \mathbf{s}_1 \mathbf{s}_2^{-1}\mathbf{x}\right)\right], \tag{2.108}$$

and when $\det \mathbf{s}_2 \to 0$, the kernel is

$$\psi_2(\mathbf{x}_1) = \frac{1}{\sqrt{\det \mathbf{s}_1}} \exp\left(\frac{i\kappa}{2}\mathbf{x}_1^T \mathbf{s}_3 \mathbf{s}_1^{-1}\mathbf{x}_1\right)\psi_1\left(\mathbf{s}_1^{-1}\mathbf{x}_1\right). \tag{2.109}$$

2.6.1 Partially coherent wave fields

So far, we have restricted our attention to a coherent monochromatic paraxial wave field undergoing a unitary transformation generated by the most general quadratic in the operators $\hat{x}$, $\hat{p}_x$, $\hat{y}$, and $\hat{p}_y$. In fact, we can extend this approach to partially coherent scalar wave fields as well as to paraxial vectorial wave fields. For instance, a partially coherent light field is characterized by its cross-spectral density given by

$$\Gamma(\mathbf{x}_1, \mathbf{x}_2; z) = \sum_j \mathrm{p}_j \, \psi_j(\mathbf{x}_1; z) \, \psi_j^*(\mathbf{x}_2; z), \tag{2.110}$$

where $\psi_j(\mathbf{x}; z)$ are it's constituent coherent components with $\mathbf{x} = (x, y)$ and $\sum \mathrm{p}_j = 1$. Evidently by Eqs. (2.73) and (2.74), under the action of a FOOS corresponding to a $\mathbf{S}$ on the partially coherent wave field,

$$\Gamma \to \mathcal{U}(\mathbf{S}) \, \Gamma \, \mathcal{U}^\dagger(\mathbf{S}). \tag{2.111}$$

Further, one may evaluate Wolf function [117, 118] from the knowledge of cross-spectral density as

$$W(\xi) \equiv W(\mathbf{x}, \mathbf{p}) = \frac{\kappa^2}{(2\pi)^2} \int \mathrm{d}^2\mathbf{x}_1 \, \Gamma(\mathbf{x} - \mathbf{x}_1/2, \mathbf{x} + \mathbf{x}_1/2) \, \exp\left(i\kappa \, \mathbf{p} \cdot \mathbf{x}_1\right), \tag{2.112}$$

where $\mathbf{p} = (p_x, p_y)$ and $\xi = [x, p_x, y, p_y]^T$. Then as well known [112, 111],

$$\Gamma \to \mathcal{U}(\mathbf{S}) \, \Gamma \, \mathcal{U}^\dagger(\mathbf{S}) \Longleftrightarrow W(\xi) \to W(\mathbf{S}^{-1} \, \xi). \tag{2.113}$$

Thus, realizing any symplectic matrix $\mathbf{S}$ in terms of ray transfer matrices $\mathbf{F}(d)$ and $\mathbf{L}(f)$ is equivalent to realizing the corresponding unitary $\mathcal{U}(\mathbf{S})$ in terms of $\mathcal{F}_d$ and $\mathcal{L}_f$ on a paraxial wave field (both coherent as well as partially coherent). In a similar fashion, the realization of a unitary transformation as in Eq. (2.73) extends to paraxial vector wave fields through the appropriate replacement of the operators $\hat{\xi} = [\hat{x}, \hat{p}_x, \hat{y}, \hat{p}_y]^T$, as outlined in Refs. [119, 120, 121].

2.6.2 Definition of FOOS

Consider the Wolf function $W(\xi)$ (Eq. (2.112)) corresponding to an optical system. This optical system is said to be a FOOS if the Wolf function transforms linearly [94] as given in (2.113). FOOS can be broadly classified into two categories : *symmetric* and *asymmetric*. For symmetric FOOS, ray transfer matrix $\mathbf{S}^{-1}$ acts identically on $[x, p_x]^T$ and $[y, p_y]^T$, i.e., $\mathbf{S} = S \oplus S$ (Eq. (2.84)). An equivalent statement is that the ray coordinates x and y transform symmetrically (cf. (2.4) and (2.26)). Otherwise, the FOOS is said to be asymmetric. It is readily noted that from (2.28) that cylindrical lens is an example of asymmetric FOOS. We may note that examples of symmetric FOOS include, transmission through quadratic graded index media, fractional Fourier transform, magnifiers, inverse free propagation, and etc. [94, 95, 116, 122, 123, 96, 124].

2.7 Orbital angular momentum (OAM) of light

In this Section we obtain OAM possessed by a paraxial wave field traveling in z-direction from the Maxwell equations (Section 2.3). Since divergence of a curl vanishes, we can

associate a vector potential $\mathbf{A}$ [106, 107] for the magnetic field $\mathbf{B}$ obeying Eq. (2.30) as

$$\mathbf{B} = \nabla \times \mathbf{A}. \tag{2.114}$$

Substituting this in Eq. (2.31), we obtain

$$\begin{aligned} \nabla \times \mathbf{E} &= -\frac{\partial}{\partial t} (\nabla \times \mathbf{A}) \\ \nabla \times \left(\mathbf{E} + \frac{\partial \mathbf{A}}{\partial t} \right) &= 0. \end{aligned} \tag{2.115}$$

Because curl of a gradient is zero, we can associate a scalar function $\mathcal{V}$ [106, 107] with $\mathbf{E}$ as

$$\mathbf{E} + \frac{\partial \mathbf{A}}{\partial t} \equiv -\nabla \mathcal{V}. \tag{2.116}$$

Then the electric field $\mathbf{E}$ can be expressed as

$$\mathbf{E} = -\nabla \mathcal{V} - \frac{\partial \mathbf{A}}{\partial t}. \tag{2.117}$$

We can readily note that when the vector potential $\mathbf{A}$ does not vary with time, the scalar function $\mathcal{V}$ is just the well known electric potential in electrostatics [106]. Now by using Eqs. (2.114) and (2.117) in Eq. (2.32) we obtain

$$\begin{aligned} \nabla \times (\nabla \times \mathbf{A}) &= \mu_0 \, \epsilon_0 \, \frac{\partial}{\partial t} \left(-\nabla \mathcal{V} - \frac{\partial \mathbf{A}}{\partial t} \right) \\ \nabla^2 \mathbf{A} - \mu_0 \, \epsilon_0 \, \frac{\partial^2 \mathbf{A}}{\partial t^2} &= \nabla \left(\nabla \cdot \mathbf{A} + \mu_0 \, \epsilon_0 \, \frac{\partial \mathcal{V}}{\partial t} \right). \end{aligned} \tag{2.118}$$

Here, the second equality follows from the first by making use of the identity [106, 107]

$$\nabla \times (\nabla \times \mathbf{A}) = \nabla (\nabla \cdot \mathbf{A}) - \nabla^2 \mathbf{A}. \tag{2.119}$$

In *Lorentz gauge*, we choose

$$\nabla \cdot \mathbf{A} + \mu_0 \, \epsilon_0 \, \frac{\partial \mathcal{V}}{\partial t} = 0, \tag{2.120}$$

and hence Eq. (2.118) reduces to

$$\nabla^2 \mathbf{A} - \mu_0 \, \epsilon_0 \, \frac{\partial^2 \mathbf{A}}{\partial t^2} = 0. \tag{2.121}$$

In other words, $\mathbf{A}$ satisfies the wave equation (Eq. (2.35)). In the paraxial limit, $\mathbf{A}$ satisfies the paraxial wave equation (Eq. (2.45)). So, by Eqs. (2.41) and (2.42), the vector potential $\mathbf{A}$ [80, 125] given by

$$\mathbf{A} = \hat{i} \, \psi(x, y; z) \, \exp\left[i(\kappa z - \omega t)\right], \tag{2.122}$$

where $\hat{i}$ is the unit vector along the x–axis, and $\psi(x, y; z)$ is the associated paraxial wave field. Then, by Eq. (2.114), the associated magnetic field is

$$\begin{aligned}
\mathbf{B} &= \begin{vmatrix} \hat{i} & \hat{j} & \hat{k} \\ \frac{\partial}{\partial x} & \frac{\partial}{\partial y} & \frac{\partial}{\partial z} \\ \psi \, \exp\left[i(\kappa z - \omega t)\right] & 0 & 0 \end{vmatrix} \\
&= \left[\hat{j} \left(\frac{\partial \psi}{\partial z} + i\kappa \, \psi\right) - \hat{k} \, \frac{\partial \psi}{\partial y}\right] \exp\left[i(\kappa z - \omega t)\right] \\
&\approx i\kappa \left(\hat{j} \, \psi + \hat{k} \, \frac{i}{\kappa} \, \frac{\partial \psi}{\partial y}\right) \exp\left[i(\kappa z - \omega t)\right].
\end{aligned} \tag{2.123}$$

Here, $\hat{j}$ and $\hat{k}$ are unit vectors along y and z directions respectively. Note that since $\left|\frac{\partial \psi}{\partial z}\right| \ll |\kappa \, \psi|$, we have dropped the first term in the second equality. Now plugging this magnetic field in one of the Maxwell equations (Eq. (2.32)), we obtain

$$\begin{aligned}
\frac{1}{c^2} \, \frac{\partial \mathbf{E}}{\partial t} &= \begin{vmatrix} \hat{i} & \hat{j} & \hat{k} \\ \frac{\partial}{\partial x} & \frac{\partial}{\partial y} & \frac{\partial}{\partial z} \\ 0 & i\kappa \, \psi \, \exp\left[i(\kappa z - \omega t)\right] & -\frac{\partial \psi}{\partial y} \, \exp\left[i(\kappa z - \omega t)\right] \end{vmatrix} \\
&= \left\{-\hat{i} \left[\frac{\partial^2 \psi}{\partial y^2} + i\kappa \left(\frac{\partial \psi}{\partial z} + i\kappa \, \psi\right)\right] - \hat{j} \, \frac{\partial^2 \psi}{\partial x \partial y} + i\kappa \, \frac{\partial \psi}{\partial x}\right\} \exp\left[i(\kappa z - \omega t)\right] \\
&\approx \left[\hat{i} \, \kappa^2 \, \psi + \hat{k} \, (i\kappa) \, \frac{\partial \psi}{\partial x}\right] \exp\left[i(\kappa z - \omega t)\right].
\end{aligned} \tag{2.124}$$

Here, we note that we have neglected first two terms of the $\hat{i}$ component, and the $\hat{j}$ component. Now since $c = \omega/\kappa$, we readily observe that

$$\mathbf{E} \approx i\omega \left(\hat{i}\, \psi + \hat{k}\, \frac{i}{\kappa}\, \frac{\partial \psi}{\partial x} \right) \exp\left[i(\kappa z - \omega t) \right]. \tag{2.125}$$

It can be noted this choice of electric field is also consistent with the other Maxwell equation (2.31). With this, the linear momentum density associated with ψ is [80]

$$\begin{aligned} \mathsf{P} &= \epsilon_0 \left(\mathbf{E} \times \mathbf{B} \right) \\ &= \frac{\epsilon_0}{2} \left(\mathbf{E}^* \times \mathbf{B} + \mathbf{E} \times \mathbf{B}^* \right) \\ &= \frac{i\, \omega\, \epsilon_0}{2} \left(\psi\, \nabla_\perp \psi^* - \psi^*\, \nabla_\perp \psi \right) + \hat{k}\, \omega\, \kappa\, \epsilon_0\, |\psi|^2, \end{aligned} \tag{2.126}$$

where $\nabla_\perp = \hat{i}\, \frac{\partial}{\partial x} + \hat{j}\, \frac{\partial}{\partial y}$. Now, integrating Eq. (2.126) over the transverse coordinates x and y, we readily obtain

$$\begin{aligned} \bar{\mathsf{P}} &\equiv \int_{-\infty}^{\infty} \int_{-\infty}^{\infty} \mathrm{d}x\, \mathrm{d}y\, \mathsf{P} \\ &= \omega\, \kappa\, \epsilon_0 \left(\hat{i}\, \langle \hat{p}_x \rangle + \hat{j}\, \langle \hat{p}_y \rangle + \hat{k} \right). \end{aligned} \tag{2.127}$$

Here, $\hat{p}_x = -\frac{i}{\kappa}\, \frac{\partial}{\partial x}$, and $\hat{p}_y = -\frac{i}{\kappa}\, \frac{\partial}{\partial y}$ in the position representation. Also, $\langle \hat{\xi} \rangle$ is the expectation value of $\hat{\xi}$, where $\hat{\xi}$ is some arbitrary operator, and is defined as

$$\langle \hat{\xi} \rangle = \int_{-\infty}^{\infty} \int_{-\infty}^{\infty} \psi^*(x, y; z)\, \hat{\xi}\, \psi(x, y; z)\, \mathrm{d}x\, \mathrm{d}y. \tag{2.128}$$

Noting that the orbital angular momentum density L associated with ψ is [126]

$$\mathsf{L} = \mathbf{r} \times \mathsf{P}, \tag{2.129}$$

where $\mathbf{r} = x\, \hat{i} + y\, \hat{j} + z\, \hat{k}$, and defining

$$\bar{\mathsf{L}} \equiv \int_{-\infty}^{\infty} \int_{-\infty}^{\infty} \mathrm{d}x\, \mathrm{d}y\, \mathsf{L}, \tag{2.130}$$

the z component of $\bar{\mathsf{L}}$ is

$$\bar{\mathsf{L}}_z = \omega\,\kappa\,\epsilon_0\,(\langle\hat{x}\,\hat{p}_y\rangle - \langle\hat{y}\,\hat{p}_x\rangle), \tag{2.131}$$

with $\hat{x} = x$, and $\hat{y} = y$ in the position representation. Likewise, we can also define the *extrinsic angular momentum* as

$$\bar{\mathsf{L}}^{\rm ext} = \langle\mathbf{r}\rangle \times \bar{\mathsf{P}}, \tag{2.132}$$

where

$$\langle\mathbf{r}\rangle = \int_{-\infty}^{\infty}\int_{-\infty}^{\infty} \mathrm{d}x\,\mathrm{d}y\,\psi^*\,\mathbf{r}\,\psi. \tag{2.133}$$

Clearly, the z component of $\bar{\mathsf{L}}^{\rm ext}$ is

$$\bar{\mathsf{L}}_z^{\rm ext} = \omega\,\kappa\,\epsilon_0\,(\langle\hat{x}\rangle\langle\hat{p}_y\rangle - \langle\hat{y}\rangle\langle\hat{p}_x\rangle). \tag{2.134}$$

Now, the *intrinsic angular momentum* associated with ψ can readily be defined as

$$\bar{\mathsf{L}}^{\rm int} = \bar{\mathsf{L}} - \bar{\mathsf{L}}^{\rm ext}, \tag{2.135}$$

whereas the corresponding z component is

$$\bar{\mathsf{L}}_z^{\rm int} = \bar{\mathsf{L}}_z - \bar{\mathsf{L}}_z^{\rm ext} \equiv \omega\,\epsilon_0\,\tau. \tag{2.136}$$

Here, τ is the *twist parameter* [127] and is given as

$$\tau = \kappa\,\langle(\Delta\hat{x}\,\Delta\hat{p}_y - \Delta\hat{y}\,\Delta\hat{p}_x)\rangle, \tag{2.137}$$

where $\Delta\hat{\xi} = \hat{\xi} - \langle\hat{\xi}\rangle$. Further, by Refs. [128, 129], we readily observe that for cylindrical coordinates, τ assumes the form

$$\tau = \left\langle -i\,\frac{\partial}{\partial\theta}\right\rangle. \tag{2.138}$$

For instance, the LG mode $\psi_p^l(r,\theta;z)$ (see Eq. (2.51)) possesses a twist of l. Thus, paraxial wave fields possessing dislocations in their phase carry a non-zero twist.

2.8 Concluding remarks

In summary, we have derived ray transfer matrices for optical transformations such as free propagation and thin lens in the paraxial limit. Next, we have obtained such transformations using wave optics in the paraxial limit. We then have showed the equivalence between ray and wave optic versions for the optical transformation corresponding to a general FOOS in the paraxial limit. Finally, we have obtained longitudinal OAM carried by paraxial wave fields from the Maxwell equations.

Chapter 3

Some standard phase estimation tools and techniques

3.1 Introduction

In Chapter 1 we outlined phase estimation methods through intensity measurements in general. In this Chapter we explain such standard methods classified in Figure 1.1 and related mathematical tools and techniques. For the interferometry based methods, we discuss phase shifting interferometry and Fourier fringe analysis, and for the diffraction based methods, we discuss some of the well known techniques in gradient based and iteration based methods.

3.2 Phase shifting interferometry

In interferometry, we typically split a coherent wave field into two beams using a beam-splitter, pass them through reference and test arms, recombine them using another (or the same) beam-splitter, and record the intensity pattern by a CCD camera. In phase shifting interferometry, we record a series of interferograms with different phase shifts by providing an extra phase shift at the reference arm. This extra phase shift could, for instance, be applied using geometric phase or dynamic phase. While in the former case, the wave field passing through the reference arm acquires an extra phase shift due to the geometric phase introduced by the combination of quarter wave and half wave plates [20, 21], the path length of the reference arm is increased [4, 5] in the latter case, for instance, by means of piezoelectric transducers (PZT).

To illustrate, we consider Twyman-Green interferometer setup as shown in Figure 3.1, where the phase shift is achieved by moving the reference surface by means of a PZT. Sup-

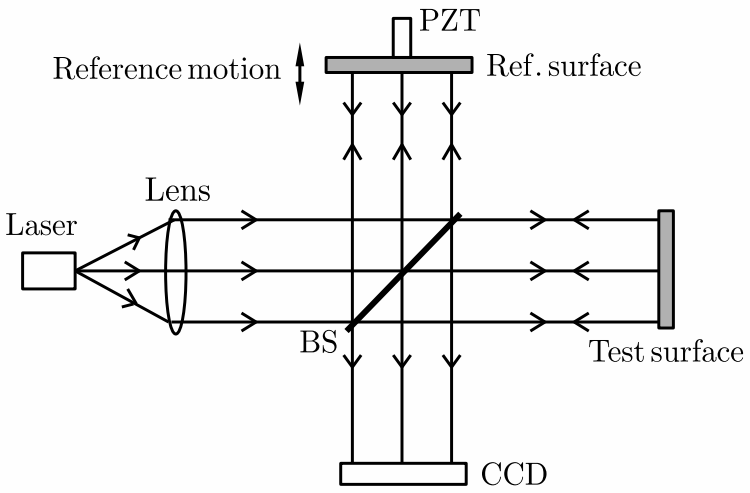

Figure 3.1: Phase shifting interferometry using Twyman-Green interferometer. Coherent light from laser is collimated by the lens before being split into two beams by the beam-splitter (BS). These two beams then recombine at the BS after getting reflected by test and reference surfaces, and the interference pattern is captured by the CCD camera. Here, motion of the reference surface can be controlled by piezo-electric transducer (PZT).

pose we are able to record N interferograms, namely $I_1(x, y)$ through $I_N(x, y)$, represented as

$$I_j(x, y) = I_0(x, y) \left\{ 1 + \cos \left[\phi(x, y) - \frac{2\pi}{N} j \right] \right\}. \tag{3.1}$$

Here, $I_0(x, y)$ is the background intensity, and $\phi(x, y)$ is the phase information we wish to retrieve. Now we discuss how the phase information encoded in these series interferograms can be extracted. The following analysis is based on Ref. [25]. First, we define the penalty function $\mathcal{Q}$ as

$$\mathcal{Q} \equiv \sum_{j=1}^{N} \left\{ I_j - I_0 - I_0 \cos \left(\phi - \frac{2\pi}{N} j \right) \right\}^2. \tag{3.2}$$

The best estimate of the phase function $\phi(x, y)$ is obtained when the partial derivative of $\mathcal{Q}$

with respect to ϕ vanishes, i.e., $\frac{\partial \mathcal{Q}}{\partial \phi} = 0$ or

$$\sum_{j=1}^{N} \left\{ I_j - I_0 - I_0 \cos\left(\phi - \frac{2\pi}{N} j\right) \right\} \sin\left(\phi - \frac{2\pi}{N} j\right) = 0. \tag{3.3}$$

It is readily noted that

$$\sum_{j=1}^{N} \sin\left(\frac{2\pi}{N} j\right) = \sum_{j=1}^{N} \mathrm{Im}\left\{\varpi^j\right\} = \sum_{j=1}^{N} \mathrm{Im}\left\{\frac{\varpi\left(\varpi^N - 1\right)}{\varpi - 1}\right\} = 0, \tag{3.4}$$

$$\sum_{j=1}^{N} \cos\left(\frac{2\pi}{N} j\right) = \sum_{j=1}^{N} \mathrm{Re}\left\{\varpi^j\right\} = \sum_{j=1}^{N} \mathrm{Re}\left\{\frac{\varpi\left(\varpi^N - 1\right)}{\varpi - 1}\right\} = 0, \tag{3.5}$$

where $\varpi = \exp\left(\frac{2\pi i}{N}\right)$, the N–th root of unity. Also,

$$\begin{aligned} \sum_{j=1}^{N} \cos\left(\phi - \frac{2\pi}{N} j\right) \sin\left(\phi - \frac{2\pi}{N} j\right) &= \frac{1}{2} \sum_{j=1}^{N} \mathrm{Im}\left\{\exp\left(2i\phi - \frac{4\pi i}{N} j\right)\right\} \\ &= 0. \end{aligned} \tag{3.6}$$

Using these results, we obtain

$$\begin{aligned} \sum_{j=1}^{N} I_j \sin\left(\phi - \frac{2\pi}{N} j\right) &= 0 \\ \sin\phi \sum_{j=1}^{N} I_j \cos\left(\frac{2\pi}{N} j\right) &= \cos\phi \sum_{j=1}^{N} I_j \sin\left(\frac{2\pi}{N} j\right) \\ \phi(x, y) &= \tan^{-1}\left[\frac{\sum_{j=1}^{N} I_j \sin\left(\frac{2\pi}{N} j\right)}{\sum_{j=1}^{N} I_j \cos\left(\frac{2\pi}{N} j\right)}\right]. \end{aligned} \tag{3.7}$$

Clearly, the retrieved phase is in wrapped form and is unwrapped as demonstrated in Section 3.5.

Before proceeding to Fourier fringe analysis [15, 16], we need to understand Hilbert transforms and the notion of asymptotic analytic signals.

3.3 Hilbert transform

Consider a real, square integrable function $U(x)$ with $-\infty < x < \infty$ and

$$\int_{-\infty}^{\infty} U^2(x)\,\mathrm{d}x < \infty. \tag{3.8}$$

Now its Hilbert transform [130] is defined as

$$U_h(x) \equiv -\frac{1}{\pi}\,\mathrm{P}\int_{-\infty}^{\infty} \frac{U(\tilde{t})}{\tilde{t}-x}\,\mathrm{d}\tilde{t}. \tag{3.9}$$

Here, P refers to the Cauchy principal value at $\tilde{t} = x$. The Hilbert transform of $U_h(x)$ is given by

$$U(x) = -\frac{1}{\pi}\,\mathrm{P}\int_{-\infty}^{\infty} \frac{U_h(\tilde{t})}{\tilde{t}-x}\,\mathrm{d}\tilde{t}. \tag{3.10}$$

It can be noted that the functions $U(x)$ and $U_h(x)$ form a *Hilbert transform pair* [130]. Further, the *complex analytic signal* [130] corresponding to the function $U(x)$ is defined as

$$U_a(x) \equiv U(x) + i\,U_h(x). \tag{3.11}$$

Let $\tilde{U}(\tilde{x})$, $\tilde{U}_h(\tilde{x})$, and $\tilde{U}_a(\tilde{x})$ denote the Fourier transform of $U(x)$, $U_h(x)$, and $U_a(x)$ respectively, i.e.,

$$\tilde{U}(\tilde{x}) = \frac{1}{\sqrt{2\pi}}\int_{-\infty}^{\infty} U(x)\,e^{ix\tilde{x}}\,\mathrm{d}x, \tag{3.12}$$

$$U(x) = \frac{1}{\sqrt{2\pi}}\int_{-\infty}^{\infty} \tilde{U}(\tilde{x})\,e^{-ix\tilde{x}}\,\mathrm{d}\tilde{x}. \tag{3.13}$$

Similarly, the Fourier pairs of $U_h(x)$ and $U_a(x)$ can also readily be defined, and we have avoided for brevity. Then, by Ref. [41], we note that

$$\tilde{U}_h(x) = -i\,\mathrm{sig}(x)\,\tilde{U}(x), \tag{3.14}$$

where $\mathrm{sig}(x)$ denotes the signum function of a real variable x and is defined as

$$\mathrm{sgn}(x) = \begin{cases} -1 & \text{if } x < 0, \\ 0 & \text{if } x = 0, \\ 1 & \text{if } x > 0. \end{cases} \tag{3.15}$$

By Eqs. (3.11) and (3.14), we readily observe that

$$\tilde{U}_a(\tilde{x}) = 2\,\Theta(\tilde{x})\,\tilde{U}(\tilde{x}). \tag{3.16}$$

Here, $\Theta(x)$ is the Heaviside step function and is given as

$$\Theta(x) = \begin{cases} 1 & \text{if } x \geq 0, \\ 0 & \text{if } x < 0. \end{cases} \tag{3.17}$$

3.3.1 Asymptotic analytic signal

Let

$$U(x) = A(x)\,\cos\left[\Lambda\,\phi(x)\right], \tag{3.18}$$

where $A(x)$ and $\phi(x)$ are the amplitude and phase respectively of the function $U(x)$, and Λ is a large positive real number. Assuming that $A(x)$ and $\phi(x)$ are twice and four times continuously differentiable functions respectively [41, 40], the asymptotic analytic signal $U_a(x)$ corresponding to the function $U(x)$ is given by

$$U_a(x) = A(x)\,\exp\left[i\,\Lambda\,\phi(x)\right] + O(\Lambda^{-3/2}),\ \ \Lambda \to \infty. \tag{3.19}$$

3.4 Fourier fringe analysis

Now we explain the phase retrieval from perturbed straight line fringes. First, we consider the seminal work of Takeda *et al.* [15]. Suppose we are given a perturbed straight line fringe represented as

$$I(x, y) = I_0(x, y) + I_0(x, y)\,\cos\left[\phi(x, y) + \kappa_1\,x + \kappa_2\,y\right]. \tag{3.20}$$

Here, $I_0(x, y)$ is the background intensity, $\kappa_1\, x + \kappa_2\, y$ is the effective tilt, and $\phi(x, y)$ is the phase information we wish to retrieve. It is assumed that the functions $I_0(x, y)$ and $\phi(x, y)$ vary much slowly in compared with the tilt term. On Fourier transforming Eq. (3.20), we readily obtain

$$\tilde{I}(\kappa_x, \kappa_y) = \tilde{I}_0(\kappa_x, \kappa_y) + \tilde{\vartheta}(\kappa_x - \kappa_1, \kappa_y - \kappa_2) + \tilde{\vartheta}^*(\kappa_x + \kappa_1, \kappa_y + \kappa_2), \tag{3.21}$$

where $\tilde{\vartheta}(\kappa_x, \kappa_y)$ is the Fourier transform of the function

$$\vartheta(x, y) = \frac{1}{2}\, I_0(x, y)\, \exp\left[i\phi(x, y)\right]. \tag{3.22}$$

In the frequency plane, we observe that there exist three peaks corresponding to the terms $\tilde{I}_0(\kappa_x, \kappa_y)$, $\tilde{\vartheta}(\kappa_x, \kappa_y)$, and $\tilde{\vartheta}^*(\kappa_x, \kappa_y)$ centered at $(0, 0)$, (κ_1, κ_2), and $(-\kappa_1, -\kappa_2)$ respectively. First, we remove the peak due to the term $\tilde{I}_0(\kappa_x, \kappa_y)$. As $\tilde{\vartheta}^*(\kappa_x, \kappa_y)$ is the complex conjugate of $\tilde{\vartheta}(\kappa_x, \kappa_y)$, it doesn't contain any extra information. So, we move the peak corresponding to $\tilde{\vartheta}(\kappa_x, \kappa_y)$ to the center, i.e., $(0, 0)$, and inverse Fourier transform to get back $\vartheta(x, y)$. Performing complex logarithm to this function gives

$$\log\left[\vartheta(x, y)\right] = \log\left[\frac{1}{2}\, I_0(x, y)\right] + i\phi(x, y). \tag{3.23}$$

Thus, the imaginary part of the complex logarithm contains the desired phase information in wrapped form and is unwrapped as demonstrated in Section 3.5.

An alternate method suggested by Ikeda *et al.* [16] is as follows. After Fourier transforming $I(x, y)$ as in Eq. (3.21), we first remove the term $\tilde{I}_0(\kappa_x, \kappa_y)$ at the center of the frequency plane. Then we inverse Fourier transform to obtain

$$I_c(x, y) \equiv I_0(x, y)\, \cos\left[\phi(x, y) + \kappa_1\, x + \kappa_2\, y\right]. \tag{3.24}$$

Since $I_0(x, y)$ is assumed to vary slowly in compared with the tilt term, the Hilbert transform (Eq. (3.9)) of $I_c(x, y)$ yields

$$I_s(x, y) \equiv I_0(x, y)\, \sin\left[\phi(x, y) + \kappa_1\, x + \kappa_2\, y\right]. \tag{3.25}$$

By Eqs. (3.24) and (3.25), the phase along with the tilt term is computed as

$$\phi(x, y) + \kappa_1\, x + \kappa_2\, y = \tan^{-1}\left[\frac{I_s(x, y)}{I_c(x, y)}\right]. \tag{3.26}$$

Again, the phase extracted is in wrapped form along with the effective tilt. So, the phase retrieved (discarding the effective tilt) through both phase shifting method (Section 3.2) as well as Fourier fringe analysis is in wrapped form.

3.5 Phase unwrapping

As remarked earlier in Sections 3.2 and 3.4, the retrieved phase is, in general, wrapped. We now outline a procedure that demonstrates how such phases are unwrapped. For brevity, we consider one dimensional version of Eq. (3.26) given by

$$\phi(x) = \tan^{-1}\left[\frac{I_s(x)}{I_c(x)}\right]. \tag{3.27}$$

Note that we have discarded the tilt term. Because the $\tan^{-1}$ function returns values between $\pm\pi$, the phase function $\phi(x)$ is in wrapped form as shown in frame (a) of the Figure 3.2. In order to obtain the unwrapped phase structure, we need to add or subtract 2π whenever we encounter a discontinuity.

Let $\{\phi_w(1), \phi_w(2), \ldots, \phi_w(N)\}$ and $\{\phi(1), \phi(2), \ldots, \phi(N)\}$ be the discretized versions of the wrapped phase $\phi_w(x)$ and unwrapped phase $\phi(x)$ respectively. Suppose

$$\phi_w(k+1) - \phi_w(k) = 2\pi. \tag{3.28}$$

Then the corresponding unwrapped phase is

$$\phi(k) = \phi_w(k), \tag{3.29}$$

$$\phi(k+1) = \phi_w(k+1) - 2\pi. \tag{3.30}$$

In practice [15], the phase is unwrapped if the inequality

$$\phi_w(k+1) - \phi_w(k) \geq 0.9 \times 2\pi. \tag{3.31}$$

is satisfied instead of Eq. (3.28). Similarly, if

$$\phi_w(k+1) - \phi_w(k) \leq -0.9 \times 2\pi, \tag{3.32}$$

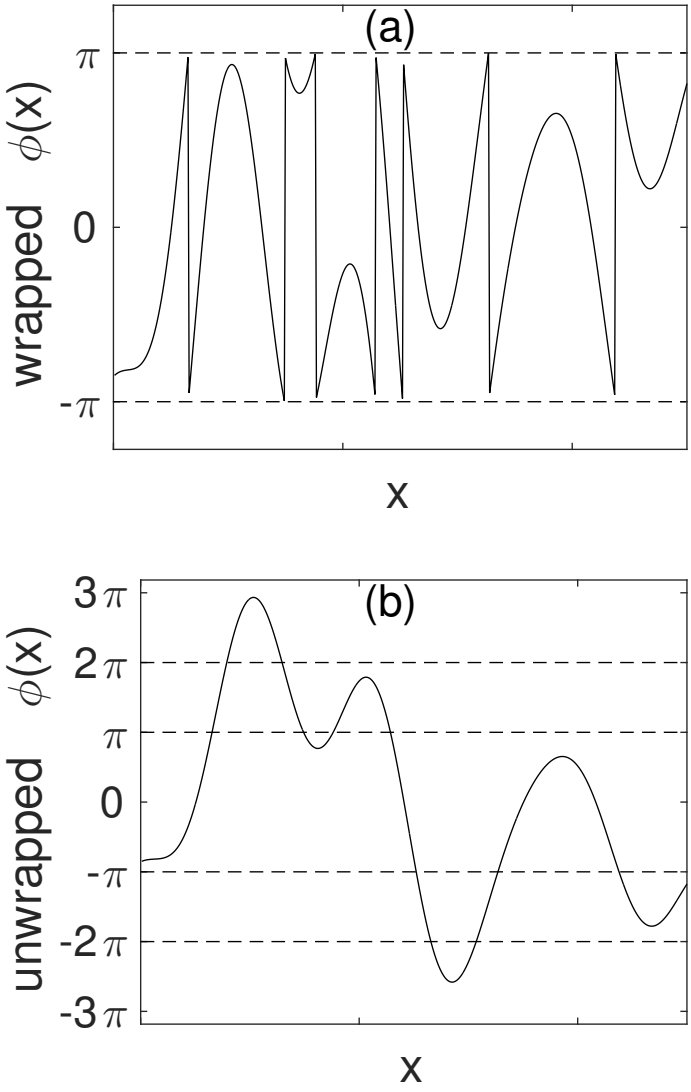

Figure 3.2: Frame (a) shows an example of the wrapped phase function $\phi(x)$, i.e., $\phi(x)$ assuming values between $-\pi$ and π. Frame (b) is the corresponding unwrapped version of $\phi(x)$ and is obtained by adding or subtracting 2π wherever discontinuity occurs.

then we readily see that

$$\phi(k) = \phi_w(k), \tag{3.33}$$

$$\phi(k+1) = \phi_w(k+1) + 2\pi. \tag{3.34}$$

Applying this procedure, we can obtain the unwrapped phase information from the wrapped one (see frame (b) of Figure 3.2).

Having discussed some widely used techniques in interferometry based methods, we now turn our attention towards diffraction based methods in the Sections below.

3.6 Shack-Hartmann wavefront sensor

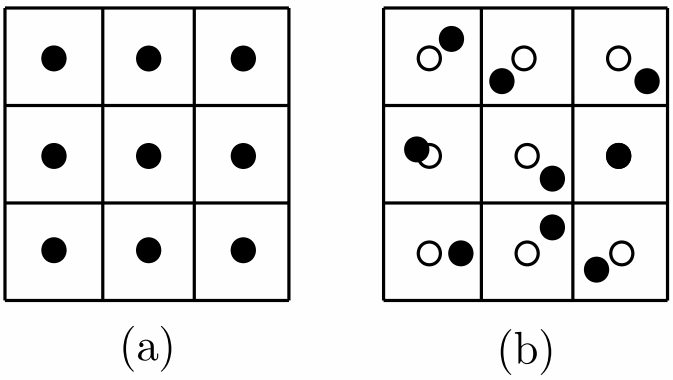

Figure 3.3: In frame (a), '•' represents the focal spot position formed by the plane wave field (PW) on the CCD screen. In frame (b), '∘' represents the focal spot position formed by the PW, while '•' represents the focal spot position formed by an incoming wave field (IW) on the CCD screen.

In this Section we explain phase retrieval of an incoming wavefront through the use of its gradients using Shack-Hartmann wavefront sensor. Suppose a wave field $A(x, y; z)$ $\times \exp\left[i\phi(x, y; z)\right]$ is traveling in the z–axis, and whose phase gradients are defined as $\phi_x \equiv \frac{\partial \phi}{\partial x}$ and $\phi_y \equiv \frac{\partial \phi}{\partial y}$. The Shack-Hartmann wavefront sensor is a device that measures phase gradients of the incoming wave field (IW). It consists of a lenslet array in which a system of

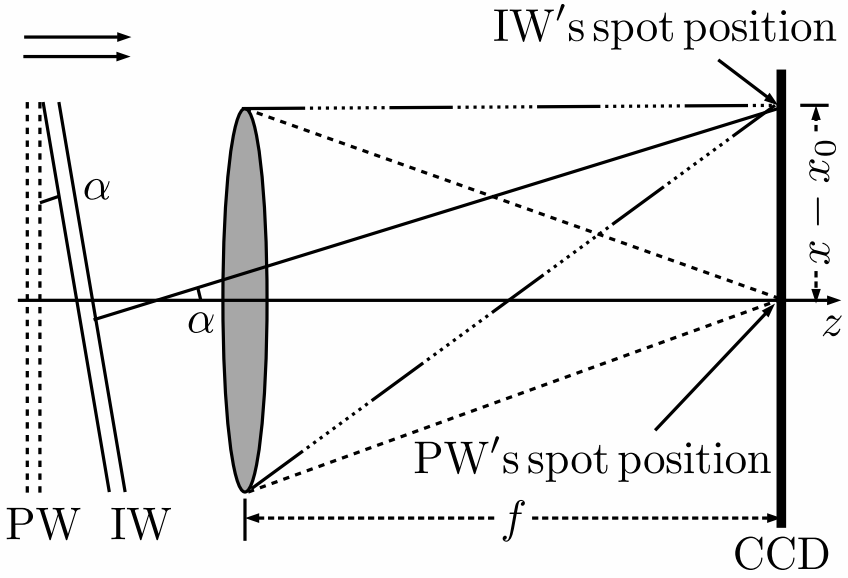

Figure 3.4: Shown here is a lens of focal length f in the lenslet array. The PW is focused at the center x_0 where the z–axis passes through the CCD screen, while the IW is focused at the point x on the CCD screen. Clearly, the tilt of the IW is proportional to $x - x_0$.

$N_1 \times N_2$ lenses with same focal length are placed in a rectangular lattice. The spots formed by these lenses due to the IW fall on the screen of the CCD camera with $N_3 \times N_4$ pixels. Suppose a plane wave field (PW) passes through the lenslet array and makes spots on the CCD screen as shown in frame (a) of Figure 3.3. For instance, as illustrated in Figure 3.4, the PW is focused at the center x_0 where the z–axis passes through the CCD screen, and the arbitrary IW is focused at the point x on the CCD screen. It is easy to see that the tilt of the IW is proportional to the distance $x - x_0$. As seen through Ref. [131], α, angle between PW and IW, is given by

$$\alpha = \frac{x - x_0}{f} = \frac{1}{\kappa}\,\phi_x. \tag{3.35}$$

Now, having determined the phase gradients ϕ_x and ϕ_y, we can reconstruct the phase information $\phi(x, y)$ using the least square method outlined in Section 6.3. Two remarks are in order. First, the phase gradients are obtained by diffracting the wave field through the lenslet array. Second, this method reconstructs the phase directly from its gradients without phase unwrapping (see Section 3.5).

3.7 Gerchberg-Saxton (GS) algorithm

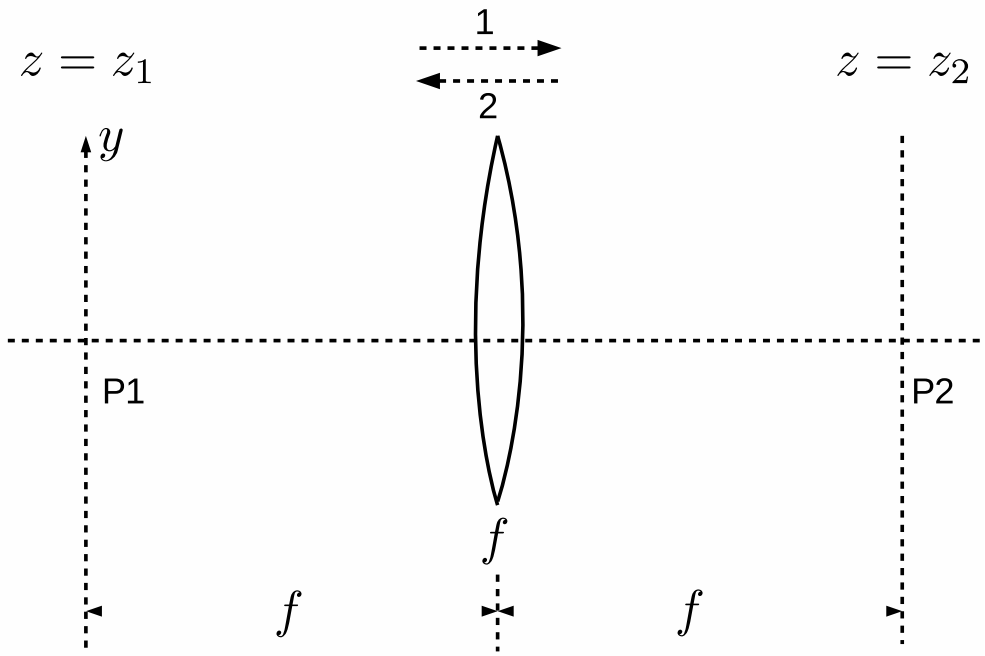

Figure 3.5: Schematic of Gerchberg-Saxton (GS) algorithm. The wave field at plane P1 is Fourier transformed (free propagation by a distance f, followed by a thin lens of focal length f, and followed by another free propagation by a distance f) and reaches the plane P2. At P2, the amplitude of the wave field is replaced with $A(x, y; z_2)$, and the resulting wave field is now inverse Fourier transformed and reaches P1. Here, again we replace the amplitude with $A(x, y; z_1)$. Repeating this process N times retrieves the respective phases at planes P1 and P2.

In this Section we overview some well known iterative algorithms to retrieve phases from two or more transverse plane intensity measurements. We first explain GS algorithm [58], an iterative process to obtain the phase information from the knowledge of intensity information recorded at two transverse planes. Suppose a wave field is traveling in the z–axis. Let P1 and P2 be two transverse planes separated by a distance $2f$ as shown in Figure 3.5, and the wave fields at P1 and P2 can be represented by $\psi(x, y; z_1) = A(x, y; z_1)$ $\times \exp[i\phi(x, y; z_1)]$ and $\psi(x, y; z_2) = A(x, y; z_2)\ \exp[i\phi(x, y; z_2)]$ respectively. Here, $A(\cdot)$ and $\phi(\cdot)$ denote amplitude and phase functions at the respective transverse planes. Also, the wave field $\psi(x, y; z_2)$ is the Fourier transform of $\psi(x, y; z_1)$. The Fourier transformation between the planes P1 and P2 is achieved by free propagating the wave field by a distance f, followed by a thin convex lens of focal length f, and followed by another free

propagation by a distance f [108, 132, 95]. Suppose we have the intensity information $I(x, y; z_1) = A^2(x, y; z_1)$ and $I(x, y; z_2) = A^2(x, y; z_2)$ measured at the planes P1 and P2 respectively, and we wish to retrieve the phases $\phi(x, y; z_1)$ and $\phi(x, y; z_2)$. To do so, we first begin with $A(x, y; z_1) \exp[i\phi_1(x, y; z_1)]$, where $\phi_1(x, y; z_1)$ is the trial phase assumed at P1. Numerical Fourier transformation of this wave field then yields $\psi_1(x, y; z_2) = A_1(x, y; z_2) \exp[i\phi_1(x, y; z_2)]$. Now we replace $A_1(x, y; z_2)$ with $A(x, y; z_2)$ and numerically inverse Fourier transform the resultant wave field to obtain $\psi_2(x, y; z_1) = A_2(x, y; z_1)$ $\times \exp[i\phi_2(x, y; z_1)]$. The amplitude $A_2(x, y; z_1)$ is again replaced with $A(x, y; z_1)$, and the process is iterated for N times. After N such iterations, the wave field obtained after N iterations, i.e., $\psi_{2N}(x, y; z_1)$, is nearly identical to the actual wave field $\psi(x, y; z_1)$. In other words, the respective phases at planes P1 and P2 are obtained after N iterations.

Several modifications to the GS algorithm have been proposed in the literature [59, 133, 61]. In Ref. [59], it was demonstrated that the introduction of new set of object constraints sped up the convergence of the algorithm. The uniqueness of the phase retrieved through the GS algorithm was discussed in Ref. [134]. These iterative algorithms, as discussed by Fienup and Wackerman [133], could stagnate, and they studied some standard stagnation problems and proposed ways to overcome them. Fienup [61] also proved that the convergence of the iterative algorithm in which the wave fields at P1 and P2 were related by free propagation transformation instead of Fourier transformation. In fact, in Refs. [135, 62], it was demonstrated that the phase information of the wave fields at P1 and P2 could be retrieved if the respective wave fields were related by any unitary transformation pertaining to a symmetric FOOS, or even by a non-unitary transformation. In Refs. [63, 64], a sequence of intensities were recorded at N transverse planes, and the GS algorithm was used to retrieve the phase information. It was argued that the phase retrieval was unambiguous owing to the constraints imposed by the intensity information at more transverse planes.

3.8 Transport-of-intensity equation

Transport-of-intensity method is another well known diffraction based method to retrieve phase from intensities. Suppose a paraxial wave field $\psi(\mathbf{x}; z)$ with $\mathbf{x} = (x, y)$ is traveling in the z–axis. Say we measure intensities at nearby transverse planes located at z and $z + \delta z$ with $\delta z \to 0$. Then the phase information can be extracted as follows. Let us consider a paraxial wave field

$$\psi(\mathbf{x}) = A(\mathbf{x}) \exp[i\,\phi(\mathbf{x})] \tag{3.36}$$

respecting the paraxial wave equation (Eq. (2.45)), where $A(\cdot)$ and $\phi(\cdot)$ refer to the amplitude and phase respectively of the wave field $\psi(\mathbf{x})$. After a little straightforward algebra, we have

$$\frac{\partial \psi}{\partial x} = \exp(i\phi)\left(\frac{\partial A}{\partial x} + i\,A\,\frac{\partial \phi}{\partial x}\right), \text{ and} \tag{3.37}$$

$$\frac{\partial^2 \psi}{\partial x^2} = \exp(i\phi)\left[\frac{\partial^2 A}{\partial x^2} + 2\,i\,\frac{\partial A}{\partial x}\,\frac{\partial \phi}{\partial x} - A\left(\frac{\partial \phi}{\partial x}\right)^2 + i\,A\,\frac{\partial^2 \phi}{\partial x^2}\right]. \tag{3.38}$$

Similarly, it can readily be obtained that

$$\frac{\partial^2 \psi}{\partial y^2} = \exp(i\phi)\left[\frac{\partial^2 A}{\partial y^2} + 2\,i\,\frac{\partial A}{\partial y}\,\frac{\partial \phi}{\partial y} - A\left(\frac{\partial \phi}{\partial y}\right)^2 + i\,A\,\frac{\partial^2 \phi}{\partial y^2}\right], \text{ and} \tag{3.39}$$

$$\frac{\partial \psi}{\partial z} = \exp(i\phi)\left(\frac{\partial A}{\partial z} + i\,A\,\frac{\partial \phi}{\partial z}\right). \tag{3.40}$$

Substituting Eqs. (3.38), (3.39), and (3.40) in Eq. (2.45), and equating real and imaginary parts, we respectively obtain

$$2\,\kappa\,\frac{\partial \phi}{\partial z} = |\nabla_\perp \phi|^2 - \frac{1}{A}\,\nabla_\perp^2 A, \text{ and} \tag{3.41}$$

$$2\,\kappa\,\frac{\partial A}{\partial z} = 2\,\nabla_\perp A \cdot \nabla_\perp \phi + A\,\nabla_\perp^2 \phi. \tag{3.42}$$

Here, $\nabla_\perp = \hat{i}\,\frac{\partial}{\partial x} + \hat{j}\,\frac{\partial}{\partial y}$. Since the intensity is $I(\mathbf{x}) = A^2(\mathbf{x})$, Eqs. (3.41) and (3.42) respectively become

$$2\,\kappa\,\frac{\partial \phi}{\partial z} = |\nabla_\perp \phi|^2 - I^{-1/2}\,\nabla_\perp^2 (I^{1/2}), \tag{3.43}$$

and

$$\begin{aligned} 2\,\kappa\,\frac{\partial I^{1/2}}{\partial z} &= 2\,\nabla_\perp (I^{1/2}) \cdot \nabla_\perp \phi + I^{1/2}\,\nabla_\perp^2 \phi \\ \kappa\,\frac{\partial I}{\partial z} &= \nabla_\perp I \cdot \nabla_\perp \phi + I\,\nabla_\perp^2 \phi. \end{aligned} \tag{3.44}$$

Now rewriting Eq. (3.44), we obtain

$$\kappa\,\frac{\partial I}{\partial z} = \nabla_\perp^2 \Phi, \text{ where} \tag{3.45}$$

$$\nabla_\perp \Phi = I\,\nabla_\perp \phi. \tag{3.46}$$

Eq. (3.45) is known as the *transport-of-intensity equation* (TIE) [12, 10], and Φ is the auxiliary function. Note that Eq. (3.45) is the two dimensional Poisson's equation [136]. Because we know the intensities at nearby transverse planes z and $z + \delta z$ with $\delta z \to 0$, we can write

$$\frac{\partial I}{\partial z} \approx \frac{I(z + \delta z) - I(z)}{\delta z}. \tag{3.47}$$

Now using the knowledge of $\partial I/\partial z$, one first solves the Poisson equation (Eq. (3.45)) to obtain Φ, the auxiliary function, and consequently the phase ϕ. Two well known methods in this regard are Green's function approach by Teague (see Ref. [10]) and Zernike polynomial decomposition (see Ref. [12]). Other approaches towards solving Eq. (3.47) are summarized in the Section 6.3 of Ref. [8]. Further, in the transport of intensity method, intensity information from two nearby transverse planes with Δz separation is obtained, and their difference yields $\partial I/\partial z$ (see Eq. (3.47)). This is in contrast with phase extraction from phase gradients, where derivatives of phase in the transverse direction are extracted from a single intensity pattern. For instance, in a Shack-Hartmann wavefront sensor (see Section 3.6), the diffracted intensity pattern obtained from lenslet array yields the phase gradient. Similarly, phase gradients can also be extracted from an interferogram which has almost sinusoidal fringes, as outlined in Section 6.2.

Before closing this Section, we have two key observations in this regard. First, we need to specify boundary conditions as the Poisson's equation (Eq. (3.45)) is a partial differential equation. Second, even if are given the knowledge of the boundary conditions, as shown in Refs. [13, 8], this method of phase retrieval cannot retrieve phases with dislocations unambiguously because the intensity has zeros.

3.9 Noise

In previous Sections we have explained few standard phase estimation techniques from intensity measurements. As we know, these intensities are typically measured using CCD cameras. As CCDs are known to introduce noise in the measurement process [137], it is necessary to quantify them. Let $\{f_1, f_2, \ldots, f_N\}$ be the discretized function measured by the CCD consisting of N pixels. Then, the mean (μ) and variance (σ^2) of the signal are

respectively defined as

$$\mu = \frac{1}{N}\sum_{j=1}^{N} f_j, \tag{3.48}$$

$$\sigma^2 = \frac{1}{N^2}\sum_{j=1}^{N}(f_j - \mu)^2. \tag{3.49}$$

Suppose the device measures $\{f_1 + \eta_1, f_2 + \eta_2, \ldots, f_N + \eta_N\}$, where $\{\eta_1, \eta_2, \ldots, \eta_N\}$ is the noise signal with zero mean and variance σ_η^2. Now the signal-to-noise ratio (SNR) can be defined as

$$\mathrm{SNR} = 10\ \log_{10}\left(\frac{\sigma^2}{\sigma_\eta^2}\right)\mathrm{dB}. \tag{3.50}$$

Here, dB stands for decibels. For example, SNR of 10 dB implies that the variance of the noise signal is 10 % of the variance of the signal $\{f_1, f_2, \ldots, f_N\}$.

3.10 Concluding remarks

In conclusion, we have briefly discussed some widely used tools and techniques in phase estimation from intensity measurements. We have also demonstrated that the phase retrieval using phase shifting and Fourier fringe analysis require phase unwrapping. Further, we have indicated that estimation of phases with dislocations using TIE needs the knowledge of boundary conditions and is not unique as the intensity has zeros.

Chapter 4

Realization of FOOS using thin lenses of positive focal length

4.1 Introduction

In Section 2.6 we remarked that realizing any symplectic matrix $\mathbf{S} \in Sp(4, \mathbb{R})$ in terms of ray transfer matrices $\mathbf{F}(d)$ and $\mathbf{L}(f)$ is equivalent to realizing the corresponding unitary $\mathcal{U}(\mathbf{S})$ in terms of $\mathcal{F}_d$ and $\mathcal{L}_f$ on a paraxial wave field (both coherent as well as partially coherent). In fact, several methods of decomposing a ray transfer matrix pertaining to a symmetric FOOS, i.e., $\mathbf{S} = S \oplus S$ with $S \in Sp(2, \mathbb{R})$, have been discussed in the literature [138, 132, 139, 140, 141, 94, 142, 143, 144, 145, 146, 147]. And the use of matrix methods and group theoretic techniques to arrive at the respective decompositions have been detailed in Refs. [148, 117, 114, 96]. The problem of decomposing the most general S in terms of elementary matrices was discussed in Refs. [149, 139, 138, 132, 94]. For example, in Ref. [132] four possible decompositions for a ray transfer matrix was outlined, and in Ref. [138], eight possible decompositions for a ray transfer matrix was outlined. And these decompositions could be in principle used to arrive at other decompositions.

When a ray transfer matrix S is decomposed in terms of $F(d)$ and $L(f)$, then such a decomposition corresponds to a FOOS which realizes the optical transformation in terms of the corresponding free propagations and lenses. In general, two different FOOS can realize the same optical transformation [132, 150], and they are of different size and structure. In Ref. [141] it was implied that not all $S \in Sp(2, \mathbb{R})$ can be physically realized as a symmetric FOOS. For instance, it was argued that it is impossible to physically realize propagation through a negative distance, i.e., inverse free propagation, since it would require a medium of 'negative thickness'.

In Ref. [94] the problem of realizing the most general symmetric FOOS using thin

lenses and free propagation was addressed. It was not only shown that inverse free propagation was physically realizable, but that every ray transfer matrix (optical transformation) S could be implemented as a symmetric FOOS which uses not more three lenses of arbitrary focal length. An alternative proof was provided in Ref. [151]. In Ref. [95], it was proved three convex lenses, as opposed to three thin lenses as in Ref. [94], were sufficient in the realization of such systems. In fact, it was proved that five convex lenses of unit focal length would realize any such system. It was further observed that any convex (concave) lens of arbitrary focal length can be realized by not more than three (two) convex lenses of unit focal length.

Having discussed the realization of symmetric FOOS, we now briefly review the asymmetric case. In the seminal work of Ref. [94], it was indicated that any element of $Sp(4, \mathbb{R})$ can be realized using finite sequence of free propagation and thin lenses (with positive or negative focal length) through making use of a theorem pertaining to Lie groups. Although they concluded that it is possible to synthesize any element $\mathbf{S} \in Sp(4, \mathbb{R})$ using finite number of thin lenses and free propagation, they did not provide an explicit decomposition to realize any such $\mathbf{S}$. As a continuation to this work, Simon and Wolf [96] gave specific examples of asymmetric FOOS such as partial Fourier transform, gyrator, cross gyrator, and image reflector. In our work, instead of following the group theoretic approach as in Ref. [94], we realize any general FOOS using matrix identities. Here, some of the matrix identities have been borrowed directly from the author's previous work on realization of symmetric FOOS [95].

In this Chapter we show that any general FOOS can be realized using elementary optical transformations including free propagation, thin convex lenses, and thin cylindrical lenses of positive focal length. That is, we explicitly realize any $\mathbf{S} \in Sp(4, \mathbb{R})$ as a sequence in matrices $\mathbf{F}(d)$, $\mathbf{L}(f)$, $\mathbf{L}_x(f)$, and $\mathbf{L}_y(f)$, with $f > 0$. First, we realize some examples of symmetric FOOS using free propagation and thin convex lenses developed by the author in Ref. [95]. By making use of these identities, we realize some standard examples of asymmetric FOOS including differential magnifiers and differential fractional Fourier transformations. Besides, using Euler decomposition, we prove that any general FOOS won't require more than 14 cylindrical lenses of positive focal length and 4 convex lenses to realize.

4.2 Realization of symmetric FOOS using thin lenses

Now we present below the realization of few symmetric FOOS. Even though these identities can readily be verified by elementary 2×2 matrix multiplications, a formal treatment on how to obtain them in a general setting is available in Ref. [95].

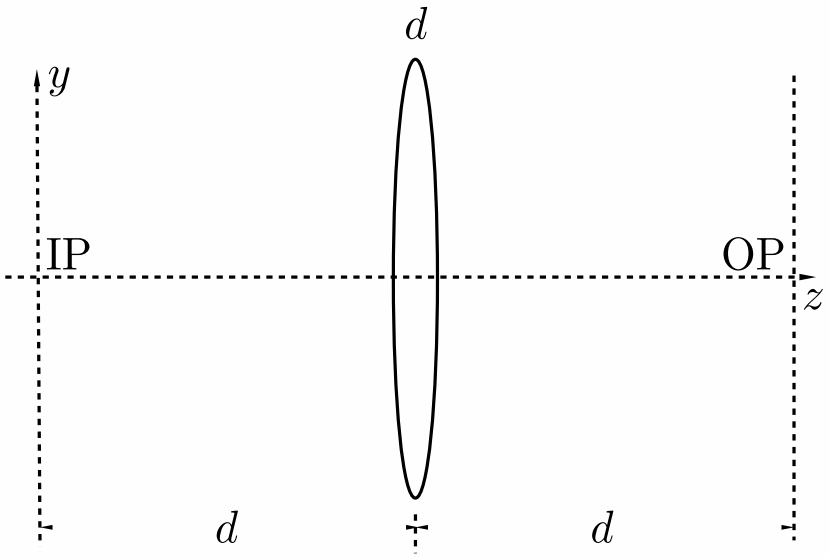

Figure 4.1: Realization of the ray transfer matrix σ_d (see Eq. (4.1)) associated with the Fourier transformation using thin lens and free propagations. Here, IP and OP refer to input plane and output plane respectively.

Fourier transformation : First we start with the ray transfer matrix associated with the Fourier transformation. Eq. (10) of Ref. [95] reads

$$\sigma_d \equiv \begin{bmatrix} 0 & d \\ -1/d & 0 \end{bmatrix} = F(d)\, L(d)\, F(d). \tag{4.1}$$

The corresponding schematic is shown in Figure 4.1.

Negative identity : By Eq. (13) of Ref. [95], the realization of ray transfer matrix associated with the negative identity transformation is

$$-\mathbb{1} = F(2d)\, L(d)\, F(2d)\, L(d), \tag{4.2}$$

and the corresponding schematic is shown in Figure 4.2.

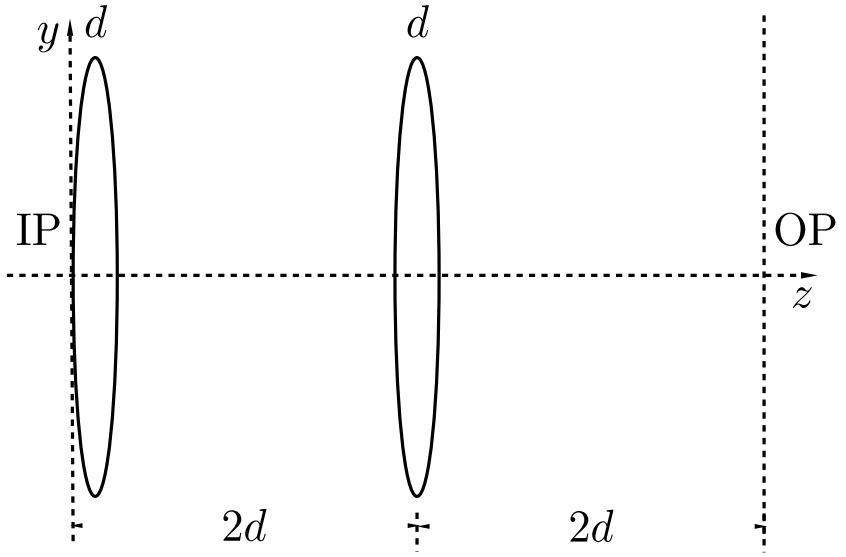

Figure 4.2: Realization of the ray transfer matrix $-\mathbb{1}$ (see Eq. (4.2)) using thin lens and free propagations. Here, IP and OP refer to input plane and output plane respectively.

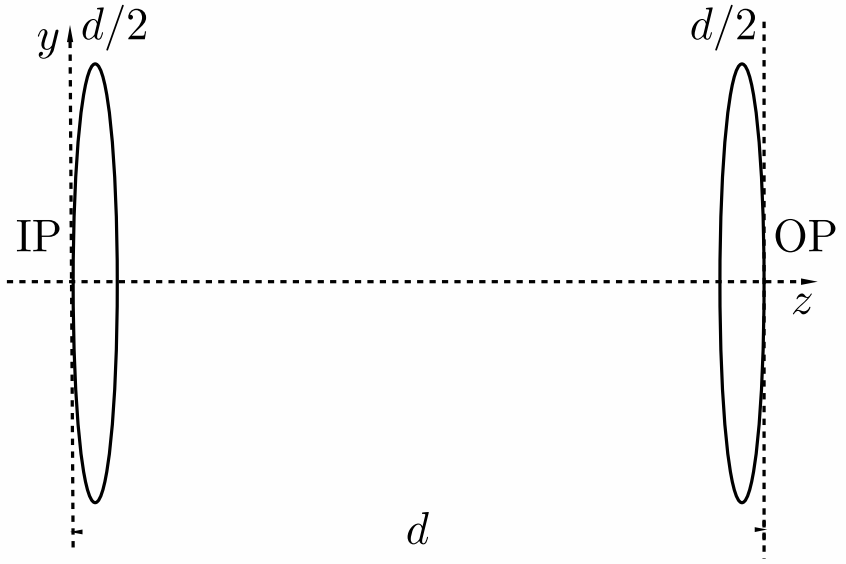

Figure 4.3: Realization of the ray transfer matrix $-F(-d)$ (see Eq. (4.3)). Here, IP and OP refer to input plane and output plane respectively.

Negative of inverse free propagation : The ray transfer matrix associated with this transformation is $-F(-d)$. Pre-multiplying both sides of Eq. (4.2) by $F(-2d)$ and replacing d with $d/2$, we obtain

$$-F(-d) = L\left(\frac{d}{2}\right) F(d)\, L\left(\frac{d}{2}\right). \tag{4.3}$$

The corresponding schematic is shown in Figure 4.3.

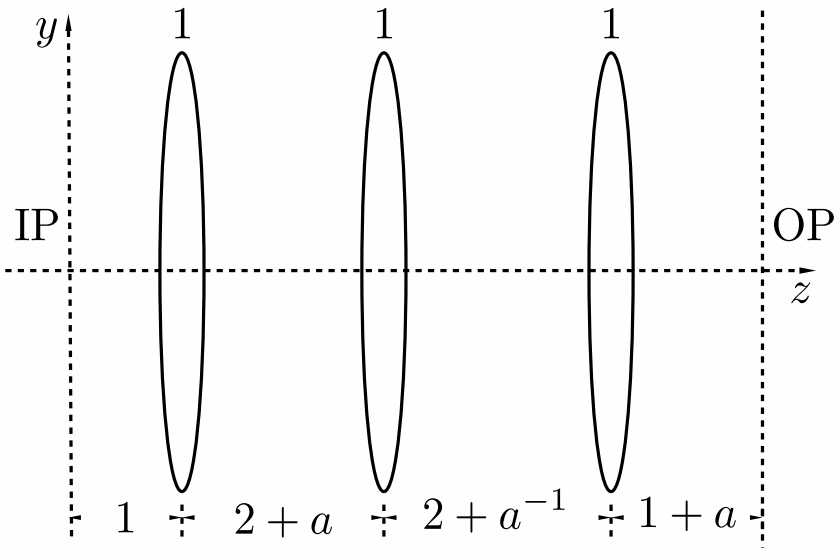

Figure 4.4: Realization of the ray transfer matrix M_a (see Eq. (4.5)) associated with the positive magnifier transformation. Here, IP and OP refer to input plane and output plane respectively, and the distances are not to scale.

Magnifier transformation : The ray transfer matrix associated with the magnifier transformation is given by [94, 95]

$$M_a \equiv \begin{bmatrix} a & 0 \\ 0 & 1/a \end{bmatrix}, \tag{4.4}$$

with a being real and $\neq 0$. When $a > 0$ ($a < 0$), M_a is called as positive (negative) magnifier. For positive magnifier, by Eq. (36) of Ref. [95], the realization is

$$M_a = F(1+a)\, L(1)\, F\left(2+\frac{1}{a}\right) L(1)\, F(2+a)\, L(1)\, F(1). \tag{4.5}$$

For negative magnifier, a straight-forward multiplication yields the realization

$$M_{-a} = L(a)\, F(1+a)\, L(1)\, F\left(1+\frac{1}{a}\right). \tag{4.6}$$

The schematic diagrams for the realization of M_a and M_{-a} are shown in Figures 4.4 and 4.5 respectively.

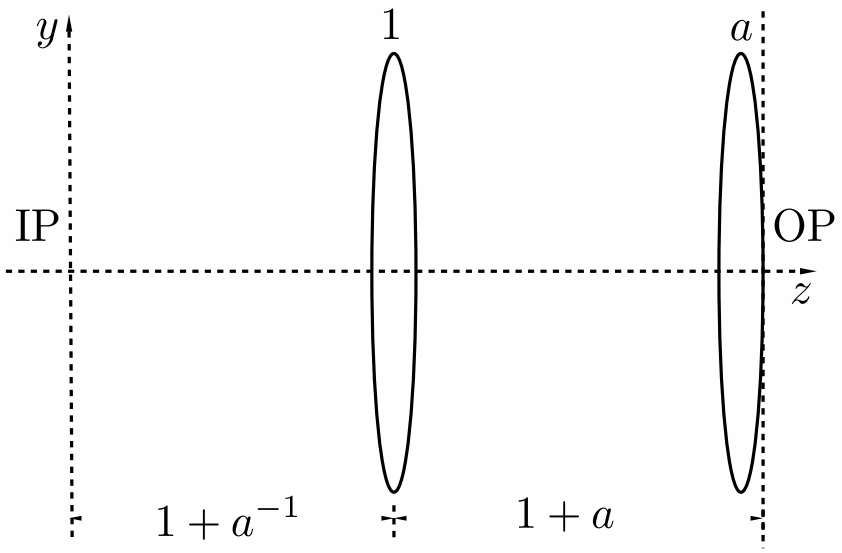

Figure 4.5: Realization of the ray transfer matrix M_{-a} (see Eq. (4.6)) associated with the negative magnifier transformation. Here, IP and OP refer to input plane and output plane respectively, and the distances are not to scale.

Fractional Fourier transformation : is defined as [95]

$$R_\alpha \equiv \begin{bmatrix} \cos\alpha & -\sin\alpha \\ \sin\alpha & \cos\alpha \end{bmatrix}, \tag{4.7}$$

with $0 \leq \alpha < 2\pi$. When $0 < \alpha < 3\pi/2$, we make use of Eq. (33) of Ref. [95] and obtain

$$R_\alpha = F\left(1+\cot\frac{\alpha}{2}\right) L(1)\, F(2+\sin\alpha)\, L(1)\, F\left(1+\cot\frac{\alpha}{2}\right), \tag{4.8}$$

and the corresponding schematic is shown in Figure 4.6. When $\alpha = 3\pi/2$, $R_\alpha = \sigma_1$ (Eq. (4.1)), and we therefore require one lens for realization. Now, when $3\pi/2 < \alpha \leq 2\pi$,

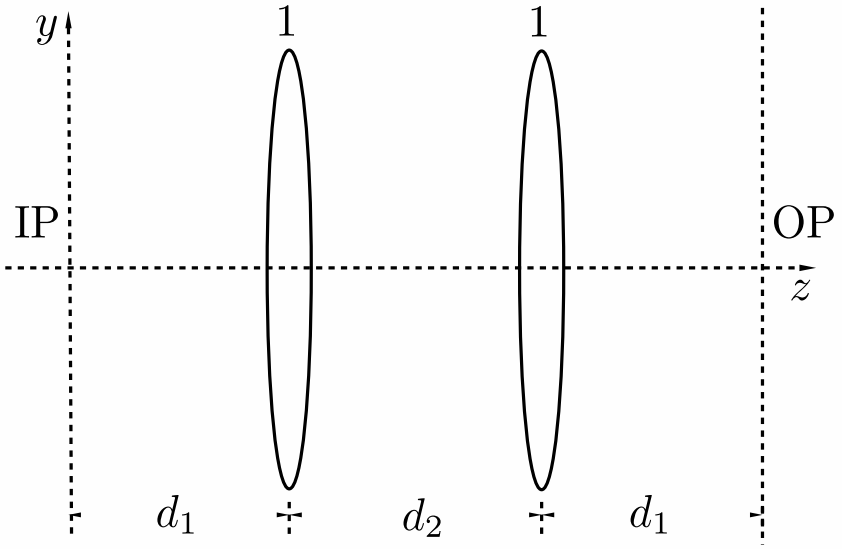

Figure 4.6: Realization of the ray transfer matrix R_α (see Eq. (4.8)) associated with the fractional Fourier transformation with $0 < \alpha < 3\pi/2$, $d_1 = 1 + \cot(\alpha/2)$, and $d_2 = 2 + \sin\alpha$. Here, IP and OP refer to input plane and output plane respectively, and the distances are not to scale.

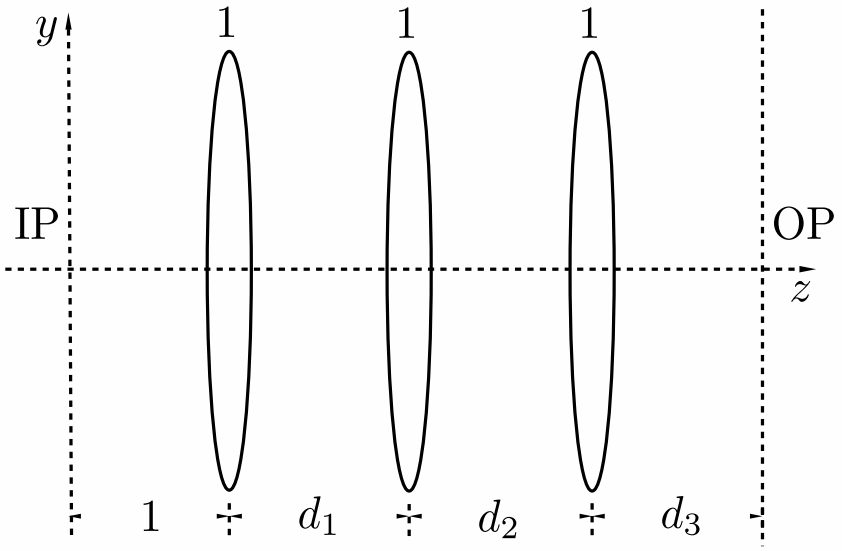

Figure 4.7: Realization of the ray transfer matrix R_α (see Eq. (4.9)) associated with the fractional Fourier transformation with $3\pi/2 < \alpha \leq 2\pi$, $d_1 = 2 + (1 + \sin\alpha)/\cos\alpha$, $d_2 = 2 + \cos\alpha$, and $d_3 = 1 + (1 - \sin\alpha)/\cos\alpha$. Here, IP and OP refer to input plane and output plane respectively, and the distances are not to scale.

by Eq. (36) of Ref. [95], we have

$$R_\alpha = F\left(1+\frac{1-\sin\alpha}{\cos\alpha}\right) L(1)\, F(2+\cos\alpha)\, L(1)\, F\left(2+\frac{1+\sin\alpha}{\cos\alpha}\right) L(1)\, F(1). \quad (4.9)$$

The corresponding schematic is shown in Figure 4.7. Finally, when $\pi < \alpha < 2\pi$, it can also be noted that

$$R_\alpha = F\left(-\tan\frac{\alpha}{2}\right) L\left(\frac{-1}{\sin\alpha}\right) F\left(-\tan\frac{\alpha}{2}\right), \quad (4.10)$$

and the corresponding schematic is shown in Figure 4.8.

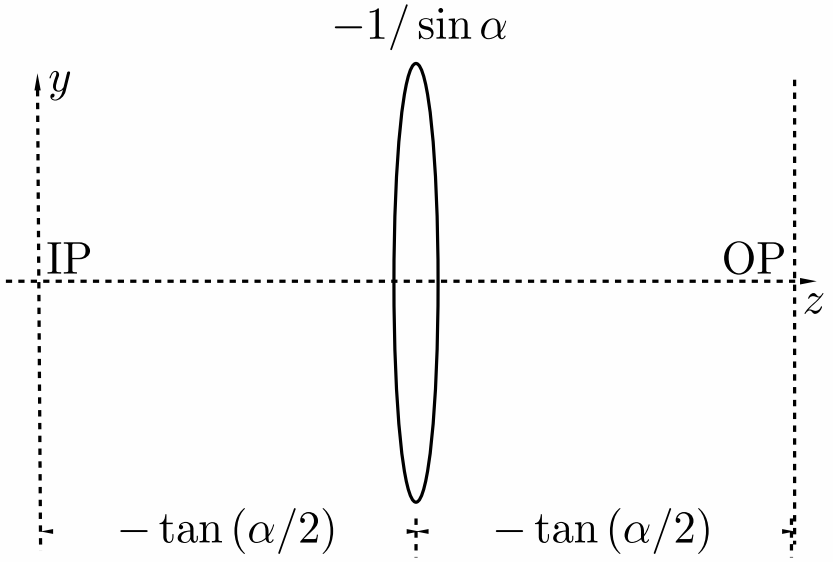

Figure 4.8: Realization of the ray transfer matrix R_α (see Eq. (4.10)) associated with the fractional Fourier transformation with $\pi < \alpha < 2\pi$. Here, IP and OP refer to input plane and output plane respectively, and the distances are not to scale.

Having realized some examples of symmetric FOOS, we now realize the most general FOOS, i.e., $\mathbf{S} \in Sp(4,\mathbb{R})$, in the following Sections.

4.3 Euler decomposition and Euler rotations

As is well known, any symplectic matrix $\mathbf{S} \in Sp(4,\mathbb{R})$ can be Euler decomposed as [114, 152, 153]

$$\mathbf{S} = \mathbf{R}_1 \, \mathbf{M} \, \mathbf{R}_2^T, \tag{4.11}$$

where both $\mathbf{R}_1$ and $\mathbf{R}_2$ are orthogonal and symplectic, i.e., $\mathbf{R}_1,\ \mathbf{R}_2 \in Sp(4,\mathbb{R}) \cap O(4,\mathbb{R})$, and $\mathbf{M} = M_a \oplus M_b$ with $M_a = \mathrm{diag}\,\{a, a^{-1}\}$ and $M_b = \mathrm{diag}\,\{b, b^{-1}\}$. To this end, we first note that $Sp(4,\mathbb{R})$ is a non-compact group. Also, both $\mathbf{R}_1$ and $\mathbf{R}_2$ are elements of the symplectic orthogonal group $Sp(4,\mathbb{R}) \cap O(4,\mathbb{R})$ (the maximal compact subgroup of $Sp(4,\mathbb{R})$ and is isomorphic to unitary group $\mathrm{U}(2)$). Further, $\mathbf{M}$ is an element of non-compact group [114]. Now consider the quadratic operators [128] :

$$\hat{J}_0 = \frac{1}{4}(\hat{x}^2 + \hat{y}^2 + \hat{p}_x^2 + \hat{p}_y^2) - \frac{1}{2}, \tag{4.12}$$

$$\hat{J}_1 = \frac{1}{4}(\hat{x}^2 - \hat{y}^2 + \hat{p}_x^2 - \hat{p}_y^2), \tag{4.13}$$

$$\hat{J}_2 = \frac{1}{2}(\hat{x}\hat{y} + \hat{p}_x\hat{p}_y), \tag{4.14}$$

$$\hat{J}_3 = \frac{1}{2}(\hat{x}\hat{p}_y - \hat{y}\hat{p}_x). \tag{4.15}$$

It is easily verified that $\hat{J}_0$ commutes with $\hat{J}_j$, and $[\hat{J}_j, \hat{J}_k] = i\epsilon_{jkl}\,\hat{J}_l$, where j, k, and l can be 1, 2, or 3. While $\hat{J}_0$ generates $\mathrm{U}(1)$, $\hat{J}_1$, $\hat{J}_2$, and $\hat{J}_3$ generate $\mathrm{SU}(2)$.

Remark : By Eqs. (4.12)-(4.15) we observe that while $\hat{J}_0$ generates equal amount of rotations in the x–p_x and y–p_y planes of the phase space, $\hat{J}_1$ generates equal and opposite amount of rotations in the x–p_x and y–p_y planes. Also, $\hat{J}_2$ is a generator of equal amount of rotations in the x–p_y and y–p_x planes. Finally, $\hat{J}_3$ produces equal amount of rotations in x–y and p_x–p_y planes, i.e., spatial rotation in the transverse x–y plane [128]. Here, we note that any unitary operator generated by $\hat{J}_0$, $\hat{J}_1$, $\hat{J}_2$, and $\hat{J}_3$ and their linear combination results in a compact transformation in the phase space.

Now define the unitary operators $\mathcal{J}_j = \exp\,(i\,2\alpha\hat{J}_j)$, with $j = 0, 1, 2, 3$. We then have

$$\mathcal{J}_j^\dagger \, \hat{\xi} \, \mathcal{J}_j = \mathbf{J}_j(\alpha) \, \hat{\xi}, \tag{4.16}$$

such that $\mathbf{J}_j(\alpha) \in Sp(4,\mathbb{R}) \cap O(4,\mathbb{R})$. Performing the necessary algebra it is obtained

that

$$\mathbf{J}_0(\alpha) = \begin{bmatrix} R_\alpha & 0 \\ 0 & R_\alpha \end{bmatrix}, \tag{4.17}$$

$$\mathbf{J}_1(\alpha) = \begin{bmatrix} R_\alpha & 0 \\ 0 & R_{-\alpha} \end{bmatrix}, \tag{4.18}$$

$$\mathbf{J}_2(\alpha) = \begin{bmatrix} \cos(\alpha)\,\mathbb{1} & -\sin(\alpha)\,\sigma_1 \\ -\sin(\alpha)\,\sigma_1 & \cos(\alpha)\,\mathbb{1} \end{bmatrix}, \tag{4.19}$$

$$\mathbf{J}_3(\alpha) = \begin{bmatrix} \cos(\alpha)\,\mathbb{1} & \sin(\alpha)\,\mathbb{1} \\ -\sin(\alpha)\,\mathbb{1} & \cos(\alpha)\,\mathbb{1} \end{bmatrix}, \tag{4.20}$$

where R_α is the rotation matrix (see Eq. (4.7)) and σ_1 is the ray transfer matrix associated with the Fourier transform (see Eq. (4.1)). Here $0 \leq \alpha < 2\pi$ and it is readily seen that $\mathbf{J}_j(\alpha)$ with $j = 0, 1, 2, 3$ are one-parameter subgroups of $O(4, \mathbb{R})$. In particular, given that any $\mathcal{U} \in \mathrm{U}(2)$ can be decomposed using *Euler rotations* [154, 115, 128] as

$$\mathcal{U} = \exp\left(i\,2\alpha \hat{J}_0\right) \exp\left(i\,2\beta \hat{J}_j\right) \exp\left(i\,2\gamma \hat{J}_k\right) \exp\left(i\,2\delta \hat{J}_j\right), \tag{4.21}$$

with $j,\ k \in 1, 2, 3$ and $j \neq k$. Then by Eqs. (4.17)-(4.20), any $\mathbf{R} \in Sp(4, \mathbb{R}) \cap O(4, \mathbb{R})$ such that $\mathcal{U}^\dagger\, \hat{\xi}\, \mathcal{U} = \mathbf{R}\, \hat{\xi}$, is realized as

$$\mathbf{R} = \mathbf{J}_0(\alpha)\, \mathbf{J}_j(\beta)\, \mathbf{J}_k(\gamma)\, \mathbf{J}_j(\delta). \tag{4.22}$$

Since $\mathbf{R}$ is a representative of $\mathrm{U}(2) = \mathrm{U}(1) \times \mathrm{SU}(2)$ with $\mathbf{J}_0(\alpha)$ representing $\mathrm{U}(1)$ and $\mathbf{J}_j(\beta)\, \mathbf{J}_k(\gamma)\, \mathbf{J}_j(\delta)$ representing $\mathrm{SU}(2)$, it is readily seen that $0 \leq \alpha < 2\pi$, $0 \leq \beta,\ \delta < \pi$, and $0 \leq \gamma \leq \pi/2$ or $\pi \leq \gamma \leq 3\pi/2$ [155]. Note that $\gamma \to \gamma + \pi$ results in $\mathbf{R} \to -\mathbf{R}$. Further in Eqs. (4.19) and (4.20), $\mathbf{J}_2(\theta)$ and $\mathbf{J}_3(\theta)$ are readily identified as the *cross gyrator* and *gyrator* respectively of Ref. [96].

Now to realize $\mathbf{M}$ of Eq. (4.11), define the unitary operator

$$\mathcal{M}(\alpha_1, \alpha_2) = \exp\left\{ \frac{-i}{2} \left[\alpha_1 (\hat{x}\, \hat{p}_x + \hat{p}_x\, \hat{x}) + \alpha_2 (\hat{y}\, \hat{p}_y + \hat{p}_y\, \hat{y}) \right] \right\}. \tag{4.23}$$

We then have

$$\begin{aligned} &\mathcal{M}(\alpha_1, \alpha_2)^\dagger\, \hat{\xi}\, \mathcal{M}(\alpha_1, \alpha_2) = \mathbf{M}\, \hat{\xi}, \ \text{ with} \\ &\mathbf{M} = \mathrm{diag}\,\{a, 1/a, b, 1/b\} \equiv M_a \oplus M_b, \end{aligned} \tag{4.24}$$

and $a = \exp(\alpha_1)$, and $b = \exp(\alpha_2)$. With this, if one obtains decompositions for $\mathbf{R}$ and $\mathbf{M}$ in terms of $\mathbf{F}(d)$, $\mathbf{L}(f)$, $\mathbf{L}_x(f)$, and $\mathbf{L}_y(f)$, then by Eq. (4.11), any $\mathbf{S}$ is realized.

4.4 Some elementary decompositions

In this Section, we work out the decomposition for a symplectic matrix $\mathbf{S}$ of the form $\mathbf{S} = S_1 \oplus S_2$, where $S_1,\ S_2 \in Sp(2, \mathbb{R})$. We begin with the example of one-sided free propagation.

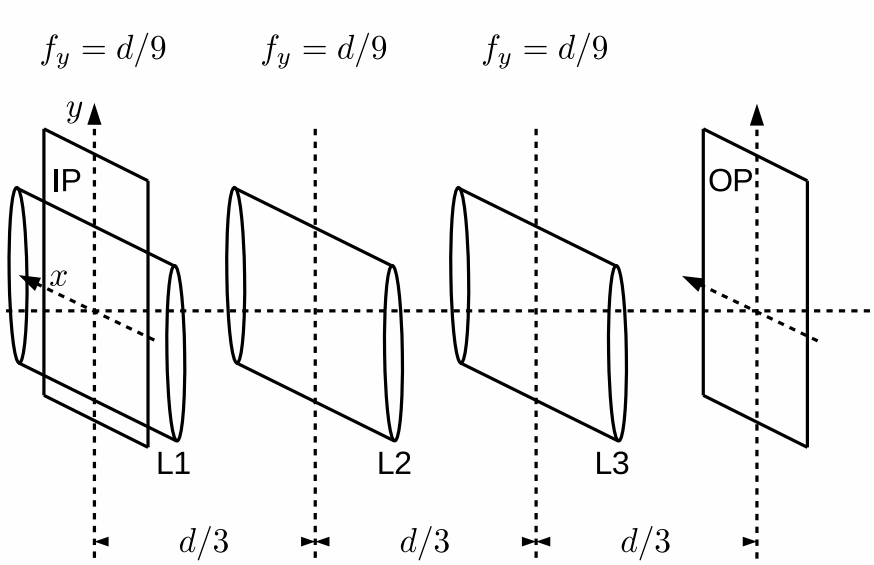

Figure 4.9: Shown here is the lens arrangement to realize one-sided free propagation (see Eq. (4.25)). Here, IP and OP stand for input plane and output plane respectively.

4.4.1 One-sided free propagation

It is a unitary transformation on a paraxial light field such that in one of the transverse coordinates, say x, the wave field propagates by distance d, while on the other transverse coordinate y the wave field remains unaffected. The symplectic matrix $\mathbf{S}$ corresponding to such a unitary transformation is given by $\mathbf{S} = F(d) \oplus \mathbb{1}$, and can be realized as

$$\begin{bmatrix} F(d) & 0 \\ 0 & \mathbb{1} \end{bmatrix} = \mathbf{F}\left(\frac{d}{3}\right) \mathbf{L}_y\left(\frac{d}{9}\right) \mathbf{F}\left(\frac{d}{3}\right) \mathbf{L}_y\left(\frac{d}{9}\right) \mathbf{F}\left(\frac{d}{3}\right) \mathbf{L}_y\left(\frac{d}{9}\right). \tag{4.25}$$

Clearly, one-sided free propagation consumes three cylindrical lenses of positive focal length to realize. The corresponding schematic is shown in Figure 4.9.

4.4.2 Differential free propagation

It is a unitary transformation whereby a paraxial wave field propagates by different distances in the coordinate axes x and y respectively. Let $d_1,\ d_2 > 0$ with $d_1 > d_2$. Then the $\mathbf{S}$ corresponding to the differential free propagation is given by

$$\begin{bmatrix} F(d_1) & 0 \\ 0 & F(d_2) \end{bmatrix} = \mathbf{F}(d_2) \times \begin{bmatrix} F(d_1 - d_2) & 0 \\ 0 & \mathbb{1} \end{bmatrix}. \tag{4.26}$$

Here the second matrix in the RHS is realized using Eq. (4.25). Similarly, if $d_1 < d_2$, then

$$\begin{bmatrix} F(d_1) & 0 \\ 0 & F(d_2) \end{bmatrix} = \mathbf{F}(d_1) \times \begin{bmatrix} \mathbb{1} & 0 \\ 0 & F(d_2 - d_1) \end{bmatrix}. \tag{4.27}$$

Note that for the realizations in Eqs. (4.26) and (4.27), three cylindrical lenses of positive focal length have been used.

4.4.3 Differential inverse free propagation

It is a unitary transformation in which a paraxial wave field "inverse free propagates" by different distances in the transverse coordinates x and y and has its corresponding symplectic matrix $\mathbf{S}$ given by $\mathbf{S} = F(-d_1) \oplus F(-d_2)$ with $d_1,\ d_2 \geq 0$. Now we know that the symplectic matrix $\mathbf{S}$ corresponding to the negative of inverse free propagation by distance d units by Eq. (4.3) is

$$-\mathbf{F}(-d) = \mathbf{L}\left(\frac{d}{2}\right) \mathbf{F}(d)\, \mathbf{L}\left(\frac{d}{2}\right). \tag{4.28}$$

The corresponding schematic is shown in Figure 4.10. Further, $-F(-d) \oplus -\mathbb{1}$ can be decomposed as

$$\begin{bmatrix} -F(-d) & 0 \\ 0 & -\mathbb{1} \end{bmatrix} = \mathbf{L}_x\left(\frac{d}{2}\right) \mathbf{F}\left(\frac{d}{4}\right) \mathbf{L}_y\left(\frac{d}{4}\right) \mathbf{F}\left(\frac{d}{2}\right) \mathbf{L}_y\left(\frac{d}{4}\right) \mathbf{F}\left(\frac{d}{4}\right) \mathbf{L}_x\left(\frac{d}{2}\right). \tag{4.29}$$

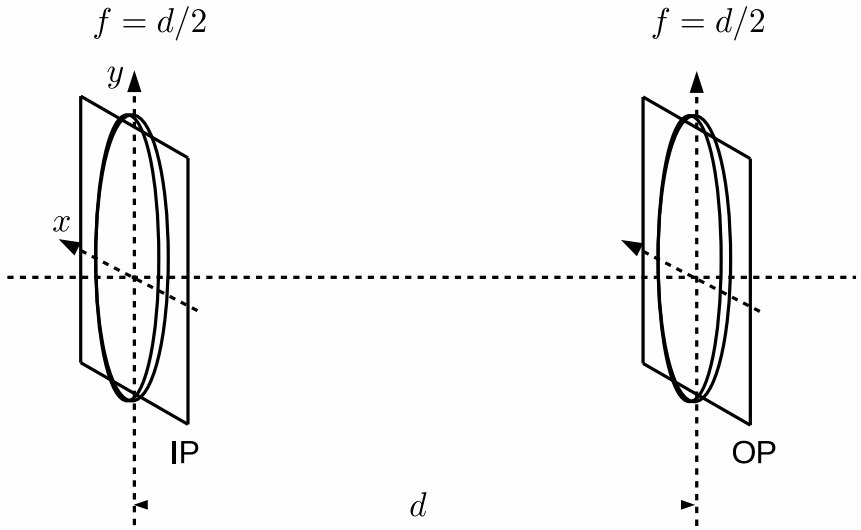

Figure 4.10: Shown here is the lens arrangement to realize negative of inverse free propagation (see Eq. (4.28)). Here, IP and OP stand for input plane and output plane respectively.

Figure 4.11 shows the corresponding lens arrangement. Now by Eqs. (4.28) and (4.29), $F(-d_1) \oplus F(-d_2)$ is decomposed as follows : Let $d_1,\ d_2 > 0$ with $d_1 > d_2$. Then

$$\begin{bmatrix} F(-d_1) & 0 \\ 0 & F(-d_2) \end{bmatrix} = -\mathbf{F}(-d_2) \times \begin{bmatrix} -F(d_2 - d_1) & 0 \\ 0 & -\mathbb{1} \end{bmatrix}. \tag{4.30}$$

Now when $d_1 < d_2$, we have

$$\begin{bmatrix} F(-d_1) & 0 \\ 0 & F(-d_2) \end{bmatrix} = -\mathbf{F}(-d_1) \times \begin{bmatrix} -\mathbb{1} & 0 \\ 0 & -F(d_1 - d_2) \end{bmatrix}. \tag{4.31}$$

It is easily seen from Eqs. (4.30) and (4.31) that differential inverse free propagation is realized by two convex lenses and four cylindrical lenses of positive focal length. Note that in Eq. (4.30) ((4.31)), by setting $d_2 = 0\,(d_1 = 0)$, we realize one-sided inverse free propagation, i.e., $F(-d_1) \oplus \mathbb{1}\,(\mathbb{1} \oplus F(-d_2))$.

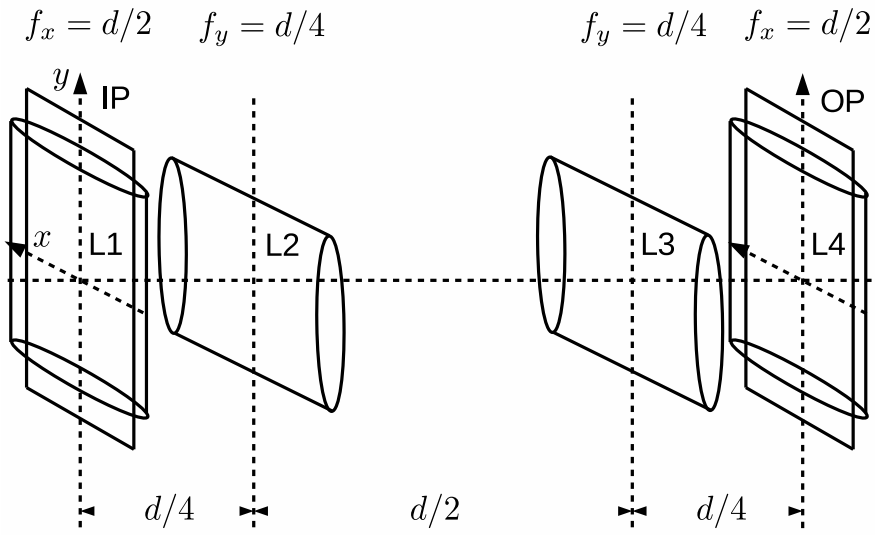

Figure 4.11: Shown here is the lens arrangement to realize $-F(-d) \oplus -\mathbb{1}$ (see Eq. (4.29)). Here, IP and OP stand for input plane and output plane respectively.

4.4.4 Partial Fourier transformation

The symplectic matrix $\mathbf{S}$ corresponding to two dimensional Fourier transform is given by [118, 111]

$$\sigma_d \oplus \sigma_d, \tag{4.32}$$

where σ_d is ray transfer matrix associated with the Fourier transform (see Eq. (4.1)) with $d > 0$. Partial Fourier transformer performs Fourier transform operation on the wave field in one transverse coordinate, say x, and performs identity transform in the other transverse coordinate y. That is, the symplectic matrix corresponding to the partial Fourier transform is given by

$$\mathbf{P}_y(d) \equiv \mathbb{1} \oplus \sigma_d. \tag{4.33}$$

We can write

$$\mathbf{P}_y(d) = \mathbf{F}\left(\frac{d}{3}\right)\mathbf{L}_x\left(\frac{2d}{9}\right)\mathbf{F}\left(\frac{2d}{3}\right)\mathbf{L}_x\left(\frac{2d}{9}\right)\mathbf{L}_y(d)\,\mathbf{F}\left(\frac{2d}{3}\right)\mathbf{L}_x\left(\frac{2d}{9}\right)\mathbf{F}\left(\frac{d}{3}\right). \tag{4.34}$$

Note that in realizing $\mathbf{P}_y(d)$, we have made use of four cylindrical lenses of positive focal length. Figure 4.12 shows the corresponding lens arrangement.

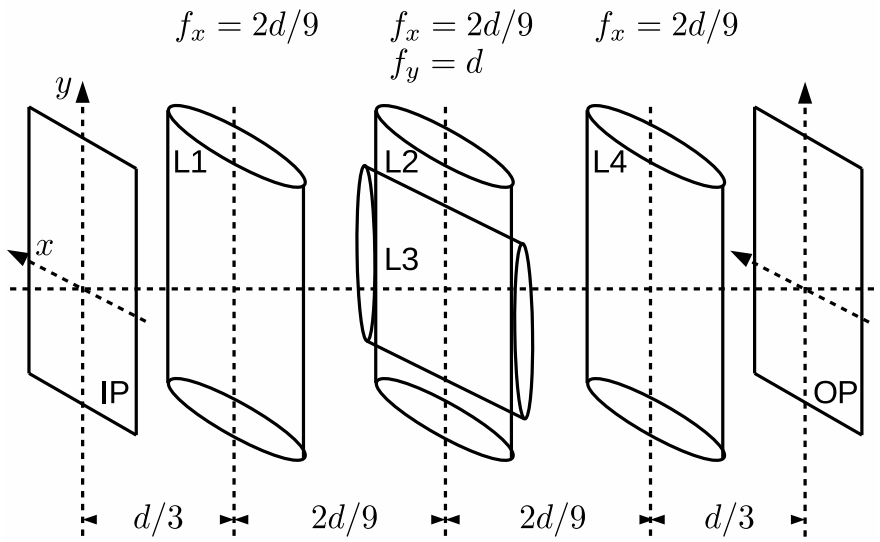

Figure 4.12: Shown here is the lens arrangement to realize partial Fourier transformation (see Eq. (4.34)). Here, IP and OP stand for input plane and output plane respectively.

4.4.5 Inverse partial Fourier transformation

The symplectic matrix $\mathbf{S}$ corresponding to the inverse partial Fourier transformation is given by $\mathbf{P}_y^{-1}(d) = \mathbb{1} \oplus \sigma_{-d}$. Now $\mathbf{P}_y^{-1}(d)$ can be rewritten as

$$\begin{aligned} \mathbf{P}_y^{-1}(d) &= \tilde{\mathbf{P}}_y(d) \times (-\mathbb{1}), \text{ where} \\ \tilde{\mathbf{P}}_y(d) &\equiv -\mathbb{1} \oplus \sigma_d. \end{aligned} \tag{4.35}$$

Now $\tilde{\mathbf{P}}_y(d)$ is realized as

$$\tilde{\mathbf{P}}_y(d) = \mathbf{F}(d)\,\mathbf{L}_x\left(\frac{d}{2}\right)\mathbf{L}_y(d)\,\mathbf{F}(d)\,\mathbf{L}_x\left(\frac{d}{2}\right). \tag{4.36}$$

Note that $-\mathbb{1}$ can be realized as in Eq. (4.2). With this,

$$\mathbf{P}_y^{-1}(d) = \mathbf{F}(d)\,\mathbf{L}_x\left(\frac{d}{2}\right)\mathbf{L}_y(d)\,\mathbf{F}(d)\,\mathbf{L}_x\left(\frac{d}{2}\right)\mathbf{F}(2d)\,\mathbf{L}(d)\,\mathbf{F}(2d)\,\mathbf{L}(d). \tag{4.37}$$

That is, two convex lenses and three cylindrical lenses of positive focal length are required to realize $\mathbf{P}_y^{-1}(d)$. Figure 4.13 shows the corresponding lens arrangement.

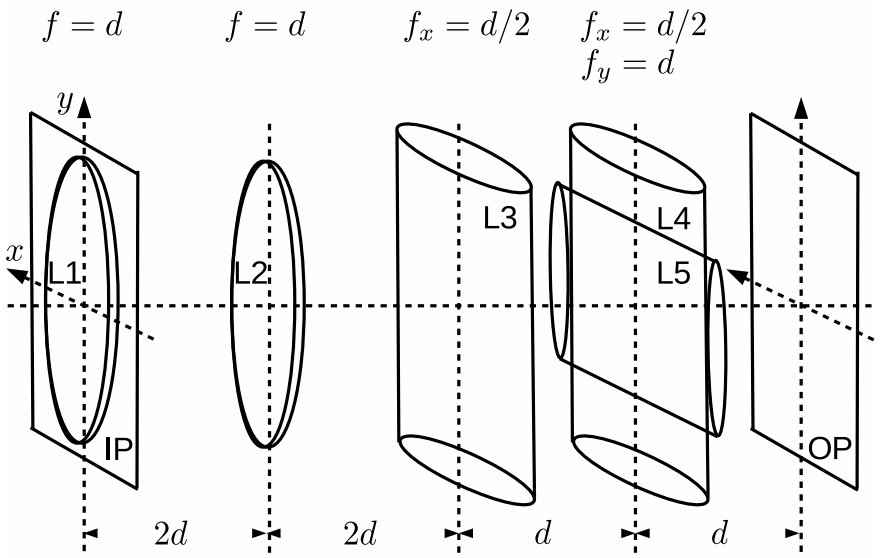

Figure 4.13: Shown here is the lens arrangement to realize inverse partial Fourier transformation (see Eq. (4.37)). Here, IP and OP stand for input plane and output plane respectively.

4.4.6 Image reflector

It is a unitary transformation on a paraxial wave field such that one of the transverse coordinates, say y, is replaced with $-y$. The symplectic matrix $\mathbf{S}$ corresponding to the image reflector is given by $\mathbf{I}_y \equiv \mathbb{1} \oplus (-\mathbb{1})$ and can be realized as

$$\mathbf{I}_y = \mathbf{F}\left(\frac{3d}{2}\right)\mathbf{L}_x(d)\,\mathbf{F}(3d)\,\mathbf{L}_x(d)\,\mathbf{L}_y\left(\frac{9d}{4}\right)\mathbf{F}(3d)\,\mathbf{L}_x(d)\,\mathbf{F}\left(\frac{3d}{2}\right)\mathbf{L}_y\left(\frac{9d}{4}\right). \qquad (4.38)$$

In other words, the image reflector is realized using five cylindrical lenses of positive focal length. Figure 4.14 shows the corresponding lens arrangement.

4.4.7 Differential magnifiers

It is a unitary transformation on a paraxial wave field such that the transverse coordinates x and y are scaled differentially. The symplectic matrix $\mathbf{S}$ corresponding to differential

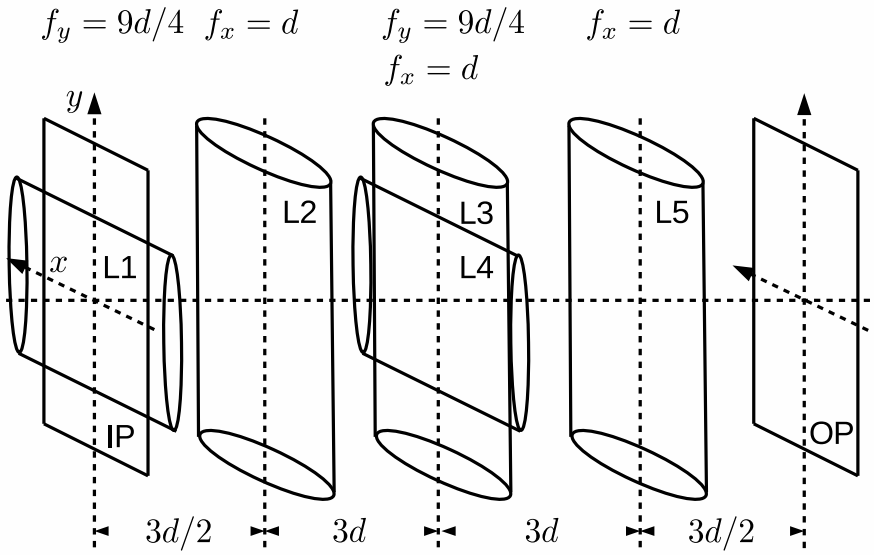

Figure 4.14: Shown here is the lens arrangement to realize image reflector (see Eq. (4.38)). Here, IP and OP stand for input plane and output plane respectively.

magnifier is $\mathbf{M}$ as stated in Eq. (4.24). $\mathbf{M}$ can be realized as

$$\begin{aligned}\mathbf{M} &= \begin{bmatrix} -M_a & 0 \\ 0 & F(t) \end{bmatrix} (-\mathbf{F}(-t)) \begin{bmatrix} F(t) & 0 \\ 0 & -M_b \end{bmatrix} \\ &= \mathbf{L}_x(ad)\, \mathbf{F}[(a+1)d]\, \mathbf{L}_x(d)\, \mathbf{F} \left[\frac{(a+1)d}{a}\right] \\ &\times \mathbf{L}\left(\frac{t}{2}\right) \mathbf{F}(t)\, \mathbf{L}\left(\frac{t}{2}\right) \\ &\times \mathbf{L}_y(b)\, \mathbf{F}(b+1)\, \mathbf{L}_y(1)\, \mathbf{F}\left(\frac{b+1}{b}\right), \end{aligned} \tag{4.39}$$

where $t = (b+1)^2/b$ and $d = at/(a+1)^2$. Note that in realizing $-\mathbf{F}(-t)$, we have made use of Eq. (4.28). Also, the matrices $-M_a \oplus F(t)$ and $F(t) \oplus (-M_b)$ were realized as in Eq. (4.6). So $\mathbf{M}$ is realized using four cylindrical lenses of positive focal length and two convex lenses.

4.4.8 Differential fractional Fourier transformations

It is a unitary transformation on a paraxial wave field such that the operator arrays $[\hat{x}, \hat{p}_x]^T$ and $[\hat{y}, \hat{p}_y]^T$ are rotated by different amounts. The corresponding symplectic matrix $\mathbf{S}$ is

$\mathbf{D}_{\alpha,\beta} \equiv R_\alpha \oplus R_\beta$ (see (4.7)). Note that $\mathbf{D}_{\alpha,\alpha} = \mathbf{J}_0(\alpha)$. Now we know from Eqs. (4.8) and (4.10) that $\mathbf{J}_0(\alpha)$ of Eq. (4.17) can be decomposed as

$$\mathbf{J}_0(\alpha) = \mathbf{F}\left(1+\cot\frac{\alpha}{2}\right)\mathbf{L}(1)\,\mathbf{F}(2+\sin\alpha)\,\mathbf{L}(1)\mathbf{F}\left(1+\cot\frac{\alpha}{2}\right),\ \ 0<\alpha<\frac{3\pi}{2}, \quad (4.40)$$

and

$$\mathbf{J}_0(\alpha) = \mathbf{F}\left(-\tan\frac{\alpha}{2}\right)\mathbf{L}\left(\frac{-1}{\sin\alpha}\right)\mathbf{F}\left(-\tan\frac{\alpha}{2}\right),\ \ \pi<\alpha<2\pi. \quad (4.41)$$

In words, $\mathbf{J}_0(\alpha)$ requires no more than two convex lenses for its realization. Note that $\mathbf{J}_0(0)$ can be realized as in Eq. (4.9). Now when $\pi < (\beta-\alpha) < 2\pi$, $\mathbf{D}_{\alpha,\beta}$ can be decomposed as

$$\mathbf{D}_{\alpha,\beta} = \mathbf{J}_0(\alpha+\pi)\begin{bmatrix} F(d) & 0 \\ 0 & R_{\beta-\alpha}\end{bmatrix}\begin{bmatrix} -F(-d) & 0 \\ 0 & -\mathbb{1}\end{bmatrix}. \quad (4.42)$$

Similarly, when $0 < (\beta-\alpha) < \pi$, $\mathbf{D}_{\alpha,\beta}$ can be decomposed as

$$\mathbf{D}_{\alpha,\beta} = \mathbf{J}_0(\beta+\pi)\begin{bmatrix} R_{\alpha-\beta} & 0 \\ 0 & F(d)\end{bmatrix}\begin{bmatrix} -\mathbb{1} & 0 \\ 0 & -F(-d)\end{bmatrix}. \quad (4.43)$$

Since $\mathbf{J}_0(\cdot)$ consumes no more than two convex lenses and $F(d)\oplus R_{\beta-\alpha}$ ($R_{\alpha-\beta}\oplus F(d)$) consumes no more than one cylindrical lens of positive focal length (see Eq. (4.41)) and $-F(-d)\oplus -\mathbb{1}$ ($-\mathbb{1}\oplus -F(-d)$) is realized as illustrated in Eq. (4.29) consuming four cylindrical lenses of positive focal length, $\mathbf{D}_{\alpha,\beta}$ requires not more than five cylindrical lenses of positive focal length and two convex lenses to realize. Note that in Eqs. (4.42) and (4.43), d is the total distance required to realize $R_{\beta-\alpha}$ ($R_{\alpha-\beta}$). As a special case of $\mathbf{D}_{\alpha,\beta}$, we have $\mathbf{J}_1(\theta) = \mathbf{D}_{\alpha,-\alpha}$ (see Eq. (4.18)). By Eqs. (4.42) and (4.43), $\mathbf{J}_1(\alpha)$ can be decomposed in the following two ways, i.e.,

$$\mathbf{J}_1(\alpha) = \mathbf{J}_0(\pi+\alpha)\,\mathbf{J}_{1a}(\alpha),\ \text{ and} \quad (4.44)$$

$$\mathbf{J}_1(\alpha) = \mathbf{J}_0(\pi-\alpha)\,\mathbf{J}_{1b}(\alpha), \quad (4.45)$$

with

$$\mathbf{J}_{1a}(\alpha) \equiv \begin{bmatrix} F(d) & 0 \\ 0 & R_{-2\alpha}\end{bmatrix}\begin{bmatrix} -F(-d) & 0 \\ 0 & -\mathbb{1}\end{bmatrix}, \quad (4.46)$$

$$\mathbf{J}_{1b}(\alpha) \equiv \begin{bmatrix} R_{2\alpha} & 0 \\ 0 & F(d) \end{bmatrix} \begin{bmatrix} -\mathbb{1} & 0 \\ 0 & -F(-d) \end{bmatrix}. \tag{4.47}$$

Note that rewriting $\mathbf{J}_1(\alpha)$ in the product form as in Eqs. (4.44) and (4.45) has the following advantage. For instance, any $\mathbf{R}$ written as in Eq. (4.22) with $j = 3$ and $k = 1$, the $\mathbf{J}_0(\cdot)$ part of $\mathbf{J}_k(\gamma)$ is readily absorbed into $\mathbf{J}_0(\alpha)$. In other words, $\mathbf{J}_1(\alpha)$ is essentially realized as $\mathbf{J}_{1a}(\alpha)$ or $\mathbf{J}_{1b}(\alpha)$, and this will be put to use in the following Section.

Having obtained the decompositions for the above listed specific examples, we now state a general decomposition for symplectic matrix $\mathbf{S}$ of the form $S_1 \oplus S_2$.

4.4.9 Theorem 1 :

Let $\mathbf{S} = S_1 \oplus S_2$, where $S_1,\ S_2 \in Sp_2(\mathbb{R})$. Then $\mathbf{S}$ can be realized using not more than three convex lenses and seven cylindrical lenses of positive focal length.

Proof : It is readily seen that any $\mathbf{S} = S_1 \oplus S_2$ can be written as

$$\mathbf{S} = \begin{bmatrix} -S_1 & 0 \\ 0 & -S_1 \end{bmatrix} \begin{bmatrix} -F(-d) & 0 \\ 0 & -\mathbb{1} \end{bmatrix} \begin{bmatrix} F(d) & 0 \\ 0 & S_1^{-1}S_2 \end{bmatrix}. \tag{4.48}$$

Here $-S_1 \oplus -S_1$ can be realized using a maximum of three convex lenses as seen in Ref. [95]. Further, $F(d) \oplus S_1^{-1}S_2$ is realized three cylindrical lenses of positive focal length as outlined in Ref. [95] with d being the total distance required to realize the two dimensional symplectic matrix $S_1^{-1}S_2$. Finally $-F(-d) \oplus -\mathbb{1}$ is realized as in Eq. (4.29), consuming four cylindrical lenses of positive focal length. Thus any $\mathbf{S}$ of the form $S_1 \oplus S_2$ is realized by using no more than three convex lenses and seven cylindrical lenses of positive focal length. In passing, note that when $S_2 = \mathbb{1}$,

$$\begin{bmatrix} S_1 & 0 \\ 0 & \mathbb{1} \end{bmatrix} = \begin{bmatrix} S_1 & 0 \\ 0 & F(d) \end{bmatrix} \begin{bmatrix} \mathbb{1} & 0 \\ 0 & F(-d) \end{bmatrix}. \tag{4.49}$$

Since $S_1 \oplus F(d)$ consumes three cylindrical lenses of positive focal length with d being the total distance required to realize S_1, and $\mathbb{1} \oplus F(-d)$ (as realized in Eq. (4.31)) consumes four cylindrical lenses of positive focal length and two convex lenses, any symplectic matrix $\mathbf{S}$ of the form $S_1 \oplus \mathbb{1}$ can be realized by no more than two convex lenses and seven cylindrical lenses of positive focal length.

4.5 Realization of 4-dimensional symplectic matrix

Having obtained the decompositions of symplectic matrices of the form $S_1 \oplus S_2$ in the previous Section, we now consider symplectic matrices which are not of the direct sum form. We begin with the realization of $\mathbf{J}_3(\alpha)$ (see Eq. (4.20)) using the method outlined in Ref. [96]. Recall that the image reflector $\mathbf{I}_y$ (Eq. (4.38)) performs a reflection in the y coordinate. The symplectic matrix corresponding to a rotated reflector, rotated by an angle $\alpha/2$ with respect to the y coordinate is given by

$$\mathbf{I}_{\alpha/2} = \mathbf{J}_3(\alpha/2)\,\mathbf{I}_y\,\mathbf{J}_3(-\alpha/2) = \begin{bmatrix} \cos\alpha\,\mathbb{1} & \sin\alpha\,\mathbb{1} \\ \sin\alpha\,\mathbb{1} & -\cos\alpha\,\mathbb{1} \end{bmatrix}. \tag{4.50}$$

Here we have used the fact that $\mathbf{J}_3(\cdot)$ generates spatial rotation in the x–y plane [128]. With this, $\mathbf{J}_3(\alpha)$ is realized as

$$\mathbf{J}_3(\alpha) = \mathbf{I}_{\alpha/2}\,\mathbf{I}_y. \tag{4.51}$$

Clearly, in realizing $\mathbf{J}_3(\alpha)$ we have made use of ten cylindrical lenses of positive focal length. Finally the cross gyrator $\mathbf{J}_2(\alpha)$ (see Eq. (4.19)) can be realized as

$$\mathbf{J}_2(\alpha) = \tilde{\mathbf{P}}_y(1)\,\mathbf{I}_{\alpha/2}\,\tilde{\mathbf{P}}_y(1). \tag{4.52}$$

It is evident by Eqs. (4.36) and (4.50) that $\mathbf{J}_2(\alpha)$ requires eleven cylindrical lenses of positive focal length to realize.

We now move on to the realization of the symplectic matrix $\mathbf{S}$ as in Eq. (4.11). While decompositions for $\mathbf{M}$, $\mathbf{J}_0$, $\mathbf{J}_1$, $\mathbf{J}_2$, and $\mathbf{J}_3$ have been obtained in Eqs. (4.39), (4.40) and (4.41), (4.44)-(4.47), (4.52), and (4.51) respectively, further simplification is possible in realizing $\mathbf{S}$ in its composite form as in Eq. (4.11). In particular, $\mathbf{R}$ (see Eq. (4.22)) can be written as

$$\mathbf{R} = \mathbf{J}_0(\alpha)\,\mathbf{J}_3(\beta)\,\mathbf{J}_1(\gamma)\,\mathbf{J}_3(\delta), \tag{4.53}$$

with the choice $j = 3$ and $k = 1$. The above choice has been made for the following reasons. First, $\mathbf{J}_3(\cdot)$ is a spatial rotation in the x–y plane. Second, in realizing $\mathbf{J}_1(\cdot)$ we consume lesser number of lenses as opposed to realizing $\mathbf{J}_2(\cdot)$, as evident from Eqs. (4.44)-

(4.47) and (4.52). Now $\mathbf{R}$ of Eq. (4.53) can be rewritten as

$$\begin{aligned}\mathbf{R} &= \mathbf{J}_3(\beta)\,\mathbf{J}_0(\alpha \pm \gamma + \pi)\,\mathbf{J}_{1a/b}(\gamma)\,\mathbf{J}_3(\delta) \\ &= \mathbf{J}_3(\beta+\delta)\,\mathbf{J}_0(\alpha \pm \gamma + \pi)\,\mathbf{J}'_{1a/b}(\gamma), \end{aligned} \tag{4.54}$$

where $\mathbf{J}_{1a/b}(\gamma)$ are as in Eqs. (4.46) and (4.47) and $\mathbf{J}'_{1a/b}(\gamma)$ is $\mathbf{J}_{1a/b}(\gamma)$ rotated by an amount $-\delta$ in the x–y plane. Note that when $0 \le \gamma \le \pi/2$ ($\pi \le \gamma \le 3\pi/2$), $\mathbf{R}$ of Eq. (4.54) is realized using $\mathbf{J}_{1a}(\gamma)$ ($\mathbf{J}_{1b}(\gamma)$) of Eq. (4.46) (Eq. (4.47)). When $\gamma = 0$ or π, $\mathbf{J}_1(\gamma) = \mathbb{1}$ or $-\mathbb{1}$ respectively and hence $\mathbf{R}$ is $\mathbf{J}_3(\beta+\delta)\,\mathbf{J}_0(\alpha \pm \gamma + \pi)$ or $\mathbf{J}_3(\beta+\delta)\,\mathbf{J}_0(\alpha \pm \gamma)$. With these observations, $\mathbf{S}$ of Eq. (4.11) is decomposed as

$$\begin{aligned}\mathbf{S} &= \mathbf{J}_3(\beta_1+\delta_1)\,\mathbf{J}_0(\alpha_1 \pm \gamma_1 + \pi)\,\mathbf{J}'_{1a/b}(\gamma_1)\,\mathbf{M} \\ &\quad \times \mathbf{J}'_{1a/b}(-\gamma_2)\,\mathbf{J}_0(-\alpha_2 \mp \gamma_2 + \pi)\,\mathbf{J}_3(-\beta_2-\delta_2) \qquad (4.55) \\ &= \mathbf{J}_3(\phi)\,\mathbf{K}', \qquad (4.56)\end{aligned}$$

where $\alpha_3 = \beta_1 + \delta_1 - \beta_2 - \delta_2$ and

$$\begin{aligned}\mathbf{K}' &= \mathbf{J}_3(\beta_2+\delta_2)\,\mathbf{K}\,\mathbf{J}_3(-\beta_2-\delta_2), \quad \text{with} \\ \mathbf{K} &= \mathbf{J}_0(\alpha_1 \pm \gamma_1 + \pi)\,\mathbf{J}'_{1a/b}(\gamma_1)\,\mathbf{M}\,\mathbf{J}'_{1a/b}(-\gamma_2)\,\mathbf{J}_0(-\alpha_2 \mp \gamma_2 + \pi). \end{aligned} \tag{4.57}$$

That is, $\mathbf{K}'$ is $\mathbf{K}$ rotated in the x–y plane at an angle $\beta_2 + \delta_2$. Since $0 \le \beta_1, \beta_2, \delta_1, \delta_2 < \pi$, $0 \le \beta_2 + \delta_2 < 2\pi$, and $0 \le \alpha_3 < 2\pi$. Thus, in realizing $\mathbf{S}$, apart from the transverse plane rotation given by $\mathbf{J}_3(\alpha_3)$, $\mathbf{S}$ is essentially $\mathbf{K}'$, i.e., rotated $\mathbf{K}$. In other words, by orienting the output x'–y' plane at an angle $-\alpha_3$ with respect to the x–y plane, any $\mathbf{S}$ is realized as a rotated $\mathbf{K}$. Further note that if any one of the angles $\alpha_1 \pm \gamma_1 + \pi$ or $-\alpha_2 \mp \gamma_2 + \pi$ of $\mathbf{J}_0(\cdot)$ lie between 0 and π, then they may be replaced respectively with $\alpha_1 \pm \gamma_1$ or $-\alpha_2 \mp \gamma_2$ so that the $\mathbf{J}_0(\cdot)$ in Eq. (4.57) is realized using one convex lens. And the remaining factor $-\mathbb{1}$ can be absorbed into $\mathbf{J}_3(\alpha_3)$, i.e., α_3 is replaced with $\alpha_3 + \pi$. On the other hand, if both of the angles $\alpha_1 \pm \gamma_1 + \pi$ and $-\alpha_2 \mp \gamma_2 + \pi$ lie between 0 and π, they are both respectively replaced with $\alpha_1 \pm \gamma_1$ and $-\alpha_2 \mp \gamma_2$ so that the $\mathbf{J}_0(\cdot)$ in Eq. (4.57) is again realized using one convex lens. We thus have

4.5.1 Theorem 2 :

Any $\mathbf{S} \in Sp(4, \mathbb{R})$ can be realized using not more than four convex lenses and fourteen cylindrical lenses of positive focal length.

Proof : In realizing $\mathbf{K}$ of Eq. (4.57), $\mathbf{J}_0(\cdot)$ (Eq. (4.41)) consumes one convex lens, $\mathbf{J}'_{1a/b}(\cdot)$ (Eqs. (4.46) and (4.47)) consumes five cylindrical lenses of positive focal length, and $\mathbf{M}$ (Eq. (4.39)) consumes two convex lenses and four cylindrical lenses of positive focal length.

The following observation can be made in regard of Theorem 2. While it is possible to realize any $\mathbf{S} \in Sp(4, \mathbb{R})$ using thin lenses of positive focal length alone, it is impossible to realize the same using thin lenses of negative focal length alone as indicated in Ref. [95].

4.6 Concluding remarks

To conclude, we have provided an explicit decomposition of a general FOOS in terms of free propagation, convex lenses, and cylindrical lenses of positive focal length. We have also obtained a decomposition of FOOS corresponding to symplectic matrices of the form $\mathbf{S} = S_1 \oplus S_2$, where $S_1,\ S_2 \in Sp(2, \mathbb{R})$. Decompositions for specific examples such as differential free and inverse free propagation, differential magnifiers, and differential fractional Fourier transform have been obtained. Moreover, the present work is relevant to situations where LCTs are used. For instance, in time evolution of a quantum mechanical system (in two variables) through a quadratic Hamiltonian [114, 113], the present decomposition will realize the same as a sequence of free particle time evolutions and instantaneous harmonic impulses of positive signature in the x and y variables. Given that notions such as entanglement in classical optics [156, 157, 158] is being actively pursued in recent literature, we believe the results presented here is definitely relevant to engineering paraxial light fields with desired properties [159, 160, 161, 162, 163]. In addition, the results are also relevant to signal processing applications that make use of LCTs [116, 122, 123, 164].

Chapter 5

Estimation of phases with dislocations in paraxial wave fields from intensity measurements

5.1 Introduction

In Section 3.7 we briefly reviewed GS algorithm and similar algorithms proposed by introducing various constraints to the GS algorithm. These algorithms generally make use of unitary transformations such as Fourier transform and free propagation which conserve the OAM of the wave field. Say we are given two intensity patterns corresponding to an LG mode, $\psi_p^l(r,\theta;z)$ (Eq. (2.51)) and $\mathcal{U}\,\psi_p^l(r,\theta;z)$, where $\mathcal{U}$ is a unitary transformation (such as Fourier transform or free propagation) which conserves OAM of the wave field. Then the retrieved phase using GS algorithm can belong to one of the LG modes $\psi_p^l(r,\theta;z)$ or $\psi_p^{-l}(r,\theta;z)$, as both have the same intensity pattern. In other words, the retrieved phase can be ambiguous up to a clockwise or anti-clockwise orientation and is hard to overcome. For instance, as mentioned in Section 1.1, even after imposing several constraints, convergence was achieved only after 939 iterations in Ref. [75] and in some cases it required 10,000 iterations (see Ref. [11]).

This ambiguity can be overcome if the unitary transformation $\mathcal{U}$ can give two different intensity patterns for the LG modes $\psi_p^l(r,\theta;z)$ and $\psi_p^{-l}(r,\theta;z)$. One simple transformation which meets this requirement is PFT (see Eq. (4.34), and Figure 4.12). That is, PFT does not typically conserve the OAM of the wave field, and the intensities of the wave fields $\mathcal{U}\psi_p^l(r,\theta;z)$ and $\mathcal{U}\psi_p^{-l}(r,\theta;z)$, where $\mathcal{U}$ is PFT, are not the same. Also, we capture intensity from three transverse planes, where the wave fields at first and transverse plane are

related by PFT and those at second and third are related by free propagation. The reasons for three plane intensity measurements are (i) availability of more information and (ii) satisfying more constraints. So the iterative algorithm can be expected to give a deterministic phase [63]. Motivated by these reasons, we propose an iterative algorithm and numerically demonstrate it to retrieve phases with dislocations through three transverse plane intensity measurements using PFT and free propagation and hence can measure the OAM of the wave field.

5.2 Fourier/partial Fourier transformation and OAM

A paraxial coherent wave field propagating along the z–direction can be represented as $\psi(x, y; z)\ \exp\left[i(\kappa z - \omega t)\right]$, where

$$\psi(x, y; z) = A(x, y; z)\ \exp\left[i\phi(x, y; z)\right]. \tag{5.1}$$

Here $A(x, y; z)$ and $\phi(x, y; z)$ are the amplitude and the phase of the wave field in the x–y plane at a given z coordinate [76].

A well known example of a paraxial coherent wave field is the LG mode (see Eq. (2.51)). Given $\psi(x, y; z)$, the intrinsic longitudinal OAM ($\bar{\mathsf{L}}_z^{\text{int}}$) as evaluated on $\psi(x, y; z)$ at a particular z coordinate is given by Eq. (2.136). It is readily seen that τ (see Eq. (2.137)) as evaluated on an LG mode as in Eq. (2.51) with mode numbers l and p is l. In this sense, τ captures the amount of phase dislocation as available in the phase of $\psi_p^l(r, \theta; z)$ (see Eq. (2.51)), and the LG mode possesses longitudinal OAM.

Now suppose $\psi(x, y; z)$ as in Eq. (5.1) undergoes two dimensional Fourier transformation [108], i.e., $\psi(x, y; z) \rightarrow \tilde{\psi}(\tilde{x}, \tilde{y}; z)$, where

$$\tilde{\psi}(\tilde{x}, \tilde{y}; z) = \frac{-i\kappa}{2\pi d} \int_{-\infty}^{\infty}\int_{-\infty}^{\infty} \exp\left[\frac{-i\kappa}{d}(x\tilde{x} + y\tilde{y})\right] \psi(x, y; z)\, \mathrm{d}x\, \mathrm{d}y. \tag{5.2}$$

Eq. (5.2) is realized as in Figure 4.1, where the wave field $\psi(x, y; z)$ is incident at the input plane, and its Fourier transformation $\tilde{\psi}(\tilde{x}, \tilde{y}; z)$ is obtained at the output plane. It is then readily verified that the operator array

$$\hat{\xi}' = [\Delta\hat{x},\ \Delta\hat{p}_x,\ \Delta\hat{y},\ \Delta\hat{p}_y]^T \rightarrow \mathbf{S}\,\hat{\xi}', \tag{5.3}$$

where

$$\mathbf{S} = \sigma_d \oplus \sigma_d, \tag{5.4}$$

with σ_d being the ray transfer matrix associated with the Fourier transform (see Eq. (4.1)). By Eq. (5.4), it is clear that $\bar{\mathsf{L}}_z^{\text{int}}$ of Eq. (2.136) is invariant on Fourier transformation of the wave field. For example, for $\psi_p^{\pm l}(r, \theta; z)$ of Eq. (2.51) at $z = 0$ (waist plane), the Fourier transform is given by

$$\begin{aligned}\frac{-i\kappa}{2\pi d} \int_{-\infty}^{\infty}\int_{-\infty}^{\infty} e^{\frac{-i\kappa}{d}(x\tilde{x}+y\tilde{y})} \psi_p^{\pm l}(r, \theta; 0)\, \mathrm{d}x\, \mathrm{d}y &= \frac{\kappa\, w(0)}{d\sqrt{2\pi}} \left[\frac{p!}{(p+|l|)!}\right]^{\frac{1}{2}} (-i)^{|l|+2p+1} \\ &\times L_p^{|l|}\left(\frac{\kappa^2\, w(0)^2\, \tilde{r}^2}{2d^2}\right) \left[\frac{\kappa\, w(0)\, \tilde{r}}{d\sqrt{2}}\right]^{|l|} \\ &\times \exp\left(\frac{-\kappa^2\, w(0)^2\, \tilde{r}^2}{4d^2}\right) \exp\left(\pm il\tilde{\theta}\right), \end{aligned} \tag{5.5}$$

where $\tilde{r} = \sqrt{\tilde{x}^2 + \tilde{y}^2}$ and $\tilde{\theta} = \tan^{-1}(\tilde{y}/\tilde{x})$. Clearly, Fourier transformation conserves the phase dislocation.

Suppose $\psi(x, y; z)$ undergoes partial Fourier transformation, say in y coordinate, i.e., $\psi(x, y; z) \to \tilde{\psi}(x, \tilde{y}; z)$, where

$$\tilde{\psi}(x, \tilde{y}; z) = \sqrt{\frac{\kappa}{i2\pi d}} \int_{-\infty}^{\infty} \exp\left(\frac{-i\kappa}{d}\, y\tilde{y}\right) \psi(x, y; z)\, \mathrm{d}y. \tag{5.6}$$

We now note that Eq. (5.6) is realized as in Figure 4.12, where the wave field $\psi(x, y; z)$ is incident at the input plane, and its partial Fourier transformation $\tilde{\psi}(x, \tilde{y}; z)$ is obtained at the output plane. Then,

$$\hat{\xi} = [\Delta\hat{x},\ \Delta\hat{p}_x,\ \Delta\hat{y},\ \Delta\hat{p}_y]^T \to \mathbf{P}_y(d)\, \hat{\xi}, \tag{5.7}$$

where

$$\mathbf{P}_y(d) = \mathbb{1} \oplus \sigma_d, \tag{5.8}$$

i.e., we have performed identity transformation in x coordinate and Fourier transformation in y coordinate (see Eq. (4.33)). To this end, we have the following observation. Referring

to Figure 4.12, we see that the lenses L1, L2, and L4 act only on the x coordinate, lens L3 acts only on the y coordinate, and free propagation acts symmetrically on both coordinates, the above configuration realizes identity transformation on the x coordinate while simultaneously realizing Fourier transformation on the y coordinate (see Eqs. (5.6), (5.8), and (4.34)).

It is readily verified that under partial Fourier transform of the wave field,

$$\bar{\mathsf{L}}_z^{\text{int}} \rightarrow \bar{\mathsf{L}}_z'^{\text{int}} = -\omega\,\varepsilon_0\,\kappa\left\langle\left(\frac{\Delta\hat{x}\,\Delta\hat{y}}{d} + d\,\Delta\hat{p}_x\,\Delta\hat{p}_y\right)\right\rangle, \text{ and} \tag{5.9}$$

$$\bar{\mathsf{L}}_z^{\text{int}} \neq \bar{\mathsf{L}}_z'^{\text{int}} \tag{5.10}$$

for a generic paraxial wave field. For example, for $\psi_p^{\pm l}(r,\theta;z)$ of Eq. (2.51) at $z=0$ (waist plane), the partial Fourier transform is given by

$$\sqrt{\frac{\kappa}{i2\pi d}}\int_{-\infty}^{\infty} e^{\frac{-i\kappa}{d}(y\tilde{y})}\psi_p^{\pm l}(r,\theta;0)\,\mathrm{d}y = \sqrt{\frac{\kappa}{i\pi d}}\frac{(-1)^p\,2^{-p-\frac{|l|}{2}}}{\sqrt{p!(p+|l|)!}}\exp\left[-\frac{x^2}{w^2(0)} - \frac{\kappa^2 w^2(0)\tilde{y}^2}{4d^2}\right] \times H_{p+l}\left(\frac{x}{w(0)} \pm \frac{\kappa w(0)\tilde{y}}{2d}\right)H_p\left(\frac{x}{w(0)} \mp \frac{\kappa w(0)\tilde{y}}{2d}\right). \tag{5.11}$$

Here $H_p(\cdot)$ is the Hermite polynomial with index p. Clearly, partial Fourier transformation not only creates/destroys phase dislocations but also distinguishes their orientation, as seen in Eq. (5.11). That is, on applying the partial Fourier transformation to the wave fields $\psi_p^l(r,\theta;z)$ and $\psi_p^{-l}(r,\theta;z)$ (Eq. (2.51)), we obtain two different intensity patterns. Clearly this feature is absent in Eq. (5.5), i.e., both the wave fields $\psi_p^l(r,\theta;z)$ and $\psi_p^{-l}(r,\theta;z)$ yield the same intensity pattern on application of Fourier transformation.

While it is well known that Fourier transform in Eq. (5.2) is readily realized in lab using a thin convex lens of focal length d and $\mathbf{S}$ of Eq. (5.4) is its corresponding ray transfer matrix [108], the realization of partial Fourier transform as in Eq. (5.6) whose ray transfer matrix is given by $\mathbf{P}_y(d)$ of Eq. (5.8) has been obtained only recently [96]. To reproduce the results obtained in Section 4.4, partial Fourier transform can be realized in terms of free propagation and thin cylindrical lenses. That is, $\mathbf{P}_y(d)$ can be realized as (schematically outlined in Figure 4.12) given in Eq. (4.34). Here $d > 0$ implies that the lens is convex. Two remarks are in order in regard of the realization outlined in Fig 4.12 (equivalently Eq. (4.34)) : First, this lens arrangement realizes partial Fourier transform on any paraxial wave field irrespective of its width. Second, through use of cylindrical lenses of focal

lengths $f_x = 2d/9$ and $f_y = d$ as shown in Figure 4.12, the total distance required to realize partial Fourier transformation is $2d$ units.

5.3 Proposed algorithm and numerical demonstration

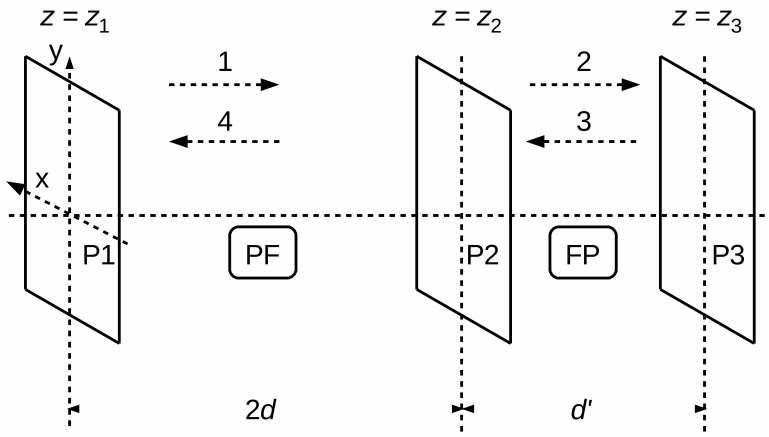

Figure 5.1: Schematic of the proposed algorithm. The wave field $\psi(x, y; z_1)$ at plane P1 is partial Fourier transformed by the lens assembly as shown in Figure 4.12 at plane P2 (shown by arrow-1). At P2, the amplitude of the wave field is replaced with $A(x, y; z_2)$. The resulting field $\psi(x, y; z_2)$ is free propagated through a distance d' to plane P3 (shown by arrow-2) and the amplitude of the resultant wave field is replaced with $A(x, y; z_3)$ to obtain $\psi(x, y; z_3)$. In the reverse direction, $\psi(x, y; z_3)$ is inverse free propagated through a distance d' to P2 (shown by arrow-3), where the resulting amplitude is replaced with $A(x, y; z_2)$. Finally this field is inverse partial Fourier transformed from P2 to P1 (shown by arrow-4) and the resulting amplitude is replaced with $A(x, y; z_1)$. This procedure is now iterated for n times.

Now for the implementation of the algorithm, since the partial Fourier transform relation in Eq. (5.6) consults only the y coordinate, any $\psi(x, y; z)$ replaced with $\psi(x, y; z)$ $\times \exp[i\phi(x)]$ with $\phi(x)$ being an arbitrary function, results in the same pair of intensities in both input and output planes. However, $\psi(x, y; z)$ and $\psi(x, y; z) \exp[i\phi(x)]$, on free propagation, need not result in same pair of intensities. Further, given that there is more information in three plane intensities than two plane intensities [63], the proposed algorithm makes use of three plane intensity measurements as follows.

Consider three transverse planes P1, P2, and P3 at the z coordinates z_1, z_2, and z_3 such that the wave field $\psi(x, y; z_2) = A(x, y; z_2) \exp[i\phi(x, y; z_2)]$ at P2 is the partial

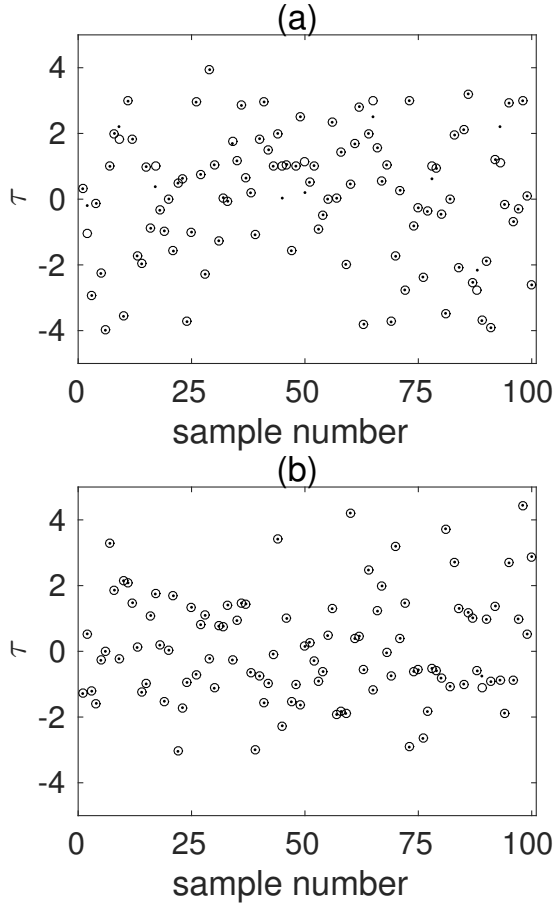

Figure 5.2: Frame (a) plots the values of τ (see (2.137)) for each of the two mode superposition samples considered in the second numerical experiment, and frame (b) plots the values of τ for each of the three mode superposition samples considered in the third numerical experiment. In both the frames, the horizontal axis enumerates the sample number. In both the frames, '$\circ$' plots the value of τ for the input sample LG superposition considered at plane P1 (see Figure 5.1), and '$\cdot$' plots the value of τ obtained on the wave field at P1 after 100 iterations of the algorithm, for the same sample. In frame (a), '$\circ$' and '$\cdot$' 'coincided' for 91 of the 100 samples considered, and in frame (b), '$\circ$' and '$\cdot$' 'coincided' for 99 of the 100 considered samples, $C(2n)$ (see Eq. (5.12)) converged to 1 within $1\,\%$ error in less than 100 iterations for those samples (see also frames (a5) of Figure 5.3), (b5) of Figure 5.4), and (c5) of Figure 5.5).

Fourier transform of the field $\psi(x, y; z_1) = A(x, y; z_1) \exp[i\phi(x, y; z_1)]$ at P1, and field $\psi(x, y; z_3) = A(x, y; z_3) \exp[i\phi(x, y; z_3)]$ at P3 is the field $\psi(x, y; z_2) = A(x, y; z_2) \times \exp[i\phi(x, y; z_2)]$ at P2 free propagated through distance d' (see Figure5.1). Say we measure their corresponding intensities $I(x, y; z_1)$, $I(x, y; z_2)$, and $I(x, y; z_3)$ at these three planes. Now the phases $\phi(x, y; z_1)$, $\phi(x, y; z_2)$, and $\phi(x, y; z_3)$ of the wave field at these three planes P1, P2, and P3 is extracted through the knowledge of intensities $I(x, y; z_1)$, $I(x, y; z_2)$, and $I(x, y; z_3)$ as follows: We first start with the wave field $A(x, y; z_1) \times \exp[i\phi_1(x, y; z_1)]$ at plane P1, with $\phi_1(x, y; z_1)$ as the initial trial phase. This wave field is numerically partial Fourier transformed to obtain $\psi_1(x, y; z_2) = A_1(x, y; z_2) \exp[i\phi_1(x, y; z_2)]$ at plane P2. Now $A_1(x, y; z_2)$ is replaced with $A(x, y; z_2)$ at P2, and the resulting wave field is free propagated numerically through distance d' to obtain $\psi_1(x, y; z_3) = A_1(x, y; z_3) \times \exp[i\phi_1(x, y; z_3)]$ at plane P3. Then $A_1(x, y; z_3)$ is replaced with $A(x, y; z_3)$ at P3 and the resulting field is inverse free propagated numerically through a distance d' to plane P2 to obtain $\psi_2(x, y; z_2) = A_2(x, y; z_2) \exp[i\phi_2(x, y; z_2)]$. Finally $A_2(x, y; z_2)$ is replaced with $A(x, y; z_2)$ at P2 and the resultant field is inverse partial Fourier transformed numerically to obtain $\psi_2(x, y; z_1) = A_2(x, y; z_1) \exp[i\phi_2(x, y; z_1)]$ at P1. This process is repeated n times so that $\psi_{2n}(x, y; z_1) \approx \psi(x, y; z_1)$.

To numerically demonstrate the algorithm, a grid of size 512×512 was chosen. The length of the grid was chosen to be $\approx$ 6.769 mm, with $d \approx 14.14$ cm and $\lambda = 633$ nm. This ensured that the relation in Eq. (5.6) is realized numerically using the discrete Fourier transform in a direct manner.[1] LG modes and their superpositions were considered, with $w(0)$ varied randomly between 0.1 mm and 0.3 mm in an equi-probable manner by making use of the '`rand`' command in MATLAB. Such a superposition propagated through a distance of 1 mm is considered as being incident on P1, which on numerical partial Fourier transform results in the wave field P2, and which on further numerical free propagation results in the wave field at P3. White Gaussian noise of 10 dB is added to each of the corresponding three intensities at P1, P2, and P3. The resulting three intensities are then taken to be $I(x, y; z_1)$, $I(x, y; z_2)$, and $I(x, y; z_3)$ which are measured in an experiment. Choosing $w(0)$ in the range 0.1 mm through 0.3 mm ensured that the fields in P1, P2, and P3 are sufficiently well-sampled. The algorithm is executed numerically as outlined in the previous paragraph. In each of the studied examples, the initial trial phase was assumed to be zero. Further, to curtail the effects of the added noise, the considered intensities in the

[1] It is easy to see from Eq. (5.6) that the optical PFT is scaled by a factor κ/d. While implementing this numerically in a discrete manner (for the choice $N = 512$, $d = 14.14\,\mathrm{cm}$, and $\lambda = 633\,\mathrm{nm}$), the scaling factor can be chosen as unity if the length of the grid is 6.769 mm.

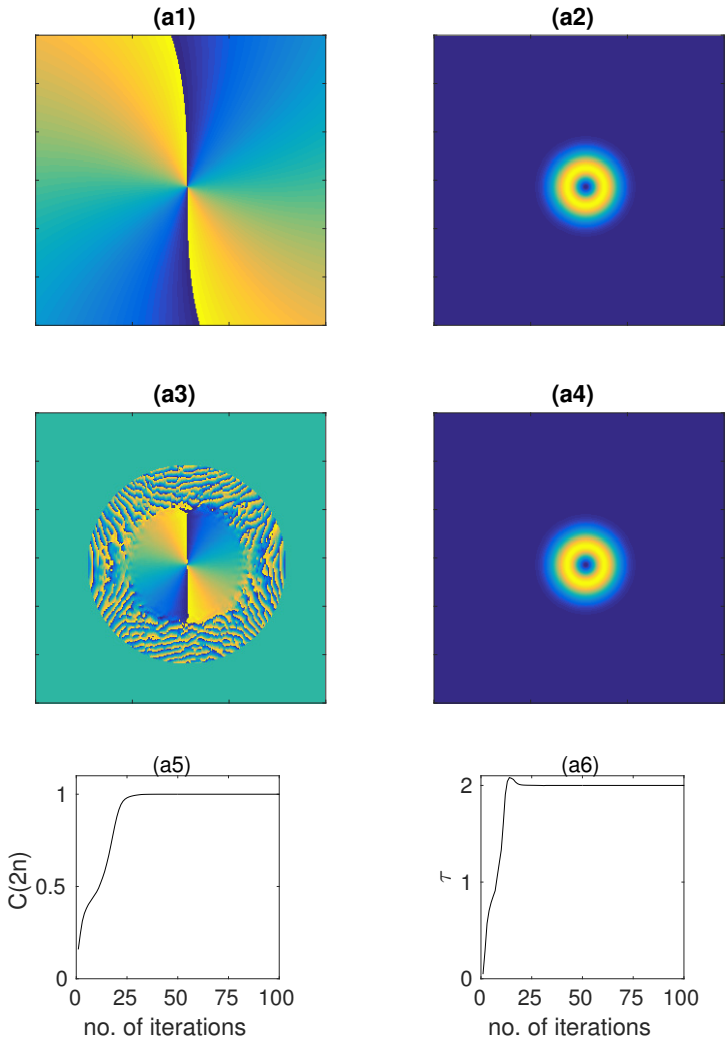

Figure 5.3: Frames (a1) and (a2) plot the input phase and amplitude of the LG beam with $(l, p) = (2, 0)$ and $w(0) = 0.2542$ mm. Frame (a3) plots the phase of the wave field at P1 after 100 iterations, and frame (a4) plots the amplitude after 100 iterations. Frame (a5) plots $C(2n)$ (Eq. (5.12)) versus iteration number n, and frame (a6) plots the twist parameter τ (Eq. 2.137) versus iteration number n, for the same example.

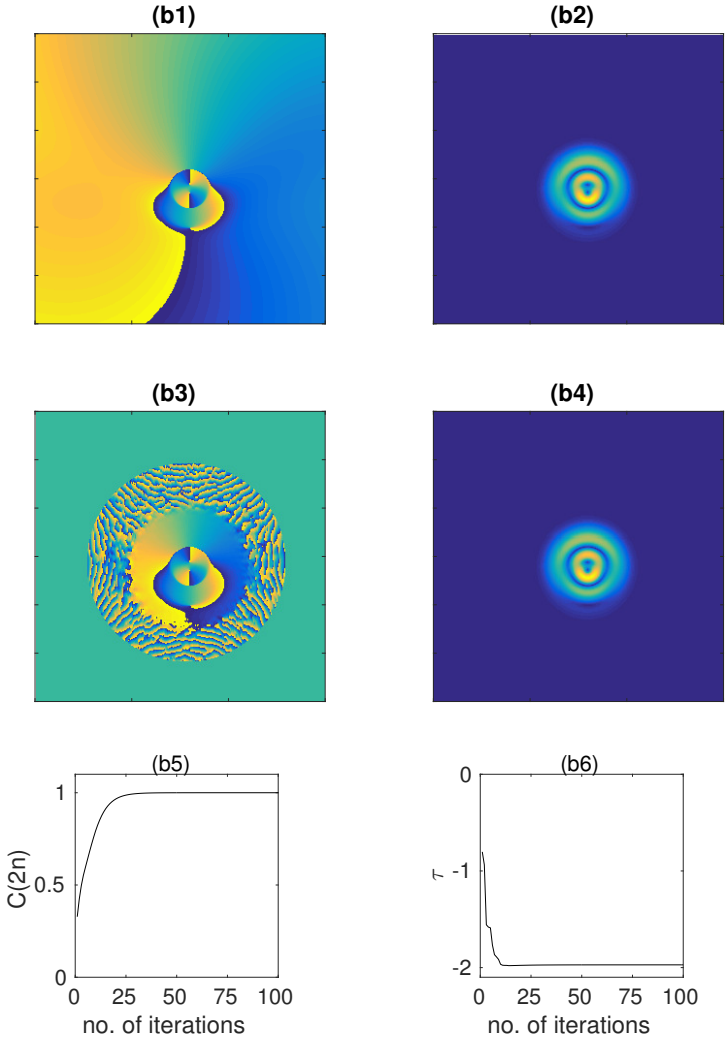

Figure 5.4: Frames (b1) and (b2) plot the input phase and amplitude of a two mode superposition with mode numbers $(l_1, p_1) = (-2, 1)$, $(l_2, p_2) = (-1, 2)$, coefficients $c_1 = 0.9314$, $c_2 = 0.0017 - 0.3639\,i$, with $\tau = -1.9716$ and $w(0) = 0.2204$ mm (second numerical experiment). Frame (b3) plots the phase of the wave field at P1 after 100 iterations, and frame (b4) plots the amplitude after 100 iterations. Frame (b5) plots $C(2n)$ versus iteration number n, and frame (b6) plots τ versus iteration number n, for the same example.

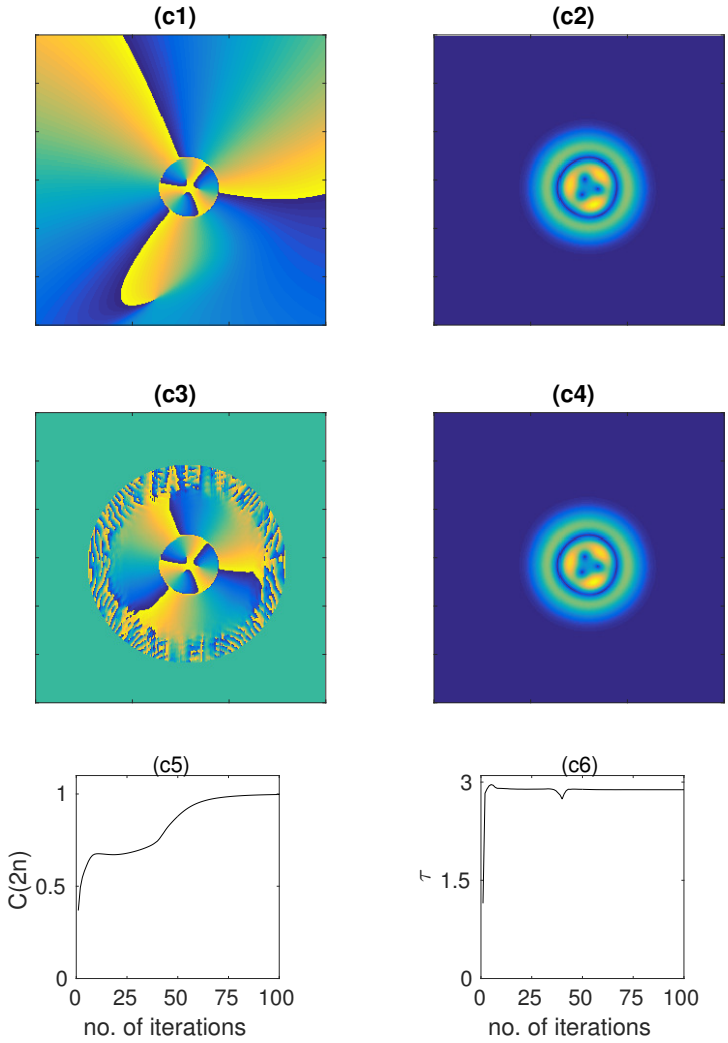

Figure 5.5: Frames (c1) and (c2) plot the input phase and amplitude of a three mode superposition with mode numbers $(l_1, p_1) = (0, 0)$, $(l_2, p_2) = (1, 2)$, $(l_3, p_3) = (3, 1)$, coefficients $c_1 = -0.1934$, $c_2 = -0.0506 - 0.0006\,i$, and $c_3 = 0.8539 - 0.4806\,i$, transverse shift of (5,4), (8,9), and (2,1) (in pixels) for the constituent modes, with $\tau = 2.8827$, and $w(0) = 0.2830$ mm (third numerical experiment). Frame (c3) plots the phase of the wave field at P1 after 100 iterations, and frame (c4) plots the amplitude after 100 iterations. Frame (c5) plots $C(2n)$ versus iteration number n, and frame (c6) plots τ versus iteration number n, for the same example.

three planes are as truncated [60] to a radius 100 pixels, i.e., ≈ 1.32 mm (see frames (a3) of Figure 5.3), (b3) of Figure 5.4), and (c3) of Figure 5.5). To test for convergence, the twist parameter τ was numerically evaluated on $\psi_{2n}(x, y; z_1)$, $\psi_{2n}(x, y; z_2)$, and $\psi_{2n}(x, y; z_3)$ compared with τ of $\psi(x, y; z_1)$, $\psi(x, y; z_2)$, and $\psi(x, y; z_3)$ at each iteration. Also the correlation $C(2n)$ between $\psi(x, y; z_i)$ and $\psi_{2n}(x, y; z_i)$ given by

$$C(2n) = \left| \int_{-\infty}^{\infty} \int_{-\infty}^{\infty} \psi_{2n}^{*}(x, y; z_i)\, \psi(x, y; z_i)\, \mathrm{d}x\, \mathrm{d}y \right| \tag{5.12}$$

was evaluated at each iteration in each of the respective planes. Here both $\psi_{2n}^{*}(x, y; z_i)$ and $\psi(x, y; z_i)$ are assumed to be normalized, i.e.,

$$\int_{-\infty}^{\infty} \int_{-\infty}^{\infty} \psi_{2n}^{*}(x, y; z_i)\, \psi_{2n}(x, y; z_i)\, \mathrm{d}x\, \mathrm{d}y = 1,$$

$$\text{and} \int_{-\infty}^{\infty} \int_{-\infty}^{\infty} \psi^{*}(x, y; z_i)\, \psi(x, y; z_i)\, \mathrm{d}x\, \mathrm{d}y = 1.$$

Clearly $0 \leq C(2n) \leq 1$, and the algorithm is said to have 'converged' when $C(2n) \approx 1$ after n iterations. The % error in convergence can be quantified as

$$\frac{[1 - C(2n)]}{C(2n)} \times 100.$$

For the purpose of illustration, three numerical experiments were performed. In the first numerical experiment, centered LG modes with $w(0) = 0.1687$ mm were considered, with $d' = d$. The index p was varied from 0 through 5 with index l going from $-p$ through $+p$ in each instance. It was found that $C(2n)$ converged to within 1% error in all the three planes in < 100 iterations, except for $l = \pm 1$ and $p = 0$. However, when d' was set to $1.5 \times d$, $C(2n)$ converged within 100 iterations for these two examples. As a variation of the experiment, $w(0)$ was varied randomly between 0.1 mm and 0.3 mm for the considered LG modes. It was again found that $C(2n)$ converged rapidly (see frames (a1)-(a6) of Figure 5.3).

In the second numerical experiment, two and three random complex linear superposi-

tions of centered LG modes such as :

$$\psi(r,\theta;z) = \sum_{j=1}^{m=2\text{ or }3} c_j\,\psi_{p_j}^{l_j}, \;\text{ with }\; \sum_{j=1}^{m} |c_j|^2 = 1, \tag{5.13}$$

were considered as being incident on P1, with $d' = d$ and $w(0)$ was varied randomly between 0.1 mm and 0.3 mm. The indices l_j and p_j ($0 \leq p_j \leq 5$ and corresponding l_j such that $-p_j \leq l_j \leq p_j$) were randomly chosen from those considered in the first numerical experiment by making use of '`rand`' command in MATLAB, in an equi-probable manner. When $m = 3$, the coefficients $\{c_1, c_2, c_3\}$ were chosen as

$$\begin{aligned} c_1 &= \exp(i\gamma_1)\,\cos\alpha, \\ c_2 &= \exp(i\gamma_2)\,\sin\alpha\,\cos\beta, \\ c_3 &= \exp(i\gamma_3)\,\sin\alpha\,\sin\beta, \end{aligned}$$

where $0 \leq \alpha \leq \pi$, and $0 \leq \beta, \gamma_1, \gamma_2, \gamma_3 < 2\pi$. The angles were chosen randomly in their respective intervals by making use of `rand` command in MATLAB. For $m = 2$, we let $\beta = 0$. The algorithm was tested on 100 such samples both for two and three superpositions and it was found that for more than 90 samples (see frame (a) of Figure 5.2), $C(2n)$ converged within 1% error in all the three planes within 100 iterations (see frames (b1)-(b6) of Figure 5.4). For the remaining samples, when d' was varied, rapid convergence was observed for particular choices of d'.

In the third numerical experiment, the considered superpositions were as in Eq. (5.13) of the second experiment, however, each mode in the superposition were randomly shifted in the transverse plane from the center in both x and y coordinates from 1 through 10 pixels in an equi-probable manner, with 100 samples each for two and three superpositions with mode numbers varied as in the previous experiment. Again, it was found that more than 90 samples (see frame (b) of Figure 5.2) converged within 100 iterations within 1% error in $C(2n)$ in all the three planes, for two and three superpositions (see frames (c1)-(c6) of Figure 5.5). For the remaining samples, rapid convergence was observed for appropriate choice of d'. It is useful to note that in all the studied numerical examples, τ was recovered unambiguously while the retrieved phase was ambiguous up to an overall shift.

For samples which didn't converge, we observed that while wave field correlation ($C(2n)$) between the input wave field and the obtained wave field after 100 iterations varied between

0 and 1, their respective intensity correlation varied between 0.8 and 1. This might be attributed to 'phase stagnation', where the algorithm is caught on a local minima (see, for instance, Refs. [60] and [61]). In our algorithm we have resolved this issue by varying d' (see Figure 5.1), and upon doing so we found that the algorithm converged.

5.4 Concluding remarks

To conclude, we have proposed and demonstrated an iterative algorithm to extract phases with dislocations from intensity measurements on paraxial wave fields. The algorithm makes use of partial Fourier transformation which does not conserve longitudinal OAM and can readily differentiate between two LG modes with opposite phase orientations, as opposed to Fourier transformation. As a result, phase is retrieved unambiguously even in the presence of white Gaussian noise in the transverse intensities. To test our claim, we have tested our algorithm on random complex linear superpositions of LG modes, and performed three numerical experiments, and found that the algorithm converges within 100 iterations for all the tested cases. Finally, the proposed method works well for wave fields with both integral and non-integral longitudinal OAM.

Chapter 6

Phase estimation using phase gradients obtained through Hilbert transform

6.1 Introduction

In Chapter 4 we proposed an iterative algorithm to retrieve phases with dislocations through three transverse plane intensity measurements and demonstrated it numerically using complex linear superpositions of LG modes. In this Chapter we propose a single-shot algorithm to extract phases from perturbed straight line fringes without phase unwrapping. We demonstrate our algorithm on numerically generated interferograms whose phases were random and generated using standard atmospheric turbulence models as well as experimentally on a Mach-Zehnder interferometric setup with a PRPP inserted in one of its arms. Throughout this Chapter we assume that phase encoded in these fringes do not possess any phase dislocations.

In Chapter 3 we discussed some widely used phase estimation methods in the literature to extract phase encoded in the interferogram(s). We now briefly review them. In interferometry based methods (see Figure 1.1), we discussed phase shifting interferometry in Section 3.2. Here, phase is extracted from N interferograms which are phase shifted versions of one another. This method can work for both straight line as well as closed fringes [5]. Another well known interferometry based method is Fourier fringe analysis (see Section 3.4) proposed in Ref. [15]. While this method requires single interferogram for phase retrieval (single-shot), it can only work for straight line fringes. Another alternate method proposed in Ref. [16] makes use of Hilbert transform (see Section 3.3). It can be noted that both methods presented in Refs. [15, 16] rely on assumptions that both background intensity and phase vary much slowly in compared with the tilt term. Further, the extracted phase through phase shifting as well as Fourier fringe analysis methods is in

wrapped form on account of the periodicity of $\tan^{-1}$ function and therefore needs unwrapping (see Section 3.5). In gradient based method, phase is reconstructed directly from its gradients, say, for instance, using the least square fit, and hence there is no necessity for phase unwrapping. It can be noted that these gradients can experimentally be measured from an incoming wave field directly using diffraction through Shack-Hartmann wavefront sensor (see Section 3.6).

In our algorithm, we retrieve the phase $\phi(x, y)$ from Eq. (1.1) in an unwrapped form. We first obtain $I_c(x, y)$ (Eq. 3.24) and $I_s(x, y)$ (Eq. 3.25) from $I(x, y)$ (Eq. 3.20). Now, instead of estimating $\phi(x, y)$ from Eq. (3.26) which requires unwrapping, we infer phase gradients in the present work from the interferogram, i.e., compute phase gradients with the knowledge of $I_c(x, y)$ and $I_s(x, y)$. In fact, such an exercise was carried out in the work of Refs. [18, 19], where phase gradients were extracted from the phase shifted interferograms, and then the phase was estimated from the phase gradients, without the requirement for phase unwrapping.

In the present work, the phase gradients are extracted from an interferogram using the Hilbert transform, and then the phase is extracted from the estimated gradients using the method of least squares for the Hudgin geometry [49, 45], well known in the context of wavefront sensors. As is evident, for the latter part, one needs to invert a matrix of size $N^2 \times N^2$, for a measured interferogram of matrix size $N \times N$ [45, 49]. Nevertheless, we exploit the symmetries available (see Section 6.3) in the Hudgin geometry matrix so as to handle the matrix inversion analytically, and the final result is obtained with only matrix multiplications and matrix sums of matrix size $N \times N$, in the extraction of the phase from its gradients. Note that for the latter part, one could also use the other geometries, already well established in the context of wavefront sensors [45, 48, 49, 47, 50, 51, 52].

6.2 Proposed algorithm

In this Section we outline the procedure in extracting the gradients of the phase from Eq. (1.1) using the Hilbert transform. For instance, $I_0(x, y)$ and $\eta(x, y)$ can be reasonably removed from $I(x, y)$ of Eq. (1.1) by Fourier transforming $I(x, y)$, and then filtering out the central peak, and the high frequencies, corresponding respectively to $I_0(x, y)$ and from $\eta(x, y)$, followed by inverse Fourier transformation. This will yield :

$$\mathsf{f} \equiv \mathsf{f}(x, y) \approx I_0 \cos\left[\varphi(x, y)\right]. \tag{6.1}$$

Now the Hilbert-transform [40, 42, 41, 43] of $\mathsf{f}(x,y)$ yields

$$\mathsf{g} \equiv \mathsf{g}(x,y) \approx I_0 \sin\left[\varphi(x,y)\right]. \tag{6.2}$$

With this, $I_0^2 \approx \mathsf{f}^2 + \mathsf{g}^2$, so that $\cos(\varphi(x,y)) \approx \mathsf{f}(x,y)/I_0$, and $\sin(\varphi(x,y)) \approx \mathsf{g}(x,y)/I_0$. It should be noted that the Hilbert-transform of $I_0 \cos\left[\varphi(x,y)\right]$ need not necessarily yield $I_0 \sin\left[\varphi(x,y)\right]$ [42, 40, 41]. However when $I_0(x,y)$ is slowly varying as compared with $\varphi(x,y)$, $\mathsf{g}(x,y)$ of Eq. (6.2) is the Hilbert-transform of $\mathsf{f}(x,y)$ of Eq. (6.1). Further, in Eqs. (6.1) and (6.2), we have neglected the remaining unfiltered noise contribution.

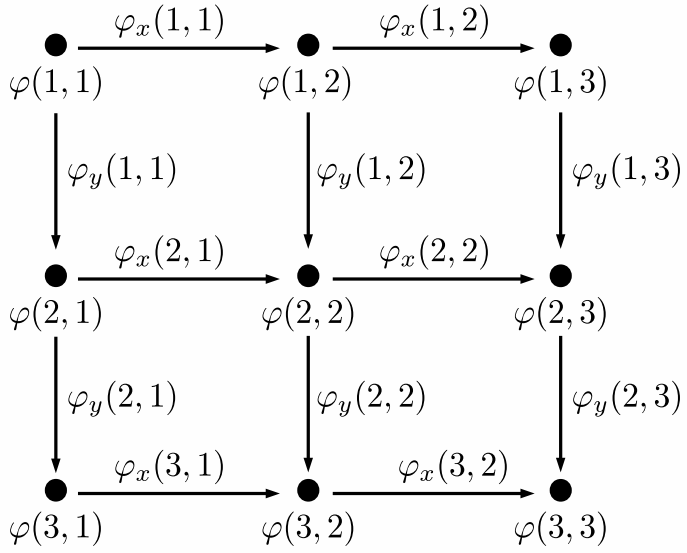

Figure 6.1: Shown here is an example to calculate the phase gradients $\varphi_x(j,k)$ and $\varphi_y(j,k)$ from the discrete phase matrix $\varphi(j,k)$ using the Hudgin geometry. Here, $\varphi_x(j,k) = \varphi(j,k) - \varphi(j,k+1)$ and $\varphi_y(j,k) = \varphi(j,k) - \varphi(j+1,k)$.

Now partial differentiating the $\mathsf{f}(x,y)$ and $\mathsf{g}(x,y)$ of Eqs. (6.1) and (6.2) with respect to x and y yields

$$\mathsf{f}_x \equiv \frac{\partial \mathsf{f}}{\partial x} \approx I_0 \sin\left[\kappa_x x + \kappa_y y - \phi(x,y)\right](\phi_x - \kappa_x), \tag{6.3}$$

$$\mathsf{f}_y \equiv \frac{\partial \mathsf{f}}{\partial y} \approx I_0 \sin\left[\kappa_x x + \kappa_y y - \phi(x,y)\right](\phi_y - \kappa_y), \tag{6.4}$$

$$\mathsf{g}_x \equiv \frac{\partial \mathsf{g}}{\partial x} \approx -I_0 \cos\left[\kappa_x x + \kappa_y y - \phi(x,y)\right](\phi_x - \kappa_x), \tag{6.5}$$

$$\mathsf{g}_y \equiv \frac{\partial \mathsf{g}}{\partial y} \approx -I_0 \cos\left[\kappa_x x + \kappa_y y - \phi(x,y)\right](\phi_y - \kappa_y), \tag{6.6}$$

where $\phi_x = \partial\phi/\partial x$ and $\phi_y = \partial\phi/\partial y$. Notice that the derivatives of I_0 with respect to both x and y are neglected with the assumption that I_0 is slowly varying. A little algebra using Eqs. (6.1)-(6.6) yields

$$\mathsf{f}_x^2 + \mathsf{g}_x^2 \approx I_0^2(\phi_x - \kappa_x)^2, \tag{6.7}$$

$$\mathsf{f}_y^2 + \mathsf{g}_y^2 \approx I_0^2(\phi_y - \kappa_y)^2. \tag{6.8}$$

Using Eqs. (6.7) and (6.8), we obtain

$$|\phi_x - \kappa_x| \approx \left(\frac{\mathsf{f}_x^2 + \mathsf{g}_x^2}{\mathsf{f}^2 + \mathsf{g}^2}\right)^{1/2}, \tag{6.9}$$

$$|\phi_y - \kappa_y| \approx \left(\frac{\mathsf{f}_y^2 + \mathsf{g}_y^2}{\mathsf{f}^2 + \mathsf{g}^2}\right)^{1/2}, \tag{6.10}$$

the modulus of the slopes. Note that the ratios in the RHS of Eqs. (6.9) and (6.10) are evaluated in a point wise manner. Now the signatures of the slopes $\varphi_x \equiv \phi_x - \kappa_x$ and $\varphi_y \equiv \phi_y - \kappa_y$ are fixed as follows : by Eq. (6.3), we have $\mathsf{f}_x = (I_0 \sin\varphi)(\phi_x - \kappa_x)$. Now dividing f_x by $I_0 \sin\varphi$ of Eq. (6.2) fixes the signature of $\phi_x - \kappa_x$. In the case when $\sin\varphi \to 0$, we divide $\mathsf{g}_x = -(I_0 \cos\varphi)(\phi_x - \kappa_x)$ (Eq. (6.5)) by $I_0 \cos\varphi$ of Eq. (6.1) to obtain the signature of $\phi_x - \kappa_x$ with an extra minus sign. Here we have used the fact that the functions $\sin\varphi$ and $\cos\varphi$ never approach zero simultaneously. In fact, in the numerical implementation, we use the former when $|\sin(\varphi)| > 1/\sqrt{2}$, and the latter when $|\sin(\varphi)| \leq 1/\sqrt{2}$, to fix the signature of φ_x. In a similar fashion the signature of φ_y is also fixed using Eqs. (6.1) and (6.2) in Eqs. (6.4) and (6.6). Now since the recorded interferogram is assumed to be a $N \times N$ matrix, the gradients are evaluated numerically using the above described procedure. Note that in discretizing Eqs. (6.1)-(6.10), the variables x and y are replaced with the discrete indices j and k. In the present scenario, the discretization of Eqs. (6.3)-(6.6) was carried out in a manner so that the discretized derivatives of phase so obtained, are as pertaining to the Hudgin geometry [49, 45]. In other words, the derivatives in Eqs. (6.3)-(6.6) were numerically evaluated as in Hudgin geometry [49].

Having obtained the gradients of $\varphi(j,k)$ namely $\varphi_x(j,k)$ and $\varphi_y(j,k)$, $\varphi(j,k)$ is reconstructed from $\varphi_x(j,k)$ and $\varphi_y(j,k)$ using the least square method for the Hudgin geometry as follows : since $I(j,k)$ of Eq. (1.1) is given by $N \times N$ matrix, the gradient matrices $\phi_x - \kappa_x$ and $\phi_y - \kappa_y$ are of matrix dimensions $N \times (N-1)$ and $(N-1) \times N$ respectively. Now $\phi_x - \kappa_x$ is rewritten as a $N(N-1) \times 1$ column vector 's_1', where the rows of $\phi_x - \kappa_x$ are concatenated and transposed to form 's_1'. Similarly, $\phi_y - \kappa_y$ is rewritten

as a $N(N-1) \times 1$ column vector 's_2', where the rows of $\phi_y - \kappa_y$ are concatenated and transposed to form 's_2'. The column vector defined as 's' is of size $(2N(N-1)+1) \times 1$ given by $s = [s_1^T, s_2^T, 0]^T$. Now the phase matrix $\varphi(j,k)$ can be rewritten as the column vector '$\boldsymbol{\varphi}$' of size $N^2 \times 1$ by concatenating the rows of $\varphi(j,k)$ followed by transpose. With this we have

$$s = B\,\boldsymbol{\varphi}, \tag{6.11}$$

where B is the Hudgin geometry matrix [45, 49] of size $(2N(N-1)+1) \times N^2$. Clearly B is not a square matrix and hence to invert from the gradient vector 's' to the phase vector '$\boldsymbol{\varphi}$', the method of least squares is used. In other words,

$$\boldsymbol{\varphi} = (B^T B)^{-1} B^T s. \tag{6.12}$$

Owing to symmetries available in B, the matrix inversion required in Eq. (6.12) can be analytically implemented, and it suffices to work with products, inverses, and sums of $N \times N$ matrices in solving Eq. (6.12), as outlined in Section 6.3. $\phi(j,k)$ can now be obtained from $\varphi(j,k)$ by suitably eliminating the tilt.

6.3 Implementation of the least square method

As outlined in Section 6.2, $B^T B$ is of size $N^2 \times N^2$. By the Hudgin geometry [45, 49], we have

$$B = \begin{bmatrix} \mathbb{1}_N \otimes \mathsf{M} \\ \mathsf{M} \otimes \mathbb{1}_N \\ \mathsf{w} \otimes \mathsf{w} \end{bmatrix}, \quad \text{where } \mathsf{M} = \begin{bmatrix} 1 & -1 & 0 & 0 & \dots \\ 0 & 1 & -1 & 0 & \dots \\ 0 & 0 & 1 & -1 & \dots \\ & & \vdots & & \end{bmatrix}, \tag{6.13}$$

is a matrix of size $(N-1) \times N$, and w is a row vector of size $1 \times N$ with all its entries to 1, with $\mathbb{1}_N$ to be the identity matrix of dimension $N \times N$. In solving (6.12), it is evident that we need to evaluate $(B^T B)^{-1}$. It is seen from (6.13) that $B^T B$ can be written as

$$B^T B = [\mathbb{1}_N \otimes \mathsf{M}^T\mathsf{M} + \mathsf{M}^T\mathsf{M} \otimes \mathbb{1}_N + \mathsf{w}^T\mathsf{w} \otimes \mathsf{w}^T\mathsf{w}]. \tag{6.14}$$

Note that $\mathsf{M}\mathsf{w}^T = 0$ and hence w^T is in the nullspace of M, and this implies that $\mathsf{M}^T\mathsf{M}$ and $\mathsf{w}^T\mathsf{w}$ can be diagonalized simultaneously using the same orthogonal transformation.

Further note that $\mathsf{M}^T\mathsf{M}$ is of the form

$$\mathsf{M}^T\mathsf{M} = \begin{bmatrix} 1 & -1 & 0 & 0 & 0 & \dots \\ -1 & 2 & -1 & 0 & 0 & \dots \\ 0 & -1 & 2 & -1 & 0 & \dots \\ & & & \ddots & & \\ 0 & 0 & \dots & -1 & 2 & -1 \\ 0 & 0 & \dots & 0 & -1 & 1 \end{bmatrix}, \tag{6.15}$$

with matrix size $N \times N$ of rank $N-1$, with one zero eigenvalue. By Ref. [165] we know that the eigenvalues of $\mathsf{M}^T\mathsf{M}$ are

$$\Lambda_k = 2 - 2\cos\frac{(k-1)\pi}{N}, \;\; k = 1, 2, \dots, N. \tag{6.16}$$

Also the eigenvectors of $\mathsf{M}^T\mathsf{M}$ are the columns of the orthogonal matrix V whose entries are given by

$$V_{lk} \equiv \frac{\sqrt{2}}{\sqrt{N}}\,\tilde{v}_k \cos\left[\frac{(2l-1)(k-1)\pi}{2N}\right], \tag{6.17}$$

where $l, k = 1, 2, \dots, N$, and $\tilde{v}_k = 1/\sqrt{2}$ when $k = 1$ and 1 otherwise. Also V is readily identified as the discrete-cosine-transform-II matrix of Ref. [165]. With this, it is readily seen that

$$(V^T \otimes V^T)(B^T B)(V \otimes V) = [\mathbb{1}_N \otimes D_1 + D_1 \otimes \mathbb{1}_N + D_2 \otimes D_2], \tag{6.18}$$

where D_2 is $N \times N$ matrix having all entries 0 except whose $(1,1)^{\text{th}}$ entry is N, and $D_1 = \text{diag}\,[\Lambda_1, \dots, \Lambda_N]$. With this we can write

$$[\mathbb{1}_N \otimes D_1 + D_1 \otimes \mathbb{1}_N + D_2 \otimes D_2] \equiv [\mathcal{C}_1 \oplus \cdots \oplus \mathcal{C}_N] \equiv \mathcal{C}, \tag{6.19}$$

where each $\mathcal{C}_j$ is an $N \times N$ diagonal matrix. We have

$$\mathcal{C}_1 = \text{diag}\,\{N^2, \Lambda_2, \dots, \Lambda_N\} \equiv \text{diag}\,\{\mathcal{C}_1^{(1)}, \dots, \mathcal{C}_1^{(N)}\}, \tag{6.20}$$

$$\begin{aligned} \mathcal{C}_j &= \text{diag}\,\{\Lambda_j, \Lambda_2 + \Lambda_j, \dots, \Lambda_N + \Lambda_j\} \\ &\equiv \text{diag}\,\{\mathcal{C}_j^{(1)}, \dots, \mathcal{C}_j^{(N)}\}, \;\; j = 2, 3, \dots, N. \end{aligned} \tag{6.21}$$

It is now clear from Eq. (6.18) that

$$\begin{aligned}(B^TB)^{-1} &= (V\otimes \mathbb{1}_N)(\mathbb{1}_N\otimes V)\mathcal{C}^{-1}(\mathbb{1}_N\otimes V^T)(V^T\otimes \mathbb{1}_N)\\ &= (V\otimes \mathbb{1}_N)[E_1\oplus\cdots\oplus E_N](V^T\otimes \mathbb{1}_N),\end{aligned} \tag{6.22}$$

where $E_j = V\mathcal{C}_j^{-1}V^T$ for $j = 1, 2, \ldots, N$. The (k, l)–th entry of E_j can be written as

$$E_j(k,l) = \sum_{m=1}^{N} V_{km}\ \left[\mathcal{C}_j^{(m)}\right]^{-1}\ V_{lm}.$$

Referring Eqs. (6.12) and (6.13), we also have

$$\begin{aligned}B^Ts &= [\mathbb{1}_N\otimes \mathsf{M}^T\ \mathsf{M}^T\otimes\ \mathbb{1}_N\ \mathsf{w}^T\otimes \mathsf{w}^T]\begin{bmatrix}s_1\\ s_2\\ 0\end{bmatrix}\\ &= (\mathbb{1}_N\otimes \mathsf{M}^T)s_1 + (\mathsf{M}^T\otimes\ \mathbb{1}_N)s_2.\end{aligned} \tag{6.23}$$

Clearly B^Ts is a column matrix of dimension $N^2\times 1$ and can be thought of as constituted of N column blocks $\mathtt{P}_i$ each of matrix size $N\times 1$ concatenated one below the other. That is $B^Ts = [\mathtt{P}_1^T\,\mathtt{P}_2^T\cdots\mathtt{P}_n^T]^T$. With this, B^Ts can be folded and equivalently rewritten as a square matrix of size $N\times N$, that is

$$[\mathtt{P}_1\mathtt{P}_2\cdots\mathtt{P}_n] = [\mathsf{M}^T\,(\phi_x - k_x)^T + (\phi_y - k_y)^T\,\mathsf{M}]_c \equiv \mathsf{F}_\mathsf{c}, \tag{6.24}$$

where the subscript c denotes the column folding. It is now clear that as

$$\begin{aligned}B^Ts &\to (V^T\otimes \mathbb{1}_N)B^Ts,\\ \mathsf{F}_\mathsf{c} &\to \mathsf{F}_\mathsf{c}V.\end{aligned} \tag{6.25}$$

In a similar fashion, as

$$\begin{aligned}(V^T\otimes \mathbb{1}_N)\,B^Ts &\to (E_1\oplus\cdots\oplus E_N)(V^T\otimes \mathbb{1}_N)B^Ts,\\ \mathsf{F}_\mathsf{c}V &\to [G_1G_2\cdots G_N]\equiv G,\end{aligned} \tag{6.26}$$

where G_1 is the multiplication of the first column of $\mathsf{F}_c V$ with E_1, G_2 is the multiplication of the second column of $\mathsf{F}_c V$ with E_2, ..., and G_N is the multiplication of the last column of $\mathsf{F}_c V$ with E_N, and each G_i is a column vector of size $N \times 1$. Finally, as

$$(E_1 \oplus \cdots \oplus E_N)(V^T \otimes \mathbb{1}_N)B^T s \rightarrow (V \otimes \mathbb{1}_N)(E_1 \oplus \cdots \oplus E_N)(V^T \otimes \mathbb{1}_N)B^T s,$$
$$G \rightarrow GV^T = \varphi, \tag{6.27}$$

the required phase matrix. The tilt factors may be appropriately removed from $\varphi(j,k)$ to obtain $\phi(j,k)$. Note that here the indices j and k are discrete.

We note that the analytic diagonalization presented in Eqs. (6.16)-(6.22) substantially speeds up the evaluation of Eq. (6.12) for the Hudgin geometry. For instance, the numerical evaluation of $\{E_1, E_2, \cdots, E_N\}$ of Eq. (6.22), consumed roughly 35 seconds as implemented in a MATLAB code for $N = 512$, where the diagonalization of $\mathsf{M}^T\mathsf{M}$ of Eq. (6.15) was carried out numerically. The same as implemented using analytic substitution based on Eqs. (6.16)-(6.22), consumed roughly 12 seconds. This statistic is as performed on a 2.40 GHz intel core i3 processor with 4 GB RAM.

6.4 Numerical demonstration through simulated interferograms

In this Section, we demonstrate the proposed phase retrieval algorithm on numerically generated interferograms. The phases $\{\phi(j,k)\}$ considered in the interferograms are generated numerically from the Kolmogorov and Tatarski power spectrums.

The Kolmogorov power spectrum [45, 103, 98, 102] is given by

$$\Phi_n(\kappa) = (0.033)\, C_n^2\, \kappa^{-11/3}, \tag{6.28}$$

where C_n^2 is the refractive index structure constant which specifies the strength of the considered turbulence, and κ is modulus of the three dimensional spatial wave number. The associated random phase power spectrum $\Phi_\theta(\kappa)$ can be stated in terms of the Kolmogorov power spectrum as

$$\Phi_\theta(\kappa) = 2\pi\, \kappa^2\, \delta_z\, \Phi_n(\kappa), \tag{6.29}$$

where δ_z is the propagation distance. A random phase picked by a paraxially propagating light field on propagation through distance δ_z can be numerically obtained as follows. The

$\sqrt{\Phi_\theta(\kappa)}$ is numerically evaluated on an appropriately chosen grid and then point wise multiplied on the grid with a random phase factor chosen from a Gaussian distribution. The resulting matrix is then numerically Fourier transformed, and the real part of the Fourier transformed matrix for instance will yield the random phase matrix $\phi(j,k)$ corresponding to the Kolmogorov power spectrum. A random phase matrix obtained in this manner could in principle have a residual tilt, which is removed using the least square fit. In our numerical experiment we implement the algorithm on a grid of size 512×512. Note that the random phases corresponding to the Tatarski power spectrum are analogously generated, with the Kolmogorov spectrum modified as $\Phi_n(\kappa)\exp(-\alpha_0\kappa^2)$, for an appropriate choice for α_0 [102, 98, 45]. Note that in both the Kolmogorov and Tatarski situations, with increasing δ_z, the average path length is increased, and hence the phase.

Table 6.1: summarizes the results of the numerical experiment performed using Kolmogorov power spectrum. Here we have assumed $C_n^2 = 10^{-14}\,\mathrm{m}^{-2/3}$, and a noise level of 20 dB. The first column enumerates the distance δ_z ranging from 10^4 m to 10^5 m in steps of 10^4 m. The second column lists the average correlation values between the generated and estimated phase samples taken over 100 samples, for the tilts removed using methods I and II respectively. The third column lists the average RMS fluctuation of the generated phases about their mean values with increasing δ_z, for 100 samples each. The fourth column lists the average RMS error between the generated and estimated phases, with increasing δ_z, for the tilts removed using methods I and II respectively.

distance (in m)	$\mathrm{C}(\phi, \phi_{\mathrm{est}})$ (method I/II)	RMS $(\phi(x,y))$	error RMS (I/II)
10^4	0.9859/0.9863	0.53	0.13/0.11
2×10^4	0.9867/0.9897	0.74	0.17/0.14
3×10^4	0.9828/0.9894	0.91	0.20/0.16
4×10^4	0.9817/0.9891	1.04	0.23/0.18
5×10^4	0.9826/0.9887	1.18	0.25/0.20
6×10^4	0.9828/0.9885	1.28	0.27/0.21
7×10^4	0.9845/0.9887	1.39	0.28/0.22
8×10^4	0.9811/0.9888	1.51	0.32/0.23
9×10^4	0.9858/0.9889	1.58	0.29/0.24
10^5	0.9837/0.9886	1.65	0.33/0.26

Having generated the random phase matrix $\phi(j,k)$ in the above described manner, the matrix elements $I(j,k)$ of a numerical interferogram can be obtained as

$$I(j,k) = \left[\sum_{\kappa_x,\kappa_y} \{1 + \cos\left[\kappa_x i + \kappa_y j - \phi(j,k)\right]\}\right] + \eta(j,k), \tag{6.30}$$

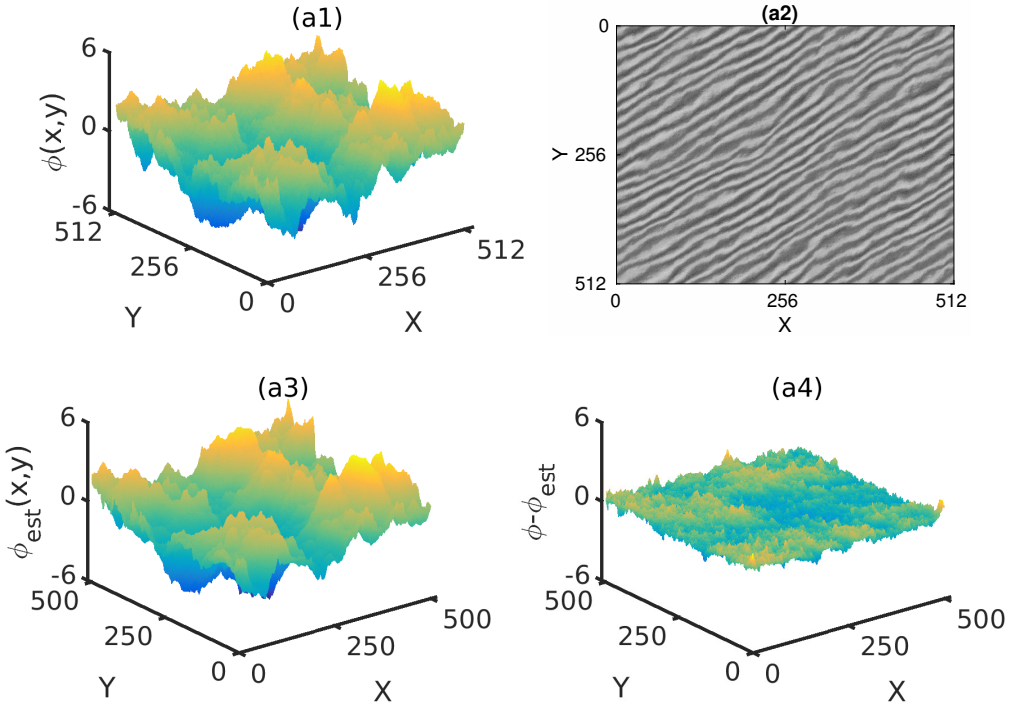

Figure 6.2: Frame (a1) plots numerically generated sample random phases $\phi(j,k)$ for the choice $\delta_z = 10^5\,\mathrm{m}$ and $C_n^2 = 10^{-14}\,\mathrm{m}^{-2/3}$ for the Kolmogorov spectrum. Frame (a2) plots the corresponding numerically generated interferogram. The noisy interferogram was generated numerically as in Eq. (6.30), where the summations over the tilt factors κ_x and κ_y about their peak values have been carried out, and Gaussian white noise of 20 dB was added. Frame (a3) plots the respective estimated phases corresponding to the interferogram in frame (a2). For the phases in frames (a1) and (a3) we obtain $C(\phi,\phi_{\mathrm{est}}) = 0.9843$. Frame (a4) plots the respective difference between the generated and estimated phases for the present phase samples. In the present situation, the RMS of the error phase in frame (a4) is ≈ 0.35 radians. Here, tilt was removed using method I.

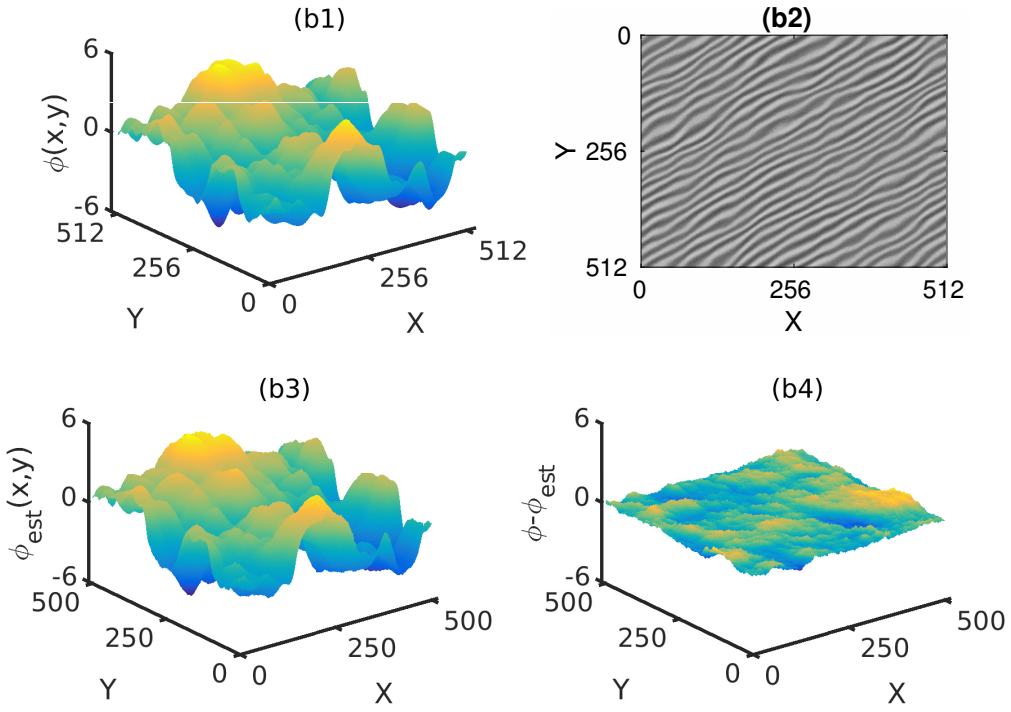

Figure 6.3: Frame (b1) plots numerically generated sample random phases $\phi(j,k)$ for the choice $\delta_z = 10^5\,\mathrm{m}$, $C_n^2 = 10^{-14}\,\mathrm{m}^{-2/3}$, and $\alpha_0 = 0.0001$ for the Tatarski spectrum. Frame (b2) plots the corresponding numerically generated interferogram. Again, as in frame (a2) of Figure 6.2, the noisy interferogram was generated numerically as in Eq. (6.30), where the summations over the tilt factors κ_x and κ_y about their peak values have been carried out, and Gaussian white noise of 20 dB was added. Frame (b3) plots the respective estimated phases corresponding to the interferogram in frame (b2). For the phases in frames (b1) and (b3) we obtain $C(\phi, \phi_{\mathrm{est}}) = 0.9928$. Frame (b4) plots the respective difference between the generated and estimated phases for the present phase samples. In the present situation, the RMS of the error phase in frame (b4) is ≈ 0.21 radians. Here, tilt was removed using method I.

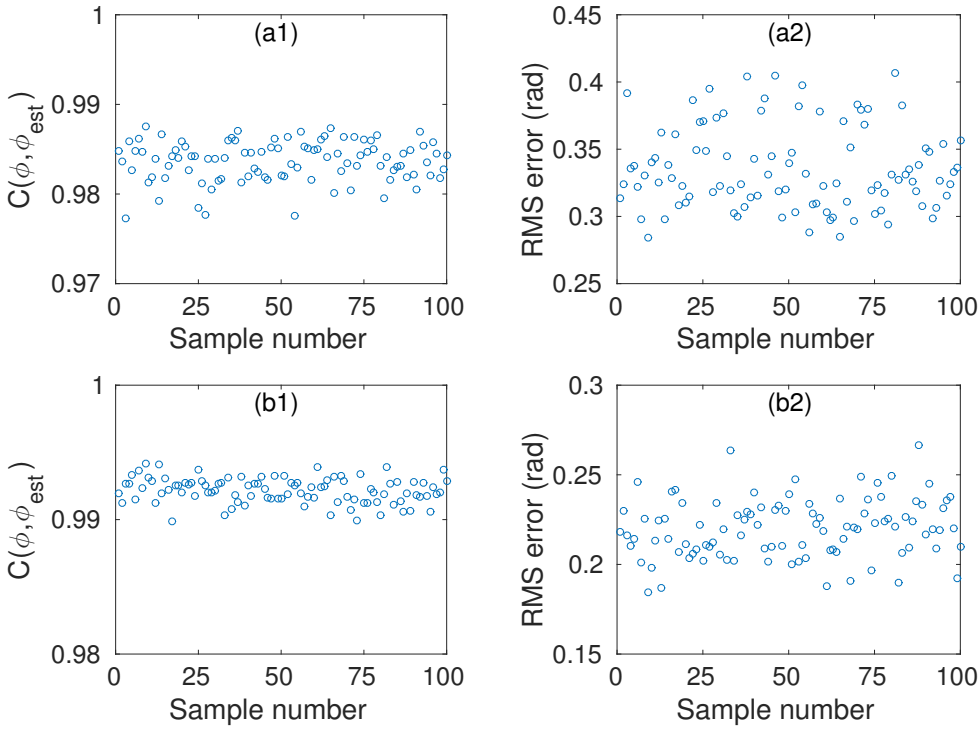

Figure 6.4: Frames (a1), (b1), and (a2), (b2) scatter plot the correlation and RMS of the error between the numerically generated and estimated phases for the Kolmogorov and Tatarski spectrums, for 100 samples. In the present figure, method I was used to remove the tilt.

Table 6.2: summarizes the results of the numerical experiment performed using Tatarski power spectrum. Here we have assumed $C_n^2 = 10^{-14}\,\mathrm{m}^{-2/3}$, $\alpha_0 = 0.0001$, and a noise level of 20 dB. The first column enumerates the distance δ_z ranging from $10^4\,\mathrm{m}$ to $10^5\,\mathrm{m}$ in steps of $10^4\,\mathrm{m}$. The second column lists the average correlation values between the generated and estimated phase samples taken over 100 samples, for the tilts removed using methods I and II respectively. The third column lists the average RMS fluctuation of the generated phases about their mean values with increasing δ_z, for 100 samples each. The fourth column lists the average RMS error between the generated and estimated phases, with increasing δ_z, for the tilts removed using methods I and II respectively.

distance (in m)	$\mathrm{C}(\phi, \phi_{\mathrm{est}})$ (method I/II)	RMS $(\phi(x, y))$	error RMS (I/II)
10^4	$0.9889/0.9897$	0.50	$0.11/0.10$
2×10^4	$0.9886/0.9942$	0.70	$0.15/0.12$
3×10^4	$0.9924/0.9942$	0.86	$0.14/0.12$
4×10^4	$0.9904/0.9940$	0.99	$0.17/0.13$
5×10^4	$0.9910/0.9942$	1.11	$0.18/0.14$
6×10^4	$0.9870/0.9942$	1.21	$0.22/0.15$
7×10^4	$0.9925/0.9945$	1.30	$0.19/0.15$
8×10^4	$0.9924/0.9947$	1.39	$0.20/0.16$
9×10^4	$0.9905/0.9949$	1.48	$0.23/0.16$
10^5	$0.9914/0.9952$	1.56	$0.23/0.17$

where the summation over the tilt factors κ_x and κ_y is performed to account for the quasi-monochromaticity of the source [2, 38, 39], and $\eta(j,k)$ is the additive Gaussian white noise. Here in the present situation, $\eta(j,k)$ is generated using the command 'AGWN' in MATLAB, for varying noise levels in decibels. And since $\eta(j,k)$ could take both positive and negative values, a minimum overall shift is added to $I(j,k)$ to make it point wise positive. κ_x and κ_y are allowed to vary around their respective peak values, as drawn from a Gaussian distribution whose width was sufficiently narrow (in the present scenario it was lesser than the width of a pixel), to account for the quasi-monochromaticity. Further the peak tilt factor values are assumed to be non-integer multiples of $2\pi/N$. For instance, in the present numerical experiment, $\kappa_x = (2\pi/N) \times x$ and $\kappa_y = (2\pi/N) \times y$ were assigned mean peak values $\kappa_{0x} = (2\pi/N) \times x_0$ and $\kappa_{0y} = (2\pi/N) \times y_0$ with $x_0,\ y_0$ assuming the non-integer values 20.3 and 15.3 respectively, for $N = 512$. And the tilt factors κ_x and κ_y were drawn from a Gaussian distribution about their respective peak values from a Gaussian of width 0.417, with corresponding $x,\ y$ varied in steps of 0.1 up to 0.3, about x_0 and y_0. Further we assume that the phase $\phi(j,k)$ is stationary despite varying κ_x and κ_y.

Having generated the interferograms in above described manner, the phase with its residual tilt is estimated using the algorithm described in Section 6.2. In the present situation, for all the numerical examples we study, $I_0(j,k)$ and $\eta(j,k)$ were filtered as follows : $I(j,k)$ was Fourier transformed, and the central peak corresponding to I_0 situated in the central four pixels in the Fourier plane was removed. Further all frequencies with radius $\geq 100^2$ pixels from pixel points $(x_0 = 20.3, y_0 = 15.3)$ and $(x_0 = -20.3, y_0 = -15.3)$ were also removed. This choice of radius in the frequency plane roughly ensured that the 'large frequency' components as contributed by the Kolmogorov and Tatarski phase spectrums were retained, while the 'higher frequency' contributions from $\eta(j,k)$ were neglected. The remaining signal was inverse Fourier transformed and then Hilbert transformed to obtain the discretized versions of Eqs. (6.1) and (6.2). Having run the algorithm and having obtained $\varphi(j,k)$, the residual tilt is then removed using the following two methods. In the first method (i.e., method I), phase samples $\{\varphi(j,k)\}$ estimated for a particular choice of C_n^2 and δ_z over several interferograms are averaged to obtain a 'plane' phase, which is then subtracted from each of the estimated phases $\varphi(j,k)$ to yield $\phi(j,k)$. Here the 'plane' phase is sufficiently 'plane' owing to the fact that each $\phi(j,k)$ was sufficiently random. The randomness of $\phi(j,k)$ can be safely assumed in the present scenario since they were generated from atmospheric turbulence models. In the second method (i.e., method II), each interferogram is treated independently, and the plane phase that best fits the estimated $\varphi(j,k)$ is obtained using the least square method, and then subtracted from

the estimated $\varphi(j,k)$ to remove the tilt. The second method could be hence thought of as single-shot, and this of value in several experimental situations when one is required to estimate the phase with the availability of only a single interferogram [16, 166, 35, 167].

To numerically compare the generated and estimated phases, we make use of the phase correlation function. Given phases $\phi_1(j,k)$ and $\phi_2(j,k)$, the phase correlation function is defined as

$$\mathrm{C}(\phi_1,\phi_2) = \frac{\sum_{j,k} \tilde{\phi}_1(j,k)\,\tilde{\phi}_2(j,k)}{\left[\sum_{j,k} \tilde{\phi}_1(j,k)^2\right]^{1/2}\left[\sum_{j,k} \tilde{\phi}_2(j,k)^2\right]^{1/2}}, \tag{6.31}$$

where $\tilde{\phi}(j,k) = \phi(j,k) - \langle\phi(j,k)\rangle$. Here $\langle\cdot\rangle$ denotes the ensemble average. Note that $-1 \leq \mathrm{C}(\phi_1,\phi_2) \leq 1$, and $C(\phi_1,\phi_2) = 1$ only when $\phi_1(j,k) = \phi_2(j,k)$ [168, 2]. We also make use of the root mean square (RMS) of the difference between the numerically generated and estimated phases. For instance, for phases $\phi_1(j,k)$ and $\phi_2(j,k)$, the RMS of the difference is given by $\sqrt{\frac{1}{N}\left[\sum_{j,k}(\tilde{\phi}_1(j,k) - \tilde{\phi}_2(j,k))^2\right]}$.

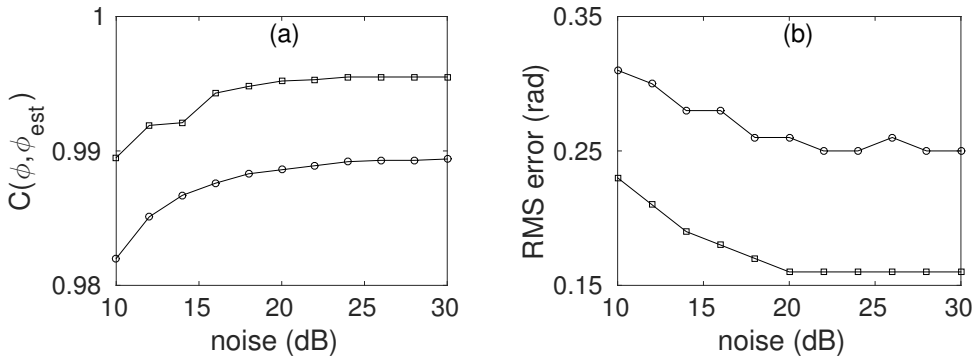

Figure 6.5: Here frame (a) plots the average variation of the correlation between the numerically generated and estimated phases with varying noise, and frame (b) plots the average error RMS in radians between the generated and estimated phases with varying noise, for the Kolmogorov and Tatarski phases, with $\delta_z = 10^5\,\mathrm{m}$. In both the plots, the circles correspond to Kolmogorov phases, and squares correspond to the Tatarski phases, and the averaging was performed over 100 samples each. It may be noted that for this choice of δ_z, both the Kolmogorov and Tatarski phases roughly varied between $\pm 2\pi$ radians. Here, the tilt was removed using method II.

In implementing the algorithm on an interferogram as in Eq. (6.30), we note the following : there are low frequency components on the estimated $I_0(j,k)$ (refer Eqs.(6.1) and (6.2)), and $I_0(j,k)$ is not sufficiently constant on the grid, especially tailing near the boundaries, which is implied by the fact there is a summation over κ_x and κ_y in obtaining the

interferogram as in Eq. (6.30). Consequently, this leads to a decrease in correlation, and increase in error RMS between the simulated and estimated phases in our numerical experiment, when the whole grid is taken in to consideration. Thus in the present numerical experiment, while the phase estimation algorithm runs on the grid of size 512×512, the correlation and error between the generated and estimated phases is evaluated only on the truncated grid of size 500×500, with the phase estimated at the boundary being ignored. And this improves the fidelity between the generated and estimated phases, while reducing the error. The low frequency components in the estimated $I_0(j,k)$ are also observed in the experimentally retrieved interferograms (see Section 6.5). Consequently, the phase estimation algorithm is run on the experimentally observed interferograms of size 400×400, but the correlation and error between the estimated phases is evaluated only on a grid of size 380×380. Further, in Eqs. (6.3)-(6.10) we have assumed that the intensity I_0 as estimated by the Hilbert transform is sufficiently constant. This however does not hold for instance when the encoded phases are sufficiently 'large and fluctuating'. For example in the present numerical experiment, for the Kolmogorov situation, for the choice of $C_n^2 = 10^{-14}\,\mathrm{m}^{-2/3}$ and $\delta_z = 10^5\,\mathrm{m}$, there are instances of particular (j,k), where the phases are large and fluctuate well enough so that fore mentioned approximation is not valid, and the $I_0(j,k)$ at that particular (j,k) can go sufficiently low so that the RHS of Eqs. (6.9) and (6.10) is ill defined, which can lead to an over estimation of phase at that grid point. To remedy this, any $I_0(j,k)$ whose value is greater or lesser than $\langle I_0(j,k)\rangle$ by an amount $0.05 \times \langle I_0(j,k)\rangle$, is replaced with a corresponding averaged value, the average being evaluated over the nearest eight points on the grid. Here $\langle I_0(j,k)\rangle$ is the mean value of the background intensity as evaluated on a full sample interferogram. Such a nearest neighbor averaging of the background intensity was performed both in the numerically generated as well as experimentally measured interferograms.

We now summarize our results. In Figures 6.2 and 6.3, we illustrate the results for the choice of $C_n^2 = 10^{-14}\,\mathrm{m}^{-2/3}$ with $\delta_z = 10^5\,\mathrm{m}$, and noise level of 20 dB. Frames (a1) and (b1) plot samples of random phases corresponding respectively to the Kolmogorov and Tatarski spectrums. Here for the Tatarski spectrum we have assumed $\alpha_0 = 0.0001$ as indicated earlier. Frames (a2) and (b2) plot the corresponding interferograms, and frames (a3) and (b3) plot the respective phases as estimated by the algorithm. Frames (a4) and (b4) plot the respective difference between the generated and estimated phases. Frames (a1), (b1), and (a2), (b2) of Figure 6.4 summarize the obtained correlation and RMS error between the generated and estimated phases for 100 samples each for the Kolmogorov and Tatarski spectrums, where the tilt has been removed using method I. Tables 6.1 and 6.2

summarize the results for varying δ_z, with δ_z increasing from 10^4 m to 10^5 m at intervals of 10^4 m, and noise level of 20 dB. Here both methods I and II were used to remove the tilts, for 100 phase samples for each δ_z. They list the average RMS of the numerically generated phase, and the average correlation and error RMS between the generated and estimated phases, for 100 samples, in each scenario. It may be noted from Tables 6.1 and 6.2, that the correlation between the generated and estimated phases for the Tatarski power spectrums is on an average higher than their respective Kolmogorov counterparts, and the error RMS is also comparatively lesser, for each δ_z. This may be attributed to the relatively smooth nature of the Tatarski phases in comparison to their Kolmogorov counterparts. Further, the average correlation between the generated and estimated phases is lower in both the Kolmogorov and Tatarski situations when the tilt was removed using method I, and this may be attributed to the fact that the 'plane phase' used to remove the tilt was obtained by averaging the random phases over only 100 samples. Nevertheless, when there is no a priori knowledge of the residual tilt of a random phase, the tilt removal using method I could be useful. Further, for relatively small phases as in the situation when $\delta_z = 10^4$ m, the error RMS is seen to be relatively higher in respect of the input phase in both the Kolmogorov and Tatarski situations, and this may be attributed to dominance of noise over the signal, in the estimation of the slopes. Figure (6.5) summarizes the average variation of the correlation and error RMS between the numerically generated and estimated phases for varying noise levels, for $\delta_z = 10^5$ m, in both the Kolmogorov and Tatarski situations, where the tilt was removed using method II.

Remark : In both proposed algorithms presented in Sections 5.3 and 6.2 we observe that the noise is introduced while measuring intensities using CCD, and we measure it in dB, as indicated in Section 3.9. It can be seen that the iterative algorithm proposed in Section 5.3 retrieves the phase unambiguously, i.e., with almost 100% correlation between the input and converged wave fields, even in the presence of 10 dB noise almost for all tested numerical examples. On the other hand, the proposed algorithm in Section 6.2 retrieves phase with a correlation just above 98% and an RMS error of ≈ 0.3 radians in the presence of 10 dB noise for the Kolmogorov phases (see Figure 6.5). Thus, the former algorithm is more immune to noise than the later. However, it should also be kept in mind that the former algorithm needs three intensity patterns for phase estimation, as opposed to the later which estimates phase from a single interferogram.

6.5 Experimental demonstration using Mach–Zehnder setup

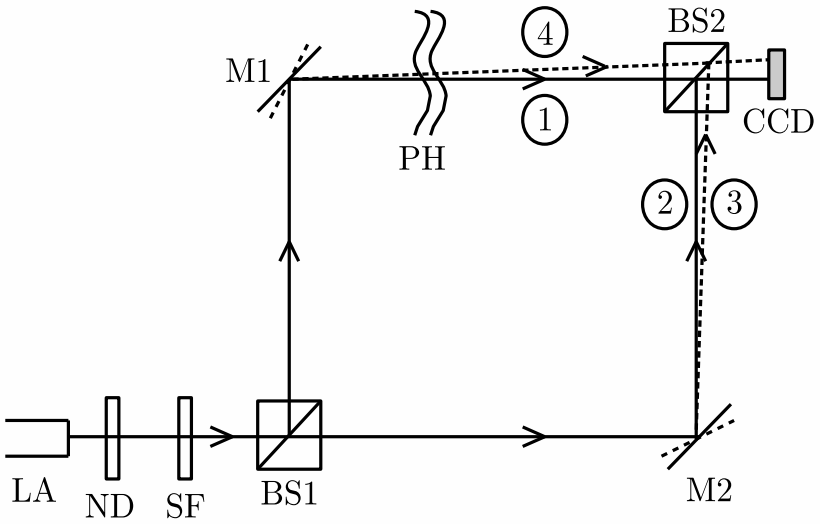

Figure 6.6: Shown here is the experimental setup to record interferograms with different tilts. Coherent wave field from laser (LA) is first attenuated by the neutral density (ND) filter, spatial filtered (SF), and then collimated using a thin lens (not shown here). The resulting beam is then split by beamsplitter BS1. Before these fields recombine at beamsplitter BS2 and being recorded by the CCD, one of the fields passes through the pseudo-random phase plate (PRPP). Spatial frequency of the interferograms can be controlled by the tilts given to mirrors M1 and M2. For the tilt position 1, wave fields 1 and 2 recombine at BS2 and the CCD records the interferogram. Then both M1 and M2 or one of them are adjusted to get a different tilt, say tilt position 2, and the wave fields 3 and 4 recombine at BS2 and the CCD records the interferogram. Note that both wave fields 1 and 4 pass through the same portion of the PRPP, and hence the encoded random phase in the interferograms corresponding to these two different tilts are the same.

In this Section, we summarize the results of two experiments which were carried out to demonstrate the consistency of the phase retrieval algorithm. In the first experiment (see Figure 6.6), the standard Mach-Zehnder setup with a collimated laser light source is used. Coherent wave field from He-Ne laser (LA) with $633\,\mathrm{nm}$ wavelength is first attenuated by the neutral density (ND) filter, and spatial filtered (SF) before being collimated by a lens. This beam is then split into two beams using the beamsplitter BS1, and these beams travel towards mirrors M1 and M2. The beam reflected from M1 passes through a pseudo-random phase plate (PRPP) [169] and is recombined with the beam reflected from M2 using the

beamsplitter BS2. The resulting beam is captured by the CCD camera, and the interferogram has now encoded the phase information of the PRPP. Now we introduce some extra tilt by adjusting M1 and M2 and let the beam reflected from M2 to pass through the same portion of the PRPP and record another interferogram. So these two interferograms carry the same phase information apart from the extra residual tilt. Here, we note that the PRPP used in the experiment consists of a five layer system, with two outer layers of BK-7 glass, two layers of near index matching polymer, and one layer of acrylic with a turbulence profile written on to it on one side [169]. Also, it was observed that peak to valley phase variation in the PRPP plate is roughly $6\pi \approx 19$ radians.

The interferograms were then recorded on a CCD camera which consists of 640×480 pixels, with each pixel of size $9.9\,\mu\mathrm{m} \times 9.9\,\mu\mathrm{m}$. Though there is an availability of 640×480 pixels, we restrict our observation area to 400×400 pixels for the sake of uniform illumination as available from the collimated beam. For each sampled region of the PRPP, two interferograms were recorded, each corresponding to two different fixed tilts (see, for instance, frames (a) and (b) of Figure (6.7)). The phases for the same sampled region of the PRPP, was then estimated from the two interferograms corresponding to the two tilts and compared. In Figure (6.7), frames (a) and (b) are the two interferograms for a particular sampled region of PRPP for two different tilts. Note that the fringes in frame (b) has a higher spatial frequency as compared to those in frame (a), indicating the different tilts. Frames (c) and (d) plot the estimated phases where method I (see Section 6.4) was used to remove the residual tilt. For the present example, the phases in frames (c) and (d) have a correlation of 0.9911. In the experiment, 300 regions of the PRPP were sampled. First, 300 interferograms were recorded for the sampled regions for the first tilt, and then the same was repeated for the second tilt. This sequential recording of the interferograms was possible due to the in built controllable stepper motor in the PRPP setup [169]. The phases for each of these 300 interferograms both with the first and second tilts were then estimated using the algorithm, and the residual tilts were removed using both methods I as well as II. Frames (a), (b), (c), and (d) of Figure (6.8) summarize the results. The observed correlations is on an average greater that 0.96 for both the methods suggesting that the phase retrieval algorithm is consistent.

In the second experiment, the phase sharing Mach–Zehnder interferometric setup introduced in Ref. [168] is used (see Figure 6.9). A wave field from LA of 633 nm wavelength which is linearly polarized is passed through a ND filter followed by a HWP oriented such that the wave field emerging from it is 45° polarized. This wave field is then spatial filtered before being collimated by a lens. The collimated wave field is passed through a PBS to

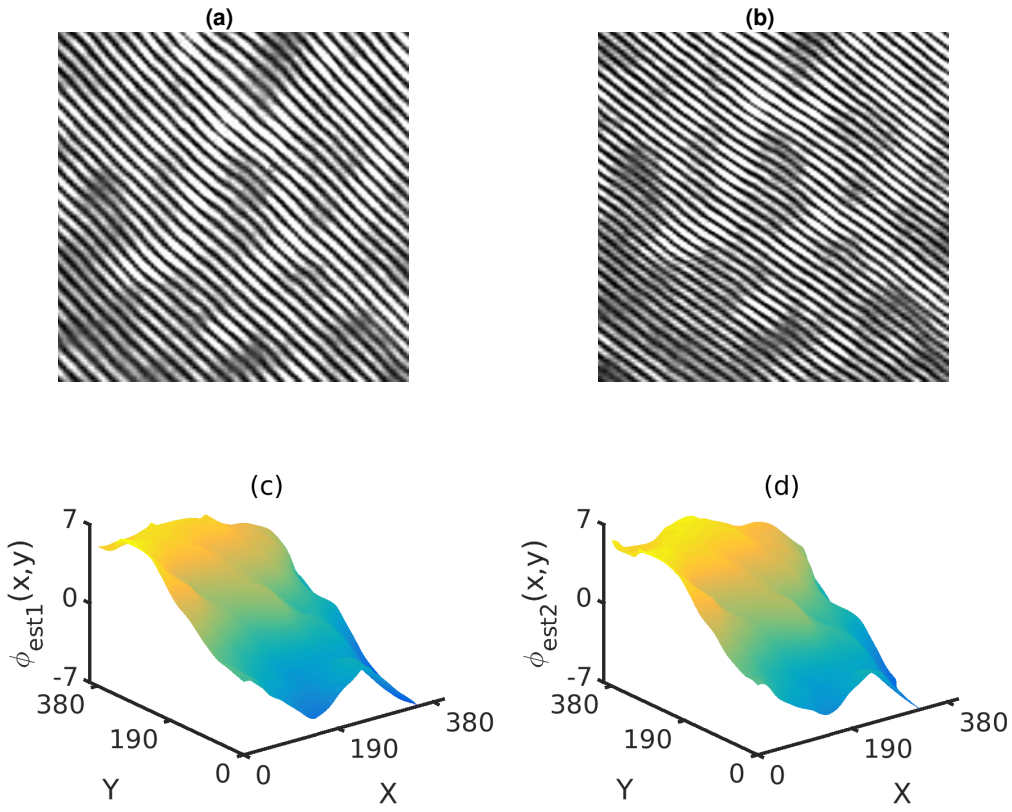

Figure 6.7: Frames (a) and (b) plot the interferograms corresponding to the same sampled region of the PRPP corresponding to two different tilts. Notice the increased spatial frequency of the fringes in frame (b) in respect of fringes in frame (a). Frames (c) and (d) plot the phases as retrieved from the interferograms in frames (a) and (b), where method I (see Section 6.4) was used for tilt removal, and phase averaging was done on 300 samples. Note that the estimated phases are plotted only on a grid of size 380×380 even though the phase estimation algorithm was run on a grid of size 400×400. For the present example, the correlation between the two phases in frames (c) and (d) was found to be 0.9911, with error RMS of 0.4856 radians.

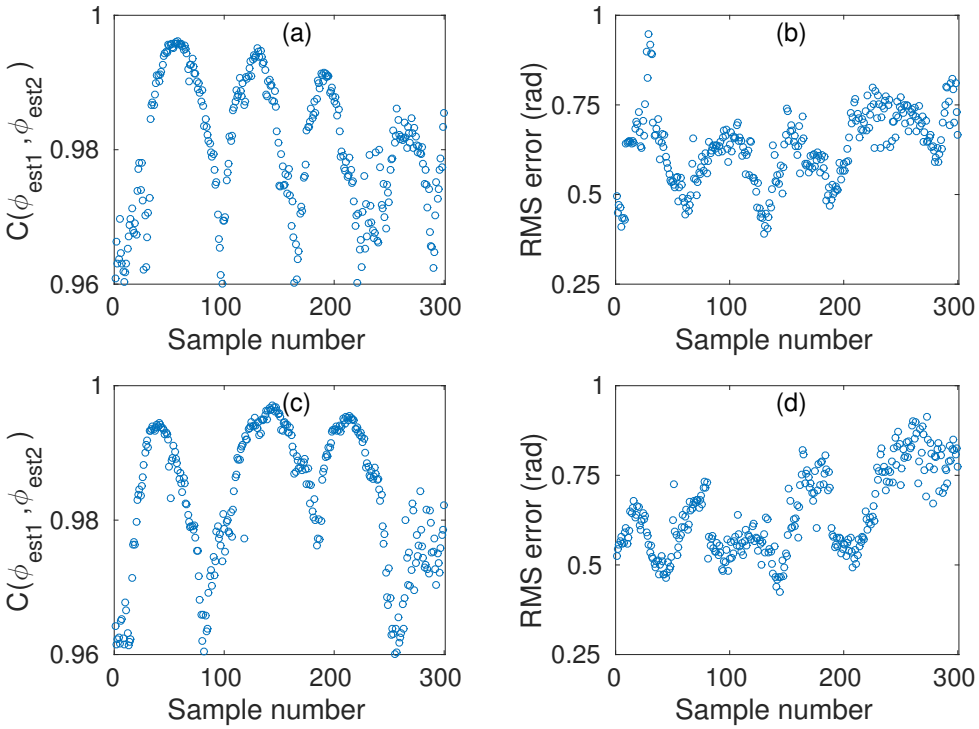

Figure 6.8: Frames (a) and (b) scatter plot the correlation values and the error RMS respectively between estimated phases corresponding to the two different tilts in the first experiment (see Figure 6.6), for 300 sampled regions of the PRPP, where the tilt was removed using method I (see Section 6.4). Frames (c) and (d) plot the same where method II (see Section 6.4) was used to remove tilt in the same experiment. It may be noted that the phases roughly varied between ± 7 radians.

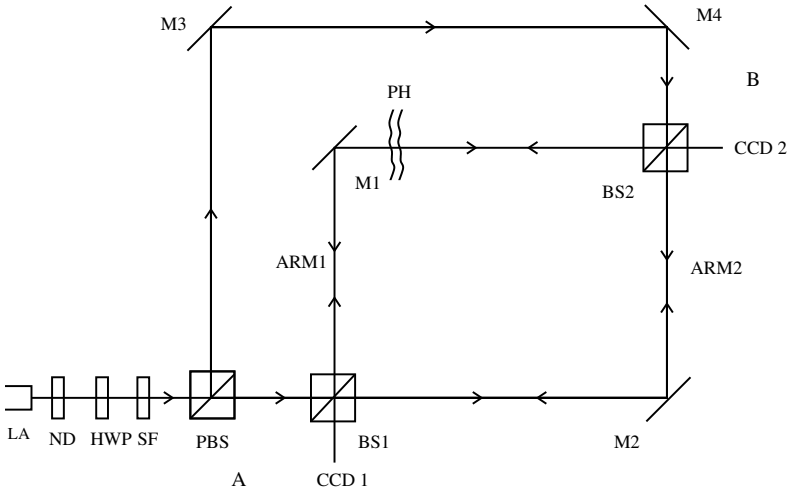

Figure 6.9: Shown here is the phase sharing experimental setup. Coherent wave field from LA (which is fully polarized) is attenuated, spatially filtered, collimated, and passed through a rotated half-wave plate (HWP), before being split by a polarizing beam-splitter (PBS) into two wave field sources with orthogonal polarizations. These two wave field sources act as the two inputs at the two arms of the Mach–Zehnder interferometer. Both these sources are split and recombined by Beam-splitter 1 and Beam-splitter 2 (BS1, BS2) to obtain the interference patterns at the two observer ends (A and B) of the interferometer. The PRPP is inserted in one of the arms of the interferometer so that both the wave field sources with orthogonal polarizations encounter the same phase difference in the two arms of the interferometer. LA, Laser; ND, Neutral Density Filter; SF, Spatial Filter Assembly; P, Polarizer; BS, Beam Splitter; M, Mirror; PH, Phase; CCD, Charged-coupled Device Camera; PBS, Polarizing Beam Splitter; HWP, Half Wave Plate.

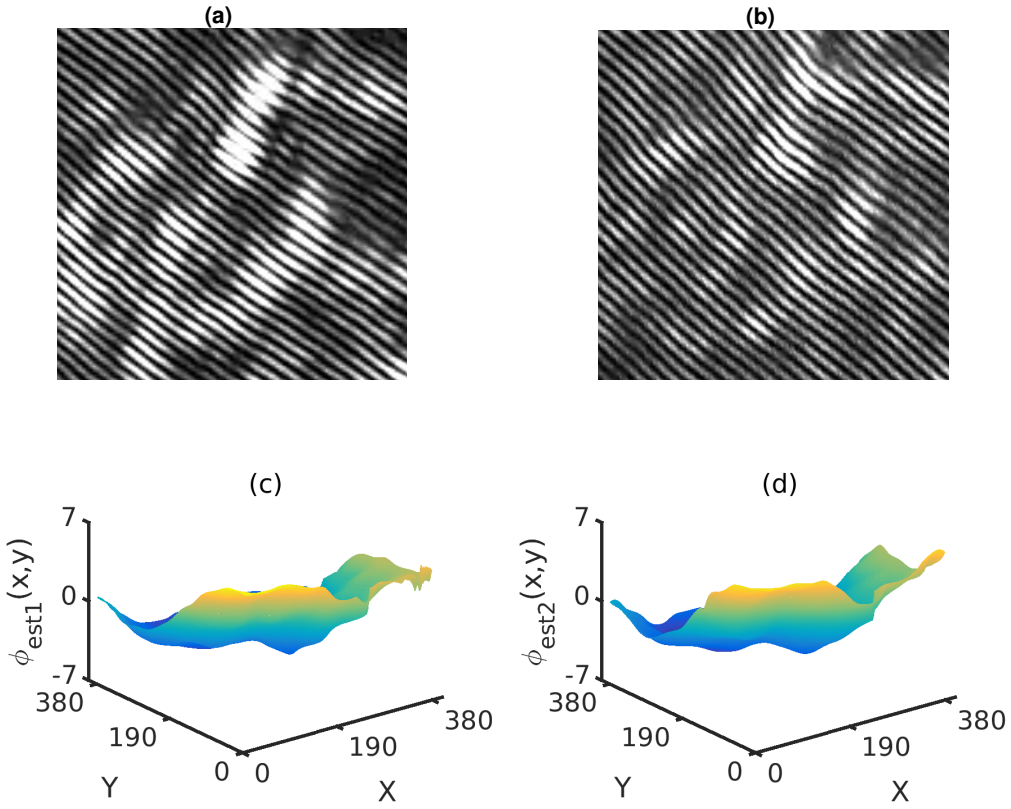

Figure 6.10: Frames (a) and (b) plot the interferograms corresponding to the same sampled region of the PRPP corresponding to the phase sharing experiment. Frames (c) and (d) plot the phases as retrieved from the interferograms in frames (a) and (b), where method I (see Section 6.4) was used to remove tilt, and phase averaging was done on 300 samples. Again, the estimated phases are plotted only on a grid of size 380×380 even though the phase estimation algorithm was run on a grid of size 400×400. For the present example, the correlation between the two phases in frames (c) and (d) was found to be 0.9933, with error RMS of 0.3361 radians.

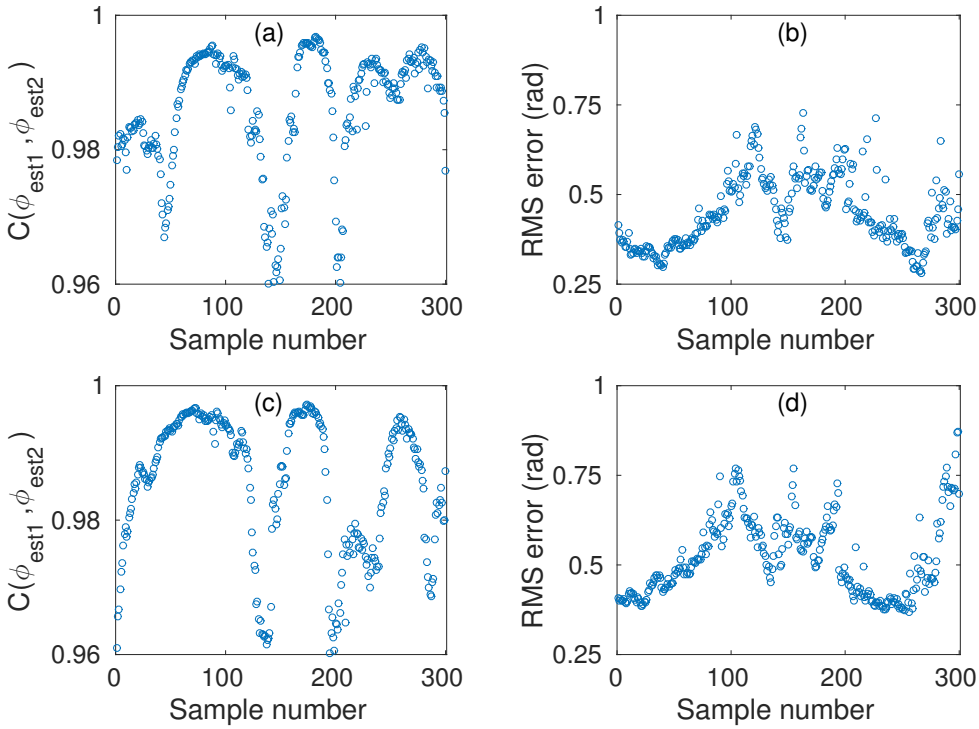

Figure 6.11: Frames (a) and (b) scatter plot the correlation values and the error RMS between phases estimated at the two ends of a Mach-Zehnder interferometer, for 300 sampled regions of the PRPP in the phase-sharing setup (see Figure 6.9), where method I (see Section 6.4) was used for tilt removal. Frames (c) and (d) plot the same in the phase-sharing experiment, where method II (see Section 6.4) was used to remove tilt. It may again be noted that the phases roughly varied between ± 7 radians.

create two sources of wave fields, one with horizontal polarization, and the other with vertical polarization. These two wave fields act as the two light sources for our work. One of the light field sources emerging from the PBS goes straight to BS1 which is at observer port A and gets split and reflected (by M1 and M2) before being recombined at BS2 (which is placed at observer port B). The interference thus obtained at observer port B is recorded on a CCD camera. The second light field source from the PBS is reflected by M3 and M4 before entering BS2 at observer port B. The second light source splits at BS2 and the two sources are reflected by M2 and M1 before recombining at BS1. The interference pattern thus obtained is recorded on a CCD camera at observer port A. The wave fields from these two light sources don't interfere in view of Fresnel-Arago's law [170], and hence we obtain two similar interferograms at CCDs placed at ports A and B (see Figure 6.10).

Now 'Shared' interferograms corresponding to the same sampled region of the PRPP were measured at the two opposing ends of the Mach–Zehnder interferometer for 300 samples (see, for instance, frames (a) and (b) of Figure 6.10). The phases were then estimated using the algorithm and the residual tilts were then removed using both methods I as well as II, the results of which are summarized in frames (a), (b), (c), and (d) of Figure (6.11). And we again find that the correlation between the estimated phases is greater that 0.96 as before, suggesting that the phase estimation algorithm is consistent. In both the experiments, the correlations between the phases were evaluated on a grid of size 380×380, even though the phase estimation algorithm was implemented on the grid of size 400×400. To this end, we have two remarks. First, as mentioned above, the grid size 400×400 was chosen because uniform illumination from the collimated beam was available on a smaller region of CCD. Second, the intensity $I_0(x, y)$ (see Eq. (1.1)) is tailing near the boundaries due to summation over spatial frequencies κ_x and κ_y as indicated in Eq. (6.30). This leads to decreased correlation (or equivalently increased RMS error), and hence we have restricted to 380×380 pixels only, even though the algorithm was run on 400×400 pixels. Further, the displaced signals obtained from the Fourier transform of an interferogram were Gaussian filtered to suppress the 'noise' and the other high frequency components. And this led to a substantial improvement on the correlation between the estimated phases.

6.6 Concluding remarks

We have proposed an algorithm to extract the phase in an unwrapped form using the Hilbert transform, from an interferogram with perturbed straight line fringes. First the phase gradients are extracted from the interferogram using the Hilbert transform, and then the extracted

phase gradients are used to estimate the phase, using the method of least squares, for the Hudgin geometry. In this regard, a simplification in the implementation of the least squares is outlined. The inversion involved in the implementation of the least squares is reduced to multiplication and sums of $N \times N$ matrices, even though the original problem requires inverting a $N^2 \times N^2$ matrix. An analytic simplification of the matrix diagonalization is also presented where the connection between discrete-cosine-transform-II (DCT-II) matrix and the Hudgin geometry matrix is effectively used. It is found that this speeds up the phase retrieval from the slopes for the Hudgin geometry. Thus the present analytic simplification is not only useful for the present context, but also in dynamic phase estimation using wavefront sensors, where the phase gradients are extracted from a wavefront sensor, for the Hudgin geometry [45, 49]. The consistency of the proposed algorithm has been demonstrated on both numerically generated noisy interferograms as well on experimentally measured interferograms, for phases which are random and are generated through passage of a collimated paraxial light field through atmospheric turbulence like situations. Thus the present algorithm is very relevant and useful, when for instance, one is interested in distillation of a secret key by two remote observers who use atmospheric turbulence as the common source of randomness, as demonstrated in the phase-sharing Mach-Zehnder set up of Ref. [168], where perturbed straight line fringes were observed by the two remote observers. The present algorithm could also be useful in other experimental contexts where 'perturbed' straight line fringes are observed [16, 35, 166, 167]. We further observe that while the algorithm is designed for interferograms of size $N \times N$, it could be effectively extended to more general inteferograms of arbitrary size, using the methods outlined in Refs. [169, 171]. We finally note that the method will not work for the for interferograms which can have closed [172, 173, 174, 175, 176] or forked [8, 65, 177, 178, 85] fringes (phases with dislocations), owing to its inherent dependence on the Hilbert transform. Note that the problem of retrieving phases with dislocations has already been demonstrated numerically in Chapter 5.

Chapter 7

Conclusion and possible future research works

7.1 Conclusion

In this thesis we have explored some aspects of phase estimation problems through intensity measurements. In this regard, we have proposed two new algorithms, and demonstrated one numerically, and the other numerically as well as experimentally. In constructing an algorithm to retrieve phases with dislocations, we have made use of the new results obtained in Chapter 4 in regard of FOOS. The obtained results may be summarized as follows :

1. We have proved that any general FOOS can be realized (in a lab) using a maximum of 4 thin convex lenses and 14 thin cylindrical lenses of positive focal length alone. In addition, explicit realizations of optical transformations including differential free and inverse free propagation, partial Fourier transformation, inverse partial Fourier transformation, image reflector, differential magnifier, differential fractional Fourier transformation, gyrator, and cross-gyrator have been provided. In fact, the decompositions of the optical transformations such as differential free and inverse free propagation, inverse partial Fourier transformation, differential magnifier, and differential fractional Fourier transformation, to the best of our knowledge, have been obtained for the first time.

2. We have proposed an algorithm to extract phases with dislocations using partial Fourier transformation, and thus measuring the OAM of the wave field, with the knowledge of three transverse plane intensity measurements alone, and not requiring any boundary conditions. This algorithm has been tested numerically using Monte-Carlo simulations on numerous random samples of random complex linear super-

position of paraxial wave fields, and unambiguous phase retrieval has been demonstrated for all such cases.

3. We have also proposed a single-shot algorithm that can extract the phase information encoded, without phase unwrapping, from perturbed straight line fringes. Phase gradients are obtained by Hilbert transform, and consequently the phase is reconstructed using the knowledge of phase gradients and the method of least squares for the Hudgin geometry. Exploiting the connection between the Hudgin geometry matrix and discrete cosine transform matrix for the first time, to the best of our knowledge, has resulted in huge reduction of the computational time. This algorithm has been successfully demonstrated to work on numerically generated interferograms whose phases were random, and generated using Kolmogorov and Tatarski atmospheric turbulence models. Also, the algorithm has been shown to work well on interferograms with random phase obtained from a Mach–Zehnder setup with PRPP inserted in one of the arms.

7.2 Possible applications

First we mention few research areas where realization of general FOOS can find applications. Phase retrieval algorithms from two as well as multi-plane intensity measurements [58, 133, 63] typically use elementary optical transformations such as Fourier transform, free propagation, and fractional Fourier transform (see, for instance, Chapter 11 of Ref. [116]). Because any complicated FOOS can be realized explicitly using free propagation and thin lenses (Chapter 4), phase retrieval algorithms involving such complicated FOOS can readily be implemented in lab.

Second, high-speed parallel processing can be made possible using optical information processing, where the required transformations are implemented by means of refractive optical elements [179, 108]. For instance, Fourier transform of a signal can be implemented optically using a thin convex lens (see Figure 4.1). Now any real time application involving instantaneous implementation of complex optical transformations can easily be performed using free propagation and thin lenses.

Third, it has been demonstrated recently that how modern digital holographic systems can be designed and analyzed using LCT (see Chapter 12 of Ref. [116]). Also, there has been growing interest towards image encryption using standard optical transformations such as Fourier and fractional Fourier transformations (see Chapter 13 of Ref. [116] and

references therein). Our realization of optical transformations can readily find applications in such research areas.

Now we explore few research areas where our iterative algorithm developed in Chapter 5 can be useful. Sorting of orbital angular momentum modes is an active research area [180, 181]. These OAM sorters make use of Cartesian to log-polar coordinate transformation performed by special optical elements and can find out $|c_j|^2$, the probability amplitude, of the constituent Laguerre-Gaussian modes. These sorters are widely used in implementation of quantum walks [182] and quantum algorithms with classical light [183, 184]. But by Section 5.3 we know that we can find out the complex coefficients c_j (see (5.13)) of the constituent Laguerre-Gaussian modes using the orthogonality of the same, given that we have estimated the phase of the wave field.

In recent years it has been demonstrated that Laguerre-Gaussian modes can be used as information carriers in free space [91], as they are robust against atmospheric turbulence [8, 92]. As our algorithm retrieves the phase unambiguously even under noisy environments, it can readily be used in such applications. Also, we believe that our algorithm is definitely relevant in situations such as Bose-Einstein condensates [73, 71], x-ray beams [70], atom interferometry [71, 72], and electron beams [68], where phases with dislocations occur naturally.

Finally, the phase retrieval algorithm using perturbed straight line fringes proposed in Chapter 6 can be used in surface metrology [4, 5]. For example, testing as well as polishing of refractive elements to high accuracy can be met easily through the use of interferometers such as Newton and Fizeau interferometers [5]. These interferometers record perturbed straight line fringes, and hence our algorithm can readily be employed. Also, as mentioned in Section 6.6, this algorithm can be employed in the phase-sharing setup (see Figure 6.9) to distill a secret key between two remote observers using atmospheric turbulence as the common source of randomness [168]. Further, our algorithm can find applications in real-time applications which require fast phase estimation, interferometry involving biological samples [185], etc.

7.3 Possible future research works

In this Section we outline some possible future research directions.

1. For the iterative algorithm using three plane intensity measurements to retrieve phases with dislocations (developed in Chapter 5), we used partial Fourier transformation as

it does not conserve the longitudinal OAM. The other FOOS which do not conserve OAM need to be explored.

2. Similarly, with availability of cylindrical lenses, the iterative algorithm could be readily demonstrated in a lab.

3. In Section 6.2, we outlined the algorithm to extract phase from its gradients wherein the discretized phase matrix and discretized phase gradients were related by Hudgin geometry matrix. Instead, one can try other well known geometries such as Fried geometry [48], Southwell geometry [47], and so on, to compute the phase matrix from its gradients, and this needs to be explored.

4. Finally, as observed earlier in Section 6.6, the proposed algorithm to extract phase from its gradients (see Section 6.2) won't work for circular fringes because of the algorithm's inherent dependence on the Hilbert transform. So, a single-shot algorithm to extract phase from such fringes without unwrapping needs to be developed.

Bibliography

[1] P. Rastogi and E. Hack, *Phase Estimation in Optical Interferometry*. CRC Press, 2014.

[2] M. Born and E. Wolf, *Principles of Optics: Electromagnetic Theory of Propagation, Interference and Diffraction of Light*. Cambridge University Archive, 2000.

[3] D. C. Ghiglia and M. D. Pritt, *Two-Dimensional Phase Unwrapping: Theory, Algorithms, and Software*. John Wiley, 1998.

[4] K. Creath, "Phase-measurement interferometry techniques," *Progress In Optics XXVI*, vol. 26, pp. 349–393, 1988.

[5] D. Malacara, *Optical Shop Testing*. John Wiley, 2007.

[6] A. Patil and P. Rastogi, "Moving ahead with phase," *Optics and Lasers in Engineering*, vol. 45, pp. 253–257, 2007.

[7] G. Rajshekhar and P. Rastogi, "Fringe analysis: Premise and perspectives," *Optics and Lasers in Engineering*, vol. 50, pp. iii–x, 2007.

[8] G. Gbur, *Singular optics*. CRC press: Boca Raton, 2017.

[9] A. Lubk, G. Guzzinati, F. Börrnert, and J. Verbeeck, "Transport of intensity phase retrieval of arbitrary wave fields including vortices," *Physical Review Letters*, vol. 111, p. 173902, 2013.

[10] M. R. Teague, "Deterministic phase retrieval: a green's function solution," *Journal of Optical Society of America*, vol. 73, pp. 1434–1441, 1983.

[11] A. V. Martin and L. J. Allen, "Phase imaging from a diffraction pattern in the presence of vortices," *Optics Communications*, vol. 277, pp. 288–294, 2007.

[12] T. E. Gureyev, A. Roberts, and K. A. Nugent, "Phase retrieval with the transport-of-intensity equation: matrix solution with use of zernike polynomials," *Journal of Optical Society of America A*, vol. 12, pp. 1932–1941, 1995.

[13] ——, "Partially coherent fields, the transport-of-intensity equation, and phase uniqueness," *Journal of Optical Society of America A*, vol. 12, pp. 1942–1946, 1995.

[14] L. Allen and M. Oxley, "Phase retrieval from series of images obtained by defocus variation," *Optics Communications*, vol. 199, pp. 65–75, 2001.

[15] M. Takeda, H. Ina, and S. Kobayashi, "Fourier-transform method of fringe-pattern analysis for computer-based topography and interferometry," *Journal of Optical Society of America*, vol. 72, pp. 156–160, 1982.

[16] T. Ikeda, G. Popescu, R. R. Dasari, and M. S. Feld, "Hilbert phase microscopy for investigating fast dynamics in transparent systems," *Optics Letters*, vol. 30, pp. 1165–1167, 2005.

[17] M. A. Schofield and Y. Zhu, "Fast phase unwrapping algorithm for interferometric applications," *Optics Letters*, vol. 28, pp. 1194–1196, 2003.

[18] G. Páez and M. Strojnik, "Fringe analysis and phase reconstruction from modulated intensity patterns," *Optics Letters*, vol. 22, pp. 1669–1671, 1997.

[19] ——, "Phase-shifted interferometry without phase unwrapping: reconstruction of a decentered wave front," *Journal of Optical Society of America A*, vol. 16, pp. 475–480, 1999.

[20] M. P. Kothiyal and C. Delisle, "Polarization component phase shifters in phase shifting interferometry: error analysis," *Optica Acta*, vol. 33, pp. 787–793, 1986.

[21] T. H. Chyba, L. J. Wang, L. Mandel, and R. Simon, "Measurement of the pancharatnam phase for a light beam," *Optics Letters*, vol. 13, pp. 562–564, 1988.

[22] G. Lai and T. Yatagai, "Generalized phase-shifting interferometry," *Journal of Optical Society of America A*, vol. 8, pp. 822–827, 1991.

[23] P. Hariharan and P. E. Ciddor, "An achromatic phase-shifter operating on the geometric phase," *Optics Communications*, vol. 110, pp. 13–17, 1994.

[24] S. S. Helen, M. P. Kothiyal, and R. S. Sirohi, "Achromatic phase shifting by a rotating polarizer," *Optics Communications*, vol. 154, pp. 249–254, 1998.

[25] C. J. Morgan, "Least-squares estimation in phase-measurement interferometry," *Optics Letters*, vol. 7, pp. 368–370, 1982.

[26] J. Schmit and K. Creath, "Extended averaging technique for derivation of error-compensating algorithms in phase-shifting interferometry," *Applied Optics*, vol. 34, pp. 3610–3619, 1995.

[27] J. A. Ferrari and E. M. Frins, "Multiple phase-shifted interferograms obtained from a single interferogram with linear carrier," *Optics Communications*, vol. 271, pp. 59–64, 2007.

[28] J. H. Bruning, D. R. Herriott, J. E. Gallagher, D. P. Rosenfeld, A. D. White, and D. J. Brangaccio, "Digital wavefront measuring interferometer for testing optical surfaces and lenses," *Applied Optics*, vol. 13, pp. 2693–2703, 1974.

[29] P. Gao, B. Yao, J. Han, L. Chen, Y. Wang, and M. Lei, "Phase and amplitude reconstruction from a single carrier-frequency interferogram without phase unwrapping," *Applied Optics*, vol. 47, pp. 2760–2766, 2008.

[30] T. Kreis, "Digital holographic interference-phase measurement using the fourier-transform method," *Journal of Optical Society of America A*, vol. 3, pp. 847–855, 1986.

[31] J. Gass, A. Dakoff, and M. K. Kim, "Phase imaging without 2π ambiguity by multiwavelength digital holography," *Optics Letters*, vol. 28, pp. 1141–1143, 2003.

[32] R. J. Salazar, F. G. Sanchez, and C. R. Sanchez, "Theory and algorithms of an efficient fringe analysis technology for automatic measurement applications," *Applied Optics*, vol. 54, pp. 5364–5374, 2015.

[33] R. J. Salazar, C. R. Sanchez, F. G. Sanchez, A. B. Pinzon, J. G. Garcia, and A. S. Alvarado, "Intensity normalization of additive and multiplicative spatially multiplexed patterns with n encoded phases," *Optics and Lasers in Engineering*, vol. 77, pp. 225–229, 2016.

[34] M. Bahich, M. Afifi, and E. Barj, "Optical phase extraction algorithm based on the continuous wavelet and the hilbert transforms," *Journal of Computing*, vol. 2, pp. 1–5, 2010.

[35] Y. Xu, Y. Wang, W. Jin, C. Lv, and H. Wu, "A new method of phase derivative extracting for off-axis quantitative phase imaging," *Optics Communications*, vol. 305, pp. 13–16, 2013.

[36] J. Min, B. Yao, M. Zhou, R. Guo, M. Lei, Y. Yang, D. Dan, S. Yan, and T. Peng, "Phase retrieval without unwrapping by single-shot dual-wavelength digital holography," *Journal of Optics*, vol. 16, p. 125409, 2014.

[37] W. Niu, L. Zhong, P. Sun, W. Zhang, and X. Lu, "Two-step phase retrieval algorithm based on the quotient of inner products of phase-shifting interferograms," *Journal of Optics*, vol. 17, p. 085703, 2015.

[38] E. C. G. Sudharshan, R. Simon, and N. Mukunda, "Paraxial-wave optics and relativistic front description. i. the scalar theory," *Physical Review A*, vol. 28, pp. 2921–2932, 1983.

[39] A. E. Siegman, *Lasers*. University Science, Mill Valley, CA, 1986.

[40] L. V. V. Arevalo, *"Time-Frequency Analysis Based on Wavelets for Hamiltonian Systems" Ph.D dissertation*. California Institute of Technology, Pasadena, CA, 2002.

[41] R. Carmona, W. L. Hwang, and B. Torrésani, *Practical Time-Frequency Analysis: Gabor and Wavelet Transforms, with an Implementation in S*. Academic Press, 1998.

[42] B. Picinbono, "On instantaneous amplitude and phase of signals," *IEEE Transactions on Signal Processing*, vol. 45, pp. 552–560, 1997.

[43] E. T. Copson, *Asymptotic expansions*. Cambridge University Press, 1965.

[44] I. Iglesias, "Phase estimation from digital holograms without unwrapping," *Optics Express*, vol. 22, pp. 21 340–21 346, 2014.

[45] R. K. Tyson, *Principles of Adaptive Optics*. CRC Press, 2011.

[46] J. M. Geary, *Introduction to wavefront sensors*. SPIE Optical Engineering Press, WA, 1995.

[47] W. H. Southwell, "Wave-front estimation from wave-front slope measurements," *Journal of Optical Society of America*, vol. 70, pp. 998–1006, 1980.

[48] D. L. Fried, "Least-square fitting a wave-front distortion estimate to an array of phase-difference measurements," *Journal of Optical Society of America*, vol. 67, pp. 370–375, 1977.

[49] R. H. Hudgin, "Wave-front reconstruction for compensated imaging," *Journal of Optical Society of America*, vol. 67, pp. 375–378, 1977.

[50] J. Hermann, "Least-squares wave-front errors of minimum norm," *Journal of Optical Society of America*, vol. 70, pp. 28–35, 1980.

[51] F. Roddier and C. Roddier, "Wavefront reconstruction using iterative fourier transforms," *Applied Optics*, vol. 30, pp. 1325–1327, 1991.

[52] B. R. Hunt, "Matrix formulation of the reconstruction of phase values from phase differences," *Journal of Optical Society of America*, vol. 69, pp. 393–399, 1979.

[53] D. C. Ghiglia and L. A. Romero, "Robust two-dimensional weighted and unweighted phase unwrapping that uses fast transforms and iterative methods," *Journal of Optical Society of America A*, vol. 11, pp. 107–117, 1994.

[54] D. Kerr, G. H. Kaufmann, and G. E. Galizzi, "Unwrapping of interferometric phase-fringe maps by the discrete cosine transform," *Applied Optics*, vol. 35, pp. 810–816, 1996.

[55] X. Liu, Y. Gao, and M. Chang, "A partial differential equation algorithm for wavefront reconstruction in lateral shearing interferometry," *Journal of Optics A: Pure and Applied Optics*, vol. 11, p. 045702, 2009.

[56] F. Dai, F. Tang, X. Wang, and O. Sasaki, "Generalized zonal wavefront reconstruction for high spatial resolution in lateral shearing interferometry," *Journal of Optical Society of America A*, vol. 29, pp. 2038–2047, 2012.

[57] F. Dai, F. Tang, X. Wang, O. Sasaki, and P. Feng, "Modal wavefront reconstruction based on zernike polynomials for lateral shearing interferometry: comparisons of existing algorithms," *Applied Optics*, vol. 51, pp. 5028–5037, 2012.

[58] R. W. Gerchberg and W. O. Saxton, "A practical algorithm for the determination of phase from image and diffraction plane pictures," *Optik*, vol. 35, pp. 237–246, 1972.

[59] J. R. Fienup, "Reconstruction of an object from the modulus of its fourier transform," *Optics Letters*, vol. 3, pp. 27–29, 1978.

[60] ——, "Phase retrieval algorithms: a comparison," *Applied Optics*, vol. 21, pp. 2758–2769, 1982.

[61] ——, "Phase-retrieval algorithms for a complicated optical system," *Applied Optics*, vol. 32, pp. 1737–1746, 1993.

[62] G.-Z. Yang, B.-Z. Dong, B.-Y. Gu, J.-Y. Zhuang, and O. K. Ersoy, "Gerchberg-saxton and yang-gu algorithms for phase retrieval in a nonunitary transform system: a comparison," *Applied Optics*, vol. 33, pp. 209–218, 1994.

[63] Y. Zhang, G. Pedrini, W. Osten, and H. J. Tiziani, "Whole optical wave field reconstruction from double or multi in-line holograms by phase retrieval algorithm," *Optics Express*, vol. 11, pp. 3234–3241, 2003.

[64] G. Pedrini, W. Osten, and Y. Zhang, "Wave-front reconstruction from a sequence of interferograms recorded at different planes," *Optics Letters*, vol. 30, pp. 833–835, 2005.

[65] J. F. Nye and M. V. Berry, "Dislocations in wave trains," *Proceedings of the Royal Society A*, vol. 336, pp. 165–190, 1974.

[66] L. Marrucci, C. Manzo, and D. Paparo, "Optical spin-to-orbital angular momentum conversion in inhomogeneous anisotropic media," *Physical Review Letters*, vol. 96, p. 163905, 2006.

[67] A. M. Yao and M. J. Padgett, "Orbital angular momentum: origins, behavior and applications," *Advances in Optics and Photonics*, vol. 3, pp. 161–204, 2011.

[68] J. Verbeeck, H. Tian, and P. Schattschneider, "Production and application of electron vortex beams," *Nature*, vol. 467, pp. 301–304, 2010.

[69] S. M. Lloyd, M. Babiker, G. Thirunavukkarasu, and J. Yuan, "Electron vortices: Beams with orbital angular momentum," *Reviews of Modern Physics*, vol. 89, p. 035004, 2017.

[70] A. G. Peele, P. J. McMahon, D. Paterson, C. Q. Tran, A. P. Mancuso, K. A. Nugent, J. P. Hayes, E. Harvey, B. Lai, and I. McNulty, "Observation of an x-ray vortex," *Optics Letters*, vol. 27, pp. 1752–1754, 2002.

[71] R. G. Scott, T. E. Judd, and T. M. Fromhold, "Exploiting soliton decay and phase fluctuations in atom chip interferometry of bose-einstein condensates," *Physical Review Letters*, vol. 6100, p. 100402, 2008.

[72] K. A. Nugent and D. Paganin, "Matter-wave phase measurement: A noninterferometric approach," *Physical Review A*, vol. 61, p. 063614, 2000.

[73] M. R. Matthews, B. P. Anderson, P. C. Haljan, D. S. Hall, C. E. Wieman, and E. A. Cornell, "Vortices in a bose-einstein condensate," *Physical Review Letters*, vol. 83, pp. 2498–2501, 1999.

[74] Y. Qiao, W. Wang, N. Minematsu, J. Liu, M. Takeda, and X. Tang, "A theory of phase singularities for image representation and its applications to object tracking and image matching," *IEEE Transactions on Signal Processing*, vol. 18, pp. 2153–2166, 2009.

[75] L. J. Allen, H. M. L. Faulkner, K. A. Nugent, M. P. Oxley, and D. Paganin, "Phase retrieval from images in the presence of first-order vortices," *Physical Review E*, vol. 63, p. 037602, 2001.

[76] H. Kogelnik and T. Li, "Laser beams and resonators," *Applied Optics*, vol. 5, pp. 1550–1567, 1966.

[77] M. W. Beijersbergen, R. P. C. Coerwinkel, M. Kristensen, and J. P. Woerdman, "Astigmatic laser mode converters and transfer of orbital angular momentum," *Optics Communications*, vol. 96, pp. 123–132, 1993.

[78] T. W. Clark, R. F. Offer, S. F. Arnold, A. S. Arnold, and N. Radwell, "Comparison of beam generation techniques using a phase only spatial light modulator," *Optics Express*, vol. 24, pp. 6249–6264, 2016.

[79] J. Courtial, "Self-imaging beams and the guoy effect," *Optics Communications*, vol. 151, pp. 1–4, 1998.

[80] L. Allen, M. W. Beijersbergen, R. J. C. Spreeuw, and J. P. Woerdman, "Orbital angular momentum of light and the transformation of laguerre-gaussian laser modes," *Physical Review A*, vol. 45, pp. 8185–8189, 1992.

[81] C.-S. Guo, S.-J. Yue, and G.-X. Wei, "Measuring the orbital angular momentum of optical vortices using a multipinhole plate," *Applied Physics Letters*, vol. 94, p. 231104, 2009.

[82] C. Schulze, A. Dudley, D. Flamm, M. Duparré, and A. Forbes, "Measurement of the orbital angular momentum density of light by modal decomposition," *New Journal of Physics*, vol. 15, p. 073025, 2013.

[83] J. Chen, X. Liu, J. Yu, and Y. Cai, "Simultaneous determination of the sign and the magnitude of the topological charge of a partially coherent vortex beam," *Applied Physics B: Lasers and Optics*, vol. 122, p. 201, 2016.

[84] V. V. Kotlyar, A. A. Kovalev, and A. P. Porfirev, "Astigmatic transforms of an optical vortex for measurement of its topological charge," *Applied Optics*, vol. 56, pp. 4095–4104, 2017.

[85] K. Murphy, D. Burke, N. Devaney, and C. Dainty, "Experimental detection of optical vortices with a shack-hartmann wavefront sensor," *Optics Express*, vol. 18, pp. 15 448–15 460, 2010.

[86] R. Yazdani and H. Fallah, "Wavefront sensing for a shack-hartmann sensor using phase retrieval based on a sequence of intensity patterns," *Applied Optics*, vol. 56, pp. 1358–1364, 2017.

[87] C. Stahl and G. Gbur, "Analytic calculation of vortex diffraction by a triangular aperture," *Journal of Optical Society of America A*, vol. 33, pp. 1175–1180, 2016.

[88] J. Zhou, W. Zhang, and L. Chen, "Experimental detection of high-order or fractional orbital angular momentum of light based on a robust mode converter," *Applied Physics Letters*, vol. 108, p. 111108, 2016.

[89] A. A. Kovalev, V. V. Kotlyar, and A. P. Porfirev, "Asymmetric laguerre-gaussian beams," *Physical Review A*, vol. 93, p. 063858, 2016.

[90] V. V. Kotlyar and A. A. Kovalev, "Hermite–gaussian modal laser beams with orbital angular momentum," *Journal of Optical Society of America A*, vol. 31, pp. 274–282, 2014.

[91] G. Gibson, J. Courtial, M. J. Padgett, M. Vasnetsov, V. Pas'ko, S. M. Barnett, and S. F.-Arnold, "Free-space information transfer using light beams carrying orbital angular momentum," *Optics Express*, vol. 12, pp. 5448–5456, 2004.

[92] G. Gbur and R. K. Tyson, "Vortex beam propagation through atmospheric turbulence and topological charge conservation," *Journal of Optical Society of America A*, vol. 25, pp. 225–230, 2008.

[93] A. Vaziri, G. Weihs, and A. Zeilinger, "Experimental two-photon, three-dimensional entanglement for quantum communication," *Physical Review Letters*, vol. 89, p. 240401, 2002.

[94] E. C. G. Sudarshan, N. Mukunda, and R. Simon, "Realization of first order optical systems using thin lenses," *Optica Acta*, vol. 32, pp. 855–872, 1985.

[95] P. A. A. Yasir and J. S. Ivan, "Realization of first-order optical systems using thin convex lenses of fixed focal length," *Journal of Optical Society of America A*, vol. 31, pp. 2011–2020, 2014.

[96] R. Simon and K. B. Wolf, "Structure of the set of paraxial optical systems," *Journal of Optical Society of America A*, vol. 17, pp. 342–355, 2000.

[97] A. Ishimaru, *Wave Propagation and Scattering in Random Media, Vol. 2*. Academic Press, New York, 1978.

[98] J. W. Strohbehn, *Laser Beam Propagation in the atmosphere*. Springer-Verlag, New York, 1978.

[99] L. C. Andrews and R. L. Phillips, *Laser Beam Propagation through Random Media*. SPIE Press, WA, 2005.

[100] W. A. Coles, J. P. Filice, R. G. Frehlich, and M. Yadlowsky, "Simulation of wave propagation in three-dimensional random media," *Applied Optics*, vol. 34, pp. 2089–2101, 1995.

[101] R. G. Lane, A. Glindemann, and J. C. Dainty, "Simulation of a kolmogorov phase screen," *Waves in Random Media*, vol. 2, pp. 209–224, 1992.

[102] V. I. Tatarski, *The Effects of the Turbulent Atmosphere on Wave Propagation*. Israel Program for Scientific Translations, Jerusalem, 1971.

[103] J. M. Martin and S. M. Flatté, "Intensity images and statistics from numerical simulation of wave propagation in 3-d random media," *Applied Optics*, vol. 27, pp. 2111–2126, 1988.

[104] ——, "Simulation of point-source scintillation through three-dimensional random media," *Journal of Optical Society of America A*, vol. 7, pp. 838–847, 1990.

[105] J. M. Geary, *Introduction to lens design: with practical ZEMAX examples*. Richmond: Willmann-Bell, 2002.

[106] D. J. Griffiths, *Introduction to electrodynamics*. Prentice Hall, 1999.

[107] G. B. Arfken and H. J. Weber, *Mathematical methods for physicists*. Elsevier, 2005.

[108] J. W. Goodman, *Introduction to Fourier Optics*. Roberts and Company Publishers, Englewood, CO, 2005.

[109] B. E. A. Saleh and M. C. Teich, *Fundamentals of photonics*. Wiley-Interscience, 2007.

[110] D. Stoler, "Operator methods in physical optics," *Journal of Optical Society of America*, vol. 71, pp. 334–341, 1981.

[111] H. Bacry and M. Cadilhac, "Metaplectic group and fourier optics," *Physical Review A*, vol. 23, pp. 2533–2536, 1981.

[112] R. Simon, E. C. G. Sudarshan, and N. Mukunda, "Gaussian pure states in quantum mechanics and the symplectic group," *Physical Review A*, vol. 37, pp. 3028–3038, 1988.

[113] M. Moshinsky and C. Quesne, "Linear canonical transformations and their unitary representations," *Journal of Mathematical Physics*, vol. 12, pp. 1772–1780, 1971.

[114] Arvind, B. Dutta, N. Mukunda, and R. Simon, "The real symplectic groups in quantum mechanics and optics," *Pramana*, vol. 45, pp. 471–497, 1995.

[115] J. J. Sakurai, *Modern quantum mechanics*. Reading, MA: Addison-Wesley, 1994.

[116] J. J. Healy, M. A. Kutay, H. M. Ozaktas, and e. J. T. Sheridan, *Linear canonical transforms: Theory and applications*. Springer (Vol. 198), 2015.

[117] R. Simon, E. C. G. Sudarshan, and N. Mukunda, "Generalized rays in first-order optics: transformation properties of gaussian schell-model fields," *Physical Review A*, vol. 29, pp. 3273–3279, 1984.

[118] R. Simon, N. Mukunda, and E. C. G. Sudarshan, "Partially coherent beams and generalized abcd law," *Optics Communications*, vol. 65, pp. 322–328, 1988.

[119] R. Simon, E. C. G. Sudarshan, and N. Mukunda, "Gaussian–maxwell beams," *Journal of Optical Society of America A*, vol. 3, pp. 536–540, 1986.

[120] ——, "Cross polarization in laser beams," *Applied Optics*, vol. 26, pp. 1589–1593, 1987.

[121] N. Mukunda, R. Simon, and E. C. G. Sudarshan, "Fourier optics for the maxwell field: formalism and applications," *Journal of Optical Society of America A*, vol. 2, pp. 416–426, 1985.

[122] D. Wei and Y.-M. Li, "Generalized sampling expansions with multiple sampling rates for lowpass and bandpass signals in the fractional fourier transform domain," *IEEE Transactions on Signal Processing*, vol. 64, pp. 4861–4874, 2016.

[123] D. Wei, R. Wang, and Y.-M. Li, "Random discrete linear canonical transform," *Journal of Optical Society of America A*, vol. 33, pp. 2470–2476, 2016.

[124] J. Shamir and N. Cohen, "Root and power transformations in optics," *Journal of Optical Society of America A*, vol. 12, pp. 2415–2423, 1995.

[125] L. Allen and M. Padgett, "The orbital angular momentum of light: An introduction," *Twisted Photons: Applications of Light with Orbital Angular Momentum*, pp. 1–12, 2011.

[126] K. Y. Bliokh and F. Nori, "Transverse and longitudinal angular momenta of light," *Physics Reports*, vol. 592, pp. 1–38, 2015.

[127] V. Madhu and J. S. Ivan, "Robustness of the twist parameter of laguerre-gaussian mode superpositions against atmospheric turbulence," *Physical Review A*, vol. 95, p. 043836, 2017.

[128] R. Simon, K. Sundar, and N. Mukunda, "Twisted gaussian schell-model beams. i. symmetry structure and normal-mode spectrum," *Journal of Optical Society of America A*, vol. 10, pp. 2008–2016, 1993.

[129] G. Nienhuis and L. Allen, "Paraxial wave optics and harmonic oscillators," *Physical Review A*, vol. 48, pp. 656–665, 1993.

[130] L. Mandel and E. Wolf, *Optical coherence and quantum optics*. Cambridge University Press, 1995.

[131] B. Schäfer and K. Mann, "Determination of beam parameters and coherence properties of laser radiation by use of an extended hartmannâĂŞshack wave-front sensor," *Applied Optics*, vol. 41, pp. 2809–2817, 2002.

[132] M. Nazarathy and J. Shamir, "First-order optics–a canonical operator representation: lossless systems," *Journal of Optical Society of America*, vol. 72, pp. 356–364, 1982.

[133] J. R. Fienup and C. C. Wackerman, "Phase-retrieval stagnation problems and solutions," *Journal of Optical Society of America A*, vol. 3, pp. 1897–1907, 1986.

[134] J. T. Foley and R. R. Butts, "Uniqueness of phase retrieval from intensity measurements," *Journal of Optical Society of America*, vol. 71, pp. 1008–1014, 1981.

[135] L. Wang, B. Dong, and G. Yang, "Phase retrieval from two intensity measurements in an optical system involving nonunitary transformation," *Applied Optics*, vol. 29, pp. 3422–3427, 1990.

[136] J. D. Jackson, *Classical electrodynamics*. Wiley, 1999.

[137] G. Rieke, *Detection of light : From the ultraviolet to the submillimeter*. Cambridge University Press, 2003.

[138] L. W. Casperson, "Synthesis of gaussian beam optical systems," *Applied Optics*, vol. 20, pp. 2243–2249, 1981.

[139] H. H. Arsenault and B. Macukow, "Factorization of the transfer matrix for symmetrical optical systems," *Journal of Optical Society of America*, vol. 73, pp. 1350–1359, 1983.

[140] S. Cornbleet, "Geometrical optics reviewed: A new light on an old subject," *Proceedings of the IEEE*, vol. 71, pp. 471–502, 1983.

[141] O. N. Stavroudis, *The optics of rays, wavefronts, and caustics*. Academic Press, 1972.

[142] M. J. Bastiaans and T. Alieva, "Synthesis of an arbitrary abcd system with fixed lens positions," *Optics Letters*, vol. 31, pp. 2414–2416, 2006.

[143] X. Liu and K. H. Brenner, "Minimal optical decomposition of ray transfer matrices," *Applied Optics*, vol. 47, pp. E88–E98, 2008.

[144] N. Mukunda, "Role of symmetry and group structure in optics," *Current Science*, vol. 59, pp. 1135–1151, 1990.

[145] M. J. Bastiaans and T. Alieva, "Classification of lossless first-order optical systems and the linear canonical transformation," *Journal of Optical Society of America A*, vol. 24, pp. 1053–1062, 2007.

[146] ——, "Properties of the linear canonical integral transformation," *Journal of Optical Society of America A*, vol. 24, pp. 3658–3665, 2007.

[147] D. J. Ming and F. H. Yi, "New decomposition of the fresnel operator corresponding to the optical transformation in abcd-systems," *Chinese Physics B*, vol. 22, p. 060302, 2013.

[148] R. A. Horn and C. R. Johnson, *Matrix analysis*. Cambridge University Press, 2013.

[149] H. H. Arsenault, "Generalization of the principal plane concept in matrix optics," *Americal Journal of Physics*, vol. 48, pp. 397–399, 1980.

[150] M. Nazarathy and J. Shamir, "Fourier optics described by operator algebra," *Journal of Optical Society of America*, vol. 70, pp. 150–159, 1980.

[151] S. Baskal and Y. S. Kim, "Shear representations of beam transfer matrices," *Physical Review E*, vol. 63, p. 056606, 2001.

[152] R. Simon, N. Mukunda, and B. Dutta, "Quantum-noise matrix for multimode systems: U(n) invariance, squeezing, and normal forms," *Physical Review A*, vol. 49, pp. 1567–1583, 1994.

[153] H. Xu, "An svd-like matrix decomposition and its applications," *Linear Algebra and its Applications*, vol. 368, pp. 1–24, 2003.

[154] H. Goldstein, *Classical mechanics*. Reading, MA: Addison-Wesley, 1980.

[155] L. C. Biedenharn and J. D. Louck, *Angular Momentum in Quantum Physics: Theory and Application*. Reading, MA: Addison-Wesley, 1981.

[156] B. N. Simon, S. Simon, F. Gori, M. Santarsiero, R. Borghi, N. Mukunda, and R. Simon, "Nonquantum entanglement resolves a basic issue in polarization optics," *Physical Review Letters*, vol. 104, p. 023901, 2010.

[157] M. McLaren, T. Konrad, and A. Forbes, "Measuring the nonseparability of vector vortex beams," *Physical Review A*, vol. 92, p. 023833, 2015.

[158] X.-F. Qian and J. H. Eberly, "Entanglement and classical polarization states," *Optics Letters*, vol. 36, pp. 4110–4112, 2011.

[159] A. Forbes, *Laser beam propagation*. CRC press: Boca Raton, 2014.

[160] S. Prabhakar, S. G. Reddy, A. Aadhi, C. Perumangatt, G. K. Samanta, and R. P. Singh, "Violation of bell's inequality for phase-singular beams," *Physical Review A*, vol. 92, p. 023822, 2015.

[161] F. G. Mitri, "Quasi-gaussian electromagnetic beams," *Physical Review A*, vol. 87, p. 035804, 2013.

[162] F. Töppel, A. Aiello, C. Marquardt, E. Giacobino, and G. Leuchs, "Classical entanglement in polarization metrology," *New Journal of Physics*, vol. 16, p. 073019, 2014.

[163] A. Aiello, F. Töppel, C. Marquardt, E. Giacobino, and G. Leuchs, "Quantum–like nonseparable structures in optical beams," *New Journal of Physics*, vol. 17, p. 043024, 2015.

[164] V. Namias, "The fractional order fourier transform and its application to quantum mechanics," *IMA Journal of Applied Mathematics*, vol. 25, pp. 241–265, 1980.

[165] V. Britanak, P. C. Yip, and K. R. Rao, *Discrete Cosine and Sine Transforms*. Elseiver London, 2007.

[166] B. Bhaduri and G. Popescu, "Derivative method for phase retrieval in off-axis quantitative phase imaging," *Optics Letters*, vol. 37, pp. 1868–1870, 2012.

[167] G. Popescu, T. Ikeda, R. R. Dasari, and M. S. Feld, "Diffraction phase microscopy for quantifying cell structure and dynamics," *Optics Letters*, vol. 31, pp. 775–777, 2006.

[168] L. Thomas, J. S. Ivan, P. A. A. Yasir, R. Sharma, R. K. Singh, C. S. Narayanamurthy, and K. S. Dasgupta, "Phase-sharing using a machâĂŞzehnder interferometer," *Applied Optics*, vol. 54, pp. 699–706, 2015.

[169] S. V. Mantravadi, T. A. Rhoadarmer, and R. S. Glas, "Simple laboratory system for generating well-controlled atmospheric-like turbulence," *Advanced Wavefront Control: Methods, Devices, and Applications II*, vol. 5553, pp. 290–300, 2004.

[170] R. Barakat, "Analytic proofs of the arago-fresnel laws for the interference of polarized light," *Journal of Optical Society of America A*, vol. 10, pp. 180–185, 1993.

[171] M. Brown and D. J. Lowe, "Automatic panoramic image stitching using invariant features," *International Journal of Computer Vision*, vol. 74, pp. 59–73, 2007.

[172] T. Yatagai, S. Nakadate, M. Idesawa, and H. Saito, "Automatic fringe analysis using digital image processing techniques," *Optical Engineering*, vol. 21, pp. 432–435, 1982.

[173] D. Zhang, M. Ma, and D. D. Arola, "Fringe skeletonizing using an improved derivative sign binary method," *Optics and Lasers in Engineering*, vol. 37, pp. 51–62, 2002.

[174] C. J. Tay, C. Quan, F. J. Yang, and X. Y. He, "A new method for phase extraction from a single fringe pattern," *Optics Communications*, vol. 239, pp. 251–258, 2004.

[175] X. Yang, Q. Yu, and S. Fu, "Determination of skeleton and sign map for phase obtaining from a single espi image," *Optics Communications*, vol. 282, pp. 2301–2306, 2009.

[176] M. Bahich, M. Afifi, and E. Barj, "A numerical spatial carrier for single fringe pattern analysis algorithm," *Optik*, vol. 122, pp. 1821–1824, 2011.

[177] N. R. Heckenberg, R. McDuff, C. P. Smith, and A. G. White, "Generation of optical phase singularities by computer-generated holograms," *Optics Letters*, vol. 17, pp. 221–223, 1992.

[178] M. Chen, F. S. Roux, and J. C. Olivier, "Detection of phase singularities with a shack–hartmann wavefront sensor," *Journal of Optical Society of America A*, vol. 24, pp. 1994–2002, 2007.

[179] Y. Ichioka, T. Iwaki, and K. Matsuoka, "Optical information processing and beyond," *Proceedings of the IEEE*, vol. 84, pp. 694–719, 1996.

[180] G. C. G. Berkhout, M. P. J. Lavery, J. Courtial, M. W. Beijersbergen, and M. J. Padgett, "Efficient sorting of orbital angular momentum states of light," *Physical Review Letters*, vol. 105, p. 153601, 2010.

[181] M. Mirhosseini, M. Malik, Z. Shi, and R. W. Boyd, "Efficient separation of the orbital angular momentum eigenstates of light," *Nature communications*, vol. 4, p. 2781, 2013.

[182] B. Sephton, A. Dudley, G. Ruffato, F. Romanato, L. Marrucci, M. Padgett, S. Goyal, F. Roux, T. Konrad, and A. Forbes, "A versatile quantum walk resonator with bright classical light," *Plos One*, vol. 14, p. e0214891, 2019.

[183] B. P.-Garcia, R. I. H.-Aranda, A. Forbes, and T. Konrad, "The first iteration of grover's algorithm using classical light with orbital angular momentum," *Journal of Modern Optics*, vol. 65, pp. 1942–1948, 2018.

[184] S. Zhang, P. Li, B. Wang, Q. Zeng, and X. Zhang, "Implementation of quantum permutation algorithm with classical light," *Journal of Physics Communications*, vol. 3, p. 015008, 2019.

[185] D. D. Nolte, *Optical Interferometry for Biology and Medicine*. Springer, 2012.

List of Publications

Refereed Journals

1. **P. A. Ameen Yasir** and J. Solomon Ivan, "Phase estimation using phase gradients obtained through Hilbert transform," *Journal of Optical Society of America A*, vol. 33, pp. 2010–2019, 2016.

2. **P. A. Ameen Yasir** and J. Solomon Ivan, "Realization of first-order optical systems using thin lenses of positive focal length," *Journal of Optical Society of America A*, vol. 34, pp. 2007–2012, 2017.

3. **P. A. Ameen Yasir** and J. Solomon Ivan, "Estimation of phases with dislocations in paraxial wave fields from intensity measurements," *Physical Review A*, vol. 97, pp. 023817, 2018.